Ab initio study of the supercritical state of iron

Zhi Li

Numéro National de Thèse : 2021LYSEN003

THÈSE de DOCTORAT DE L'UNIVERSITÉ DE LYON

opérée par

l'École Normale Supérieure de Lyon

École Doctorale N°52
Physique et Astrophysique de Lyon (PHAST)

Spécialité de doctorat : Physique des Minéraux
Discipline : Sciences de la Terre

Soutenue publiquement le 28/01/2021 par :
Zhi LI

Ab initio study of the supercritical state of iron

Etude *ab initio* de l'état supercritique du fer

Devant le jury composé de :

Alfè, Dario	Professeur	University College London	Rapporteur
Moynier, Frédéric	Professeur	Institut de Physique du Globe de Paris	Rapporteur
McCammon, Catherine	Chargée de recherche	Bayerisches Geoinstitut	Examinatrice
Labrosse, Stéphane	Professeur	ENS de Lyon	Examinateur
Caracas, Razvan	Directeur de recherche	ENS de Lyon	Directeur de thèse

Abstract

Iron as a building block material of the Earth naturally received significant attention. Considerable efforts have been made to determine its thermodynamic and thermophysical properties up to the Earth's inner core's conditions. However, its physical properties in the low-density regime are less explored, and notably the position of the liquid-vapor equilibrium line and of the critical point are lacking. The missing information inhibits developing a complete equation of state that covers the released state after shock waves, and thus hinders the characterization of large planetary impacts.

The present study aims at closing the knowledge gap on the liquid-vapor equilibrium dome of iron. For this we exploit molecular dynamics and Monte Carlo methods where the energy and the forces are estimated by the density functional theory. We then employ statistical and thermodynamics methods to construct the position of the critical point, build the liquid-vapor dome, and characterize the physical properties of the fluid iron.

First we determine the position of the critical point from *ab initio* molecular dynamics simulations along several isotherms. The simulation results provide the position of the liquid spinodal above 3000 K, and the gas spinodal close to the critical point. We bracket the position of the critical point in the 9000-9350 K temperature range, and 1.85-2.40 g/cm^3 density range, corresponding to 4-7 kbars pressure range. Additionally, we characterize the structure and the transport properties of the fluid iron over a wide density and temperature range, with a particular focus on the supercritical state.

Then we compute two Hugoniot lines starting with two realistic initial conditions. By comparing the entropy values calculated along these Hugoniot lines to that at the boiling point, we find that the pressure required to reach the onset vaporization is significantly lower than previous estimates. It suggests that previous hydrodynamic simulations underestimate the iron vapor production, and that the core of Theia underwent partial vaporization during the giant impact. Similarly, we find that a large fraction of the planetesimals falling on Earth during the late veneer must have had their cores undergoing partial vaporization. The readily achieved partial core vaporization would enhance the iron-silicates equilibration, which helps explain geochemical observations.

At last, we determine the liquid-vapor equilibrium line of iron. For this, we have extended and implemented the Gibbs ensemble Monte Carlo method coupled with the finite-temperature density functional theory. The first benchmark test to sodium shows a good agreement with available experimental results. We then apply this technique to iron and calculate its liquid density in equilibrium with the vapor phase. We also show the importance of magnetism diminishes as approaching the critical point.

Résumé

Le fer, en tant que brique élémentaire de la Terre, a reçu beaucoup d'attentions. Des efforts considérables ont été mis en œuvre pour déterminer ses propriétés thermodynamiques et thermophysiques à des conditions atteignant celles du noyau terrestre. Cependant, ses propriétés physiques dans le domaine des faibles densités sont moins explorées, et il manque en particulier la position de la courbe d'équilibre liquide-gaz et du point critique. Les informations manquantes entravent le développement d'une équation d'états complète qui couvrirait l'état de détente post onde de choc, et donc empêchent la caractérisation des grands impacts planétaires.

Cette étude vise à réduire le fossé de connaissances sur l'équilibre liquide-gaz du fer. Pour cela nous utilisons la Dynamique Moléculaire et la méthode Monte Carlo dans lesquelles les énergies et les forces sont estimées à partir de la théorie de la fonctionnelle densité. Nous utilisons ensuite des méthodes statistiques et thermodynamiques pour construire la position du point critique, le dôme liquide-gaz, et caractériser les propriétés physiques du fer à l'état de fluide.

Tout d'abord nous avons déterminé la position du point critique à partir de simulations de dynamique moléculaire ab initio selon plusieurs isothermes. Les résultats des simulations nous ont donné la position du spinodal liquide au-dessus de 3000 K, et du spinodal gazeux à proximité du point critique. La position du point critique est estimée entre 9000-9350 K et 1.85-2.4 g/cm^3, ce qui correspond à 4-7 kbars. Nous avons également caractérisé la structure et les propriétés de transport du fer fluide pour une large gamme de densités et températures, avec une attention particulière sur l'état supercritique.

Ensuite nous avons calculé deux courbes Hugoniot à partir de deux conditions initiales réalistes. En comparant les valeurs d'entropie calculées le long de ces courbes à celle du point d'ébullition, nous avons trouvé que la pression requise pour atteindre le seuil de vaporisation est significativement plus basse que précédemment estimée. Cela suggère que les simulations hydrodynamiques précédentes sous-estiment la production de vapeur de fer, et que le noyau de Théïa aurait subi une vaporisation partielle lors de l'impact géant. De même nous avons trouvé qu'une grande fraction des planétésimaux ayant frappé la Terre lors du vernis tardif ont dû voir leur noyau vaporisé partiellement. La facilité avec laquelle les noyaux se vaporisent devrait améliorer l'équilibration fer-silicate, ce qui permettrait d'expliquer les observations géochimiques.

Enfin, nous avons déterminé l'équilibre liquide-gaz du fer. Pour cela nous avons amélioré et implémenté la méthode Monte Carlo dans l'ensemble de Gibbs couplée avec la théorie de la fonctionnelle densité en températures finies. Le premier test de référence avec le sodium nous as donné un bon accord avec les résultats expérimentaux. Nous avons donc appliqué cette technique au fer et calculé sa densité liquide à l'équilibre avec la phase vapeur. Nous avons également montré que l'importance du magnétisme diminue à l'approche du point critique.

Contents

Chapter 1

The formation of the Moon

Contents

1.1 Introduction

The Moon is the most well-studied satellite in our solar system, whose investigation can be dated back to the epoch of Hipparchus and Ptolemy. In the ancient time, the primary attempt was to observe the lunar orbital motion, document its moving path and estimate its speed relative to a fixed star. These tedious and time-consuming astrophysical observations leads to the discovery of several exciting phenomena like the lunar precession. After Isaac Newton formulated the laws of motion, which laid the foundation of celestial mechanics, the focus has been shifted to explain the observed lunar motion from the perspective of mutual gravitational attractions among the Earth-Moon-Sun system. The modern research into the Moon was mostly motivated by the Apollo missions. These missions returned tons of the lunar rocks. From measurements of their chemical composition, our understanding of the lunar

interior structure has deepened considerably. These new findings, in return, stimulate scientists from different disciplines to research into the possible origin of the Moon.

This chapter will focus on the giant impact theory, which is considered as the most plausible mechanism to explain the Moon's formation. We will first review the major geochemical observations that the giant impact theory must reconcile. We then point out the total angular momentum at the time of the giant impact is still under debate. Possible values are anywhere between once and twice the present value of the Earth-Moon system. Based on this, we can divide the giant impact theory into two categories: the canonical impact model and the high-angular momentum impact model. Next, we give a brief synopsis of the geochemical consequence for these two models. With these background information in mind, we narrow down to the topic of iron, which is the main component of planets' core, and explore its behavior during giant impacts. By examining the phase diagram of iron, we identify a knowledge gap on the thermodynamic properties of iron in the low-density region, which would inhibit developing an accurate equation of state. As an essential ingredient in the giant impact modeling, the equation of state affects the amount of vapor produced as well as the energy distribution across the Earth during the impact. This chapter will end up with research problems on which the present study will focus.

1.2 The possible origin scenarios for the Moon

Many theories have been devised to explain the Moon's origin, including the fission theory, the co-formation theory, the capture theory, and the giant impact hypothesis. In the fission theory, the proto-Earth rotates so rapidly that it becomes dynamically unstable. A lunar-sized mass from the Earth's mantle is separated and injected into the Earth's orbit to be the satellite. Therefore, it is expected that the Moon has a similar isotopic composition and is depleted in iron relative to the Earth. In the co-formation theory, the Moon forms at the same time as its parent Earth. Under such an explanation, in the early solar system, gravity would pull materials together to form the Moon simultaneously as gravity bonds particles together to form the Earth. Such a moon would be expected to have a very similar isotope composition to the Earth. In the capture theory, a rocky body formed elsewhere in the solar system and was later captured by the Earth's gravitational field. Since the body captured has a wide range of possibilities in its isotope composition and iron content, various chemical consequences are possible.

However, each theory stated above fails to explain one of the major characteristics of the Earth-Moon system (see Stevenson, 1987, for a review). The fission theory needs three times more angular momentum than the present Earth-Moon system. But there is no mechanism available to supply such large angular momentum during the planetary accumulation process. The co-formation theory is also challenging due to the difficulties in explaining the lunar iron depletion relative to the Earth (see

Section 1.3). It is more reasonable to expect a very similar iron content if both bodies form together. In the capture theory, the likelihood of capturing a lunar-sized body to the present lunar orbit is nearly zero.

Influenced by Safronov's work on the planet formation through collisions between planetary embryos, both Hartmann and Davis (1975) and Cameron and Ward (1976) proposed the giant impact hypothesis as a plausible explanation for the formation of the Moon. In this model, appropriate impact conditions satisfying the Earth-Moon system's angular momentum constraints would generate a proto-lunar disk with most of the materials originating from the silicate mantle of the impactor or of the proto-Earth, then a Moon is accreted from such a disk. Therefore, the hypothesis can easily explain the lunar iron depletion relative to the Earth. In addition, the giant impact would happen naturally since the collision between planets is thought to be common in the late accretion stage. These characters have rendered the giant impact hypothesis the leading theory to explain the Moon's origin.

1.3 The geochemical constraints

Measuring the lunar rocks' chemical composition returned by Apollo missions and their comparisons to the Earth provide important constraints on which the giant impact hypothesis must reconcile. Both the Moon and the Earth have a very similar interior structure, with an iron core in the center and a silicate mantle lying above. But the average density is different with 3.34 g/cm^3 for the Moon compared to 5.51 g/cm^3 for the Earth, indicating a relative lunar iron depletion. There are two potential iron reservoirs in the Moon: the silicate mantle/crust and the metallic core. Although it is debated on the exact size of the Moon's core, it is generally accepted that its size is at most 400 km in radius (see Canup, 2004b, for a review). The combination of seismic analysis and geological modeling sets an upper bound of the total amount of iron, which is around 8-10 wt% in the Moon compared with 30 wt% in the Earth.

Despite the significant difference in the total amount of iron, a remarkable similarity in the oxygen isotope composition between the Moon and the Earth's silicate mantle was revealed by measuring the oxygen isotope composition of the lunar rock samples. Initially, it was considered that the oxygen isotopes were homogeneous in the solar system, which can explain the observed similarity in the oxygen isotope between the Earth and Moon. However, Franchi et al. (1999) found an offset in fractionation line between the Earth and Mars, indicating oxygen isotopes were distributed heterogeneously in the early solar system. Subsequent N-body simulations also suggest the possibility of a similar oxygen isotope composition between the impactor and the proto-Earth is very low (Pahlevan and Stevenson, 2007). As the oxygen isotope remains unchanged during subsequent geological processes after the Moon's formation, the isotopic indistinguishability provides a strong argument that the Moon's origin is closely linked with the Earth's mantle, and thus provide

a strong constraint on developing the giant impact theory.

The Earth and the Moon also show indifference in titanium isotope composition (^{50}Ti/^{47}Ti) (Zhang et al., 2012). Since titanium was distributed heterogeneously in the solar system, the impactor should differ its titanium isotope composition to the proto-Earth. Then we would expect the Moon to develop an offset in ^{50}Ti/^{47}Ti compared to the Earth, but they do not. The titanium-isotope homogeneity in the Earth-Moon system further confirms that the Moon is accreted from the proto-lunar disk, where most materials are from the Earth's mantle.

Two studies have recently measured the tungsten isotopic composition and found the Moon has a slightly higher ^{182}W/^{184}W ratio than the Earth (Kruijer et al., 2015; Touboul et al., 2015). Since the tungsten isotopes vary throughout the solar system, it is reasonable to expect that the giant impact event would have involved two objects with different isotopic compositions of tungsten. In order to explain the slight difference in ^{182}W/^{184}W, both studies suggest that the Earth and Moon had the same tungsten isotopic composition after the giant impact, and the difference in the ^{182}W/^{184}W ratio between the Earth and Moon is due to the addition of the late veneer, which is thought to have a chondritic composition. The model proposed also requires siderophile elements stripping from the mantle by metal from the impactor's core. Otherwise, the tungsten data would be too abundant due to the addition of the late veneer, which would not be self-consistent with the highly siderophile element concentration in the terrestrial mantle.

Several volatile elements like K and Zn are found to differ their isotopic composition in the Moon and Earth. Wang and Jacobsen (2016) found the lunar rocks are slightly enriched in the heavy isotope of K compared to the Earth. They suggest it may result from the incomplete condensation from a bulk silicate Earth vapor. During the condensation, the lighter isotope would prefer to stay in the vapor phase, causing the enrichment of heaver isotope in the solid or liquid phases. Wang and Jacobsen (2016) also indicate the potassium isotope result is inconsistent with the canonical impact model but supports the high-angular momentum giant impact model for the origin of the Moon. However, as discussed by Canup et al. (2015), the preferential accretion of volatile-rich melt in the inner disk to the Earth, rather than to the Moon, could also contribute to the volatile elements depletion and their isotope fractionation in the Moon. Therefore, the enrichment of the heavy K isotope in the Moon may only support the presence of a proto-lunar disk from which the Moon is accreted, but cannot be used to distinguish different impact models. Paniello et al. (2012) found lunar rocks are enriched in the heavy isotope of Zn and have a lower Zn concentration than the Earth. Since the equilibrium condensation would not produce such a large degree of fractionation, they suggest these variations are due to the lunar magma ocean's large-scale evaporation, which not only decreases the concentration of the volatile elements but also causes the fractionation.

In summary, the Moon is strongly depleted in iron but has a similar refractory element isotope composition to the Earth. Besides, the Moon is enriched in the

heavier isotope of the volatile elements, which is caused by the evaporation process after the Moon's formation and/or the equilibrium condensation accompanying the Moon's formation.

1.4 The dynamical constraint from the lunar orbital evolution

To find a set of impact parameters that can produce a massive and iron-depleted proto-lunar disk, we also need the dynamic constraint of the total angular momentum, which includes the rotational angular momentum of the Earth and the Moon, and the orbital angular momentum of the lunar motion. We know that the Moon is almost in a circular cycle revolving around the Earth with an eccentricity of 0.0549 and a slight inclination of 5.14° to the ecliptic plane (Fig. 1.1). From these real measurements, we can calculate the current total angular momentum of the Earth-Moon system. However, this value may not be the total angular momentum at the time when the Moon formed. Therefore, we need to find a way to recover its evolving history and obtain the total angular momentum at the time when it completed the accretion and detached from the proto-lunar disk. This is not an easy task since the Moon is continuously affected by the tidal interaction exerted by the Earth and Sun to recess its orbit.

1.4.1 The lunar orbital evolution

We can partially solve this problem by celestial mechanics and an essential contribution has been made by Touma and Wisdom (1994) and Touma and Wisdom (1998). As these calculations are extremely complex due to the employment of generalized coordinates like action-angle variables, only a general frame is outlined. Starting with the derivation of an analytic Hamiltonian for the Earth-Moon-Sun system, Touma and Wisdom (1994) made several assumptions like the lunar orbit is a circle to reduce the problem into a manageable size. Together with averaging over the short orbital time scale, the remaining degrees of freedom in the Hamiltonian is the obliquity of the Earth to the ecliptic plane, the mutual inclination of the lunar orbit to the Earth's equator, the inclination of lunar orbit to the ecliptic plane, and the precession rate of the lunar orbit. These variables are constantly changing due to the Earth's oblateness and tidal interactions. Although the physical origin of the tidal torque can easily be understood as the presence of a phase lag due to the mismatch between the orbital and rotational motion, for practical implementations, we need to employ different tidal models to approximate it as a function of the orbital elements of the Earth and the Moon. Fortunately, the detailed evolving history of the lunar orbit shows indifference to a particular model. The most striking finding is that the mutual inclination has a value of 12° when approaching the Earth (Goldreich, 1966; Touma and Wisdom, 1994). However, it disagrees with the giant impact theory which predicts the formation of the Moon is near to the Earth's equator and

thus the initial value is close to zero.

1.4.2 The high mutual inclination and the initial total angular momentum

The high mutual inclination problem has been re-investigated by Touma and Wisdom (1998). With direct numerical simulations, they discover two new phenomena called evection and eviction resonance that have a dramatic impact on the dynamic evolution of the Earth-Moon system. Resonance is a phenomenon of describing increased oscillation amplitude when the frequency of a periodically applied force matches the natural frequency of the system. We can exemplify this interesting phenomenon by the vibration of a harmonic oscillator. If the driving frequency is equal to the natural frequency of the oscillator, the resonance is achieved and the amplitude of the oscillation increases dramatically. This concept can be extended into the planetary science where resonance means a commensurability amongst the frequencies of precession or orbital motions between two planets or stars. If it happens, a periodic gravitational influence will excite the orbital eccentricity or inclination to high values just like the vibration amplitude of an oscillator. The continuous action from the Earth's tidal torque will make the lunar orbital expand and the precession period of the perigee increase (see Figure 13 in Touma and Wisdom, 1998). When this period is close to the orbital period (about one year) of the Earth, the evection resonance happens, and pumps up the eccentricity of the lunar orbit until the tides induced by the Moon and by the Earth cancel out so that the Moon stops moving outward. Then the lunar tide becomes slightly stronger than the tide in the Earth causing the contraction of the lunar orbit. During this stage, the spin rate of the Earth declines in a steady manner until escaping from the evection resonance. After that, the Moon encounters a mixed evection-inclination resonance twice which excites the mutual inclination to 12°.

Touma and Wisdom (1998) found the Moon escapes the evection resonance very fast and only a tiny amount of angular momentum is removed from the Earth-Moon system. However, Ćuk and Stewart (2012) suggest the contraction period is prolonged causing a significant de-spinning of the Earth and efficient removal of the angular momentum to the heliocentric orbit of the Earth. They suggest the initial total angular momentum at the time of the giant impact can be twice as large as the current value. By employing a different tidal model, Wisdom and Tian (2015) and Ward et al. (2020) found too much or too little angular momentum was removed from the Earth-Moon system if the initial angular momentum is high, which is inconsistent with the present Earth-Moon system. Different results obtained from applying different tidal models suggest more work is needed to investigate whether the evection resonance is a viable mechanism to remove the excess angular momentum. Ćuk et al. (2016) proposed a new origin scenario for the Moon. In this model, the Moon is accreted from the disk generated by a high-angular momentum impact with an initial high-obliquity (70°) proto-Earth. The following Laplace plane

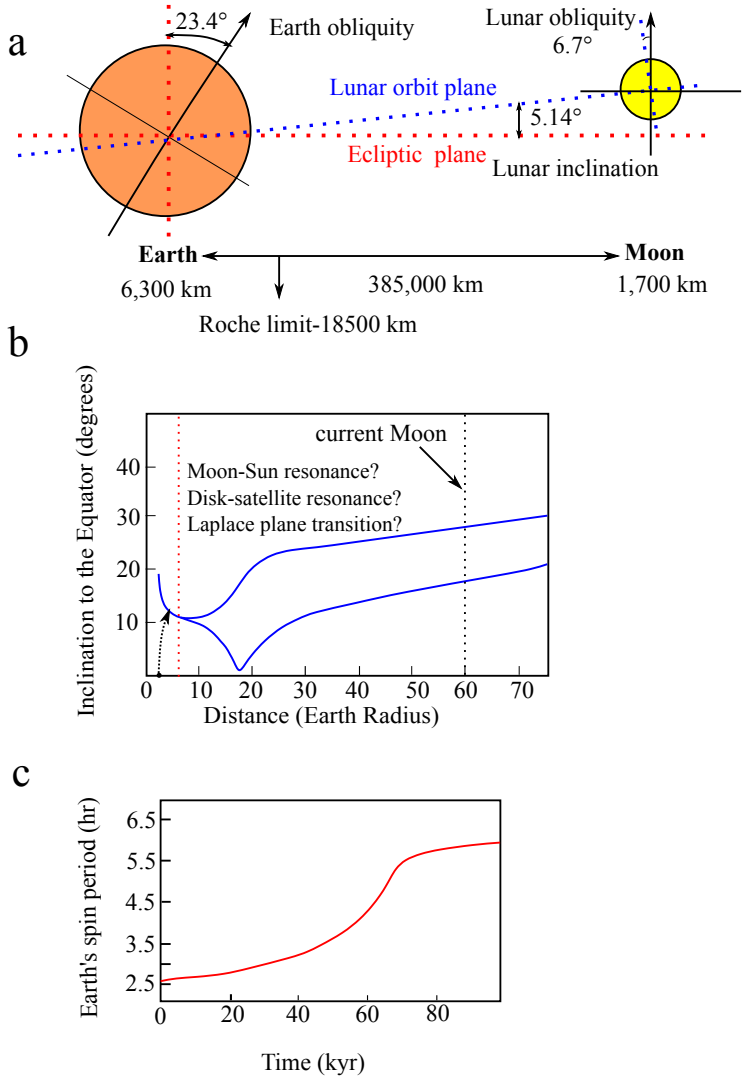

Figure 1.1: The dynamic evolution of the Moon. (a) The lunar orbital elements at present. The inclination of the lunar orbit to the ecliptic plane is 5°. The mutual inclination of the Moon's orbit to the Earth's equator varies from 18° to 28°. (b) The evolution of the mutual inclination as a function of radius. The mutual inclination must be at least 12° when the Moon forms. However, the giant impact theory predicts the moon formed at the Earth's equator predicting an initial value of 0°. This discrepancy can be reconciled with the Moon-Sun resonance (Touma and Wisdom, 1998), the disk-satellite resonance(Ward and Canup, 2000) or the Laplace plane transition (Ćuk et al., 2016), which can excite the mutual inclination to a high value (see the black dashed line in b). This figure is reproduced with permission from Touma and Wisdom (1994). (c) Ćuk and Stewart (2012) have shown the Earth's rotational rate slows down due to the Moon-Sun resonance which can be used to drain away the excess angular momentum. They suggest an initial high angular momentum at the time of the giant impact is dynamically feasible. However, subsequent studies using different tidal models found too much (Wisdom and Tian, 2015) or too little (Ward et al., 2020) angular momentum be removed from the Earth-Moon system, raising the question whether the Moon-Sun resonance is still a viable mechanism. This figure is reproduced with permission from Ćuk and Stewart (2012).

transition will excite the lunar inclination to 30° and reduce the obliquity of the Earth to 20°. This process will also remove the excess angular momentum from the Earth-Moon system and transfer to the heliocentric orbit of the Earth. Once the Moon has passed through the Laplace phase transition, it will undergo the Cassini state transition to achieve the spin-orbit resonance causing a large lunar obliquity (over 30°). The high-obliquity tides in the Moon, in return, will strongly damp the lunar inclination to reach the present value of 5°. However, Tian and Wisdom (2020) found the vertical component of the total angular momentum in the Earth-Moon system, which is perpendicular to the Earth's orbital plane, is almost conserved. They suggest an initial high-obliquity (70°) Earth with a high angular momentum proposed in Ćuk et al. (2016) would result in too large vertical angular momentum that is inconsistent with the present observations.

1.4.3 Summary

The total angular momentum at the time the Moon formed is an essential part of constraining the impact conditions. If there is no mechanism to remove or add angular momentum to the Earth-Moon system, its initial angular momentum is the same as the present Earth-Moon system. Ćuk and Stewart (2012) proposed the Moon-Sun resonance would remove a large amount of angular momentum from the Earth-Moon system. Therefore, the initial angular momentum could be up to two times higher than the present observation. However, Wisdom and Tian (2015) and Ward et al. (2020) found the resonance appears to remove too much to too little angular momentum if the initial angular momentum is high, causing inconsistency with the present Earth-Moon system. Ćuk et al. (2016) suggest that the instability associated with the Laplace plane transition would remove considerable angular momentum from the Earth-Moon system. However, Tian and Wisdom (2020) suggest an initial high obliquity Earth with a high angular momentum proposed in Ćuk et al. (2016) cannot produce the present Earth-Moon system.

1.5 The giant impact theory

1.5.1 Material injection mechanism

Before we are going to discuss in detail the impact process and its geochemical implications, a concise introduction of the material injection mechanism is given. The energetic collision between the impactor and the proto-Earth creates powerful shock waves, which will compress constitutive materials very rapidly to a high pressure and temperature condition. When the shock wave reaches the free space assumed to be a vacuum, to sustain the zero pressure interface a rarefaction wave or a relief wave must be produced. Then it reflects from the free space and travels into the compressed materials to make them expand (Forbes, 2013). As the pressure drops and volume rises during the expansion, the particle velocity of shocked materials would increase, so is the total energy which is defined as the sum of the kinetic

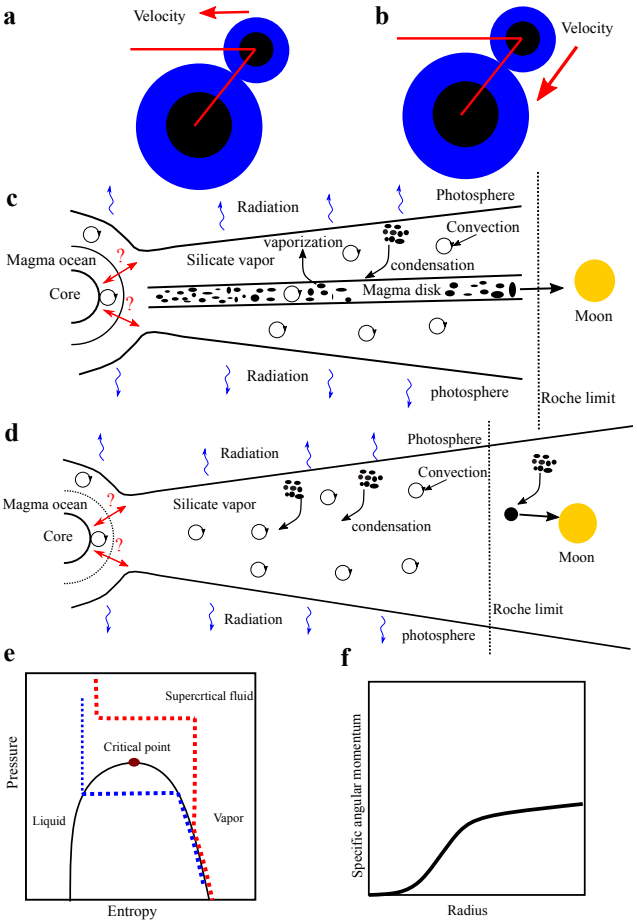

Figure 1.2: In the canonical model (a), the graze collision of a Mars-sized projectile with proto-Earth at a velocity of 10 km/s can generate a disk (b) and leave the total angular momentum of post-impact structure close to the present Earth-Moon system. The disk material is made of silicates liquids with 20 wt% vapor and primarily derived from the impactor, from which the Moon is accreted. Thus the Moon should have a distinct isotope composition compared to the Earth (Canup and Asphaug, 2001). Canup and Esposito (1996) suggest a large amount of mass must be injected directly beyond the Roche limit to form a single lunar-mass satellite. In (b), all materials outside of the Roche limit are represented by a single Moon as the accretion process is very fast on a timescale of years. Due to the Jeans instability the high density magma disk inside the Roche limit will clump and then be sheared apart by the tidal force, which results in an effective viscosity and is much larger than the molecular viscosity (Stevenson, 1987). The entropy file in (e) represented by the blue dashed line is typical for the canonical impact, which indicates the entire structure is thermally stratified. In the high-angular momentum impact model (d), a smaller impactor with a high velocity of 30 km/s hitting a rapid spinning proto-Earth can produce a disk with enough material mixing between colliding bodies to account for the measured isotopic ratios (Ćuk and Stewart, 2012). The post-impact structure is highly thermally stratified (red line in (e)) and the silicate transitions smoothly from liquid to the supercritical fluid to vapor (Lock et al., 2018), which was named as synestia. Besides, there is a smooth change in the angular velocity from the corotating inner region to the sub-Keplerian disk-like region (f).

energy and gravitational potential energy. For the high-angular momentum impact model, we need to include the rotational energy from the pre-impact spin to the total energy as well, which will make the injection more easily.

If the total energy of the injected materials is negative, they will follow a Keplerian orbit with the periapse on the Earth if there are no other materials block their pathway to inject. After one orbital period they will fall back and re-impact with the Earth. In contrast, if the injected materials have a positive total energy, they will escape the Earth's gravitational field. In order to form a proto-lunar disk, we need other mechanisms to lift the periapse of some parts of shocked materials with a negative total energy above the Earth.

One possible mechanism is the gravitational torque (Stevenson, 1987), which pumps the angular momentum into the injected materials to make their orbits lift and avoid to re-impact with the Earth. This mechanism is very similar to the current recession of the lunar orbit due to the tidal torque exerted by the Earth. Another mechanism is the pressure gradient, which becomes important if there is significant vaporization happening during the giant impact. As compression is an irreversible process, the shocked materials will gain entropy in the course to reach the peak pressure and temperature conditions. Then an expansion is followed due to relief waves. As the decompression process happens very fast, convection, viscous dissipation and radiation play a very limited role. We can safely assume this process is isentropic. If the decompressed materials intersect with the liquid-vapor dome, it will turn into the liquid-vapor mixture. The significant volume change from the condensed phase (liquid or solid) to the vapor phase upon vaporization causes an abrupt increase in the particle velocity. Then the outflow materials is subjected to the pressure gradients which is able to lift the periapse of injected materials (see Figure 6 in Stevenson, 1987). Due to the complex impact geometry, how much materials are injected into the proto-lunar disk and which mechanism is dominant can only be determined from hydrodynamic simulations.

1.5.2 The canonical impact model

As the laboratory-scale experiments are not able to simulate such planetary-scale impacts, our understanding of the giant impact mostly comes from hydrodynamic simulations (Fig. 1.2). In this section, I summarize the outcome for the canonical impact modeling. The high angular momentum impact scenario will be analysed in the next section. For simulation results, we are more interested in what kind of impact parameters will produce the present Earth-Moon system, which includes the total mass ($M_{\rm T}$) as a sum of the impactor and the proto-Earth, the impact-to-total-mass ratio (γ), impact angle (b) and the total angular momentum ($L_{\rm imp}$). The simulation details are well beyond my interests.

Benz and Cameron pioneered the application of the SPH method to the giant impact simulations. Interestingly, a series of papers were published in *Icarus* with the same title 'The origin of the Moon and the Single Impact Hypothesis' (Benz et al.,

1986, 1987, 1989; Cameron, 1997; Cameron and Benz, 1991). Due to the limit on the computational speed, all simulations except for in Cameron (1997) have a low resolution. For instance, the total number of particles in the generated proto-lunar disk is only 30 (Benz et al., 1987). From these simulations, they conclude that

1. the low-mass impactors with the impact-to-total-mass ratio less than 0.12 produces iron-rich disk;
2. the gravitational torque is more important than the pressure gradient for materials emplacement, which still holds even in the present high-resolution hydrodynamic simulations.

Cameron (1997) first performed the high-resolution simulations with a total number of particles around $N \sim 10^4$. The most successful impact to produce the current Earth-Moon system is with γ=0.3 and $M_{\rm T}$=0.65$M_{\rm E}$, where $M_{\rm E}$ is the mass of the Earth. This case is also called the early-Earth impact scenario and the Earth needs to acquire extra 0.35$M_{\rm E}$ by the late accretion. Since the Moon will receive a proportional amount of material as well and there is no mechanism available to filter out iron in these materials, the initial iron-depleted Moon will become iron-rich again causing an inconsistency with the geochemical observations. Therefore, the early-Earth impact scenario is not favorable. Canup et al. (2001) re-examined the simulation results in Cameron (1997) and proposed a scaling law to describe the results of satellite-forming impact simulations. They found the disk mass tends to increase and iron content decreases with increasing b for $0.4 < b < 0.8$, which is independent of $M_{\rm T}$. The maximum yielding of the massive and iron-depleted disk is at $b \sim 0.8$. Canup and Asphaug (2001) were guided by this trend and revisited the small impactor case with $\gamma < 0.12$. A total of 36 impact simulations were run with $\gamma = 0.108 - 0.115, b = 0.70 - 1.0, L_{\rm imp} = L_{\rm EM}$ and $M_{\rm T} = M_{\rm E}$, where $L_{\rm EM}$ is the total angular momentum of the present Earth-Moon system. They found a massive proto-lunar disk can be generated to allow the accretion of a single moon. They also confirm most of the materials in the lunar disk is from the impactor with a mass fraction of 0.6-0.74, indicating that the Moon will inevitably have a different oxygen isotope ratio compared to the Earth's mantle.

1.5.3 The high-angular momentum impact model

Ćuk and Stewart (2012) have proposed a new giant impact scenario which can produce a Moon being isotopically similar to the Earth. In this model, a small impactor with a mass around 0.026-0.1 $M_{\rm E}$ but with a high velocity (30 km/s) hits a rapidly spinning Earth. It results in a vapor-dominated disk with enough material mixing between colliding bodies to account for the measured isotopic ratios. The resulted disk has a much high angular momentum and more massive than the one generated by the canonical impact model. However, the successful Moon-forming impact leaves the Earth-Moon system with an excess angular momentum. Ćuk and Stewart (2012) propose the Earth-Moon system can lose angular momentum by the orbital resonance between the Sun and Moon, which is still under debate.

Lock et al. (2018) found the post-impact structure is highly thermally stratified and the silicate transitions smoothly from the liquid phase to the supercritical phase, then to the vapor phase. This special structure was named as synestia. There is also a smooth change in the angular velocity from the corotating inner region to the sub-Keplerian disk-like outer region. The outer part of the disk-like region is likely to be well mixed due to the falling condensates and vertical fluid motion (Lock et al., 2018). However, a whole mixing in the synestia may be difficult. On the one hand, synestia is thermally stratified, meaning the outer part is hot and has a lower density. Lifting denser materials from the inner part to the outer part needs to overcome the gravitational force. On the other hand, the monotonic increase of the specific angular momentum from the inside-out creates a barrier. The exchange of a large amount of materials between the inner part and outer part in the synestia will decrease the angular momentum of the outer part, result in the collapse of the disk-like region and leave too little materials in the disk (Melosh, 2014).

1.5.4 Summary

The giant impact model is the leading theory to explain the formation of the Moon. The classic canonical impact model fails to explain the Moon's isotopic similarity to the Earth, while the high-angular momentum impact model has problems with the removal of the excess angular momentum to match the present Earth-Moon system.

1.6 The behaviour of iron during giant impacts

Both the canonical and high-angular momentum impact models predict the impactor's core merge rapidly into the proto-Earth's core at a timescale of hours (Kraus et al., 2015). Since the chemical exchange between the sinking iron from the impactor and the silicates in the magma ocean requires a much longer time, there is a very limited chemical equilibration between the impactor's core and the Earth's silicate mantle. However, the hafnium-tungsten isotope studies (Kruijer et al., 2015; Touboul et al., 2015) have suggested a substantial level of metal-silicate equilibration is needed to remove siderophile elements almost entirely from the rocky mantle to explain the small excess of ^{182}W of the Earth relative to the Moon. There are two possible mechanisms to enhance equilibration. The first one is to mechanically break the impactor's core into small pieces since the smaller metal pieces would have longer falling time and shorter chemical equilibration time. Dahl and Stevenson (2010) show only iron fragments less than 10 km in diameter would equilibrate with silicates. Kendall and Melosh (2016) have futher revised this value by performing hydrodynamic simulations and found iron blobs with a radius of 100 km is in full equilibrium with the magma ocean. It should be noted that all Moon-forming impact simulations do not include the strength of materials, causing the overestimation of the size of fragmented iron core (Barr, 2016). The second mechanism is vaporisation. After cooling down, the vaporised materials would condensate into a distribution of small droplets on a centimetre level, and thus enhance the metal-

silicate equilibration. Kraus et al. (2015) developed an experimental technique to determine the shock pressure required for vaporization of iron along the principal Hugoniot line. They found the starting vaporization pressure is around 415 GPa compared to 817 GPa from the previous theoretical estimate using ANEOS (Pierazzo et al., 1997). Therefore, previous hydrodynamic simulations with ANEOS may underestimate the production of iron vapor.

Before the giant impact, the proto-Earth's core may grow with stable compositional stratification because higher abundances of light elements would be incorporated into the liquid metal as a result of the increasing metal-silicate equilibration pressure and temperature during accretion (Jacobson et al., 2017). The stable stratification would inhibit the outer-core convection and prevent from generating a geodynamo. Jacobson et al. (2017) proposed that an energetic giant impact may pump enough energy to homogenise the core as long as at least 4% of the total energy is deposited in the core. However, it remains as an open question on the exact amount of energy distributed into the Earth's core during the giant impact, which requires significant numerical simulations to clarify.

1.7 The role of equations of state

During the giant impact, the colliding interface and silicates in the disk can be heated up to 10^4 K and 7000-8000 K, respectively, even in the canonical impact model (Canup, 2004a). More surprisingly, the core of the impactor can reach as high as 45000 K (Canup, 2004a). It remains unclear whether these reported temperatures are physically reasonable and not caused by the equations of state of iron and silicates used in these simulations. For any giant impact simulation, the equations of state (EOS) are needed to describe the thermodynamic properties over a wide range of temperature, pressures and density. It will inevitably affect the energy distribution (Nakajima and Stevenson, 2015) and alter the after-impact dynamic evolution of the Earth such as the core-mantle equilibration and homogenising the compositional strafication of the Earth's core.

There are two sets of equations of state that have been widely used in the hydrodynamic simulations. The first one is called Tillotson EOS, which has a relatively simple analytic formula that makes computations very fast. The shortage is that Tillotson EOS does not provide any information on the physical state of materials. Therefore, simulation results are lack of vapor which may affect the efficiency of the pressure gradient to inject materials into the proto-lunar disk (Stevenson, 1987). The second one is ANEOS, which is more sophisticated and provides a thermodynamically consistent description of the phase diagram of iron and silicates. However, ANEOS treats the vapor phase as a monatomic mixture of atoms rather than the molecular cluster, resulting in an unrealistic large amount of entropy needed to vaporise solid or liquid into the gas. This problem has been solved in the improved version of ANEOS or M-ANEOS (Melosh, 2007). Canup (2004a) has compared the

hydrodynamic simulation results using the Tillotson EOS with that of M-ANEOS, and found no difference in the origin of materials of the proto-lunar disk, where more than 60 wt% is from the impactor. Only more vapor is produced using M-ANEOS as expected, which is still not enough to make the pressure gradient as the major injection mechanism.

1.8 The phase diagram of iron

As a building-block of the terrestrial planet, iron naturally receives a lot of attention on its thermodynamic properties under various conditions. Many experimental techniques have been developed to determine its phase diagram and equation of state. The laser-heated or resistance-heated diamond anvil cell is capable of compressing iron up to 400 GPa and 6000 K (Sinmyo et al., 2019). To reach pressures into the terapascal (TPa) range and temperatures up to 10,000 K or more, the dynamic compression is the only method available. It has been used to measure the physical properties of iron up to 1.4 TPa (Smith et al., 2018). The rapid advance in the computer capability in the last two decades has made *ab initio* simulations feasible. It is capable of accessing pressure and temperature conditions that are difficult to measure experimentally. In addition, theoretical simulations can directly compute the entropy (e.g. Alfe et al., 1999), which is vital to build up an accurate equation of state and is challenging to obtain from experiments.

Figure 1.3 displays the phase diagram for iron in a pressure range of 0-360 GPa and a temperature range of 0 - 8000 K. At ambient conditions, the most stable phase of iron adopts a body-centred cubic (α-bcc) structure and is in a ferromagnetic state. The Curie temperature, which marks a transition from the ferromagnetic state to the paramagnetic state, is about 1043 K. A further phase transition to the face-centred cubic (γ-fcc) structure occurs at 1200 K. In the temperature range of 1670 K to 1815 K, iron adopts the δ-bcc structure again. Above 1815 K, iron starts to melt and becomes liquid. At ambient temperature and with increasing pressure, iron changes into the hexagonal close-packed structure (ε-hcp) at around 16 GPa. This structure is stable up to at least 400 GPa and 6000 K, although recent studies suggest there is a phase transition from ε-hcp to bcc structure (Belonoshko et al., 2017) at the inner core conditions (360 GPa and 6000 K). The triple point between α-bcc, ε-hcp and γ-fcc phase of iron is around 10.5 GP and 753 K. Along the melting curve, there are two triple points. The first one is at 5 GPa and 2000 K coexisted with δ-bcc and γ-fcc phase of iron. The second one is at 90 GPa and 3000 K coexisted with ε-hcp and γ-fcc phase of iron.

A thermodynamically consistent EOS describing the Helmholtz free energy as a function of volume and temperature ($F(V,T)$) requires the entropy information. It is too expansive to perform a series of simulations over a wide range of pressure and temperature conditions to directly determine the entropy. The common practice is to build up a analytic EOS with several adjustable parameters that can be fitted

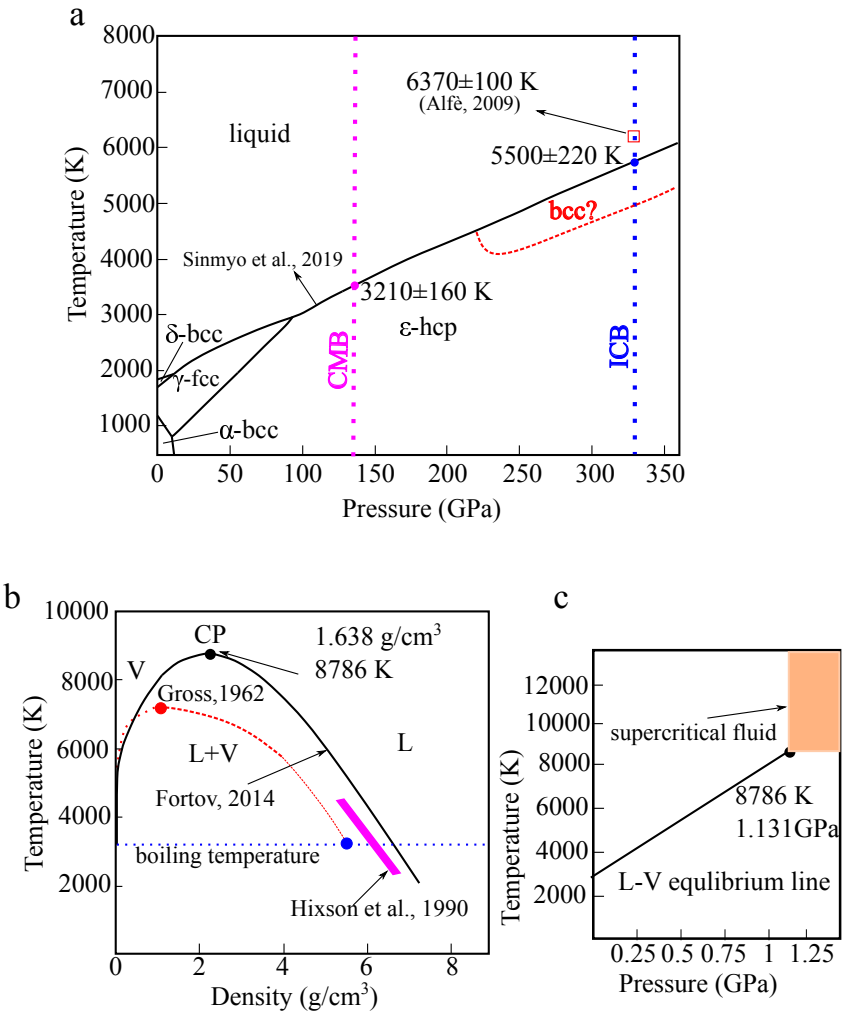

Figure 1.3: (a) The phase diagram of the condensed iron up to 360 GPa and 8000 K. The melting curve was determined by the resistance-heated diamond-anvil cell technique (Sinmyo et al., 2019). The pressure at the core-mantle boundary (CMB) is around 130 GPa. The pressure at the inner-core boundary (ICB) is about 330 GPa. The empty red square is the melting temperature at ICB determined by the *ab initio* method (Alfe, 2009). (b) The liquid-vapor equilibrium line in the temperature-density space. The black solid line and red dotted line represents the liquid-vapor equilibrium line estimated by Fortov and Lomonosov (2010) and Grosse and Kirshenbaum (1963), repectively. The blue point denotes the density of liquid iron at the boiling point of 1 bar. The magenta shared region is the experimental conditions done by Hixson et al. (1990). (c) The liquid-vapor equilibrium line in the temperature-pressure space. The supercritical state is represented by the shaded region.

from the measured or calculated pressure-density-temperature relations and phase boundary of iron (e.g. Dorogokupets et al., 2017). The derived EOS works very well to predict pressure as a function of temperature or density. However, the obtained entropy from $F(V,T)$ are sometimes questionable since it is related to the partial derivative of Helmholtz free energy to the temperature at a fixed volume and thus depends on the particular EOS model. For iron, the magnetic entropy in the paramagnetic phase further increases the complexity. Ruban et al. (2007) employed a microscopic phenomenological model to study the effect of the longitudinal spin fluctuation and found hcp-Fe may acquire a significant magnetic moment at high pressure and temperature. Therefore, future studies are required to clarify whether we need to consider magnetic entropy for all phases of iron.

Above studies are mainly on the condensed phases (>7.8 g/cm^3) of iron. The research into the low-density region near the liquid-vapor equilibrium line is very scarce. Grosse and Kirshenbaum (1963) estimated the critical point of iron based on the rectilinear law and the theorem of corresponding states. The rectilinear law states the density at the boiling point (5.828 g/cm^3 at around 3160 K) is 4.35 times more than that at the critical point. With this in mind, we can determine the critical density which is 1.34 g/cm^3. Then the critical temperature (7000 K) can be extrapolated from the relation between the liquid density and temperature spanning from the melting point to the boiling point. The corresponding law states for a metal, the entropy change along the liquid-vapor equilibrium line is equal for all materials at the same reduced temperature which is defined as the ratio between the physical temperature and the critical temperature. Grosse and Kirshenbaum (1963) have measured the entropy change at the boiling point of 3160 K for iron. This entropy change is equal to that for mercury at a reduced temperature of 0.31. Therefore, the critical temperature of iron is estimated to be about 10000 K (3160/0.31). Considering the significant difference of 3000 K given by these two methods, more work is needed to determine the liquid-vapor equilibrium and the critical point of iron. Hixson et al. (1990) measured the density of liquid iron up to 4000 K in an argon gas atmosphere at a pressure of 0.2 GPa, where the high temperature was generated by the electrical-pulse-heating technique. With an argon-ion laser backlighting the sample, the density was calculated by measuring its sample diameter. Fortov and Lomonosov (2010) has fitted a semi-empirical EOS by using available experimental data from Grosse and Kirshenbaum (1963) and Hixson et al. (1990), and predicted the critical point of iron at 8786 K and 1.638 g/cm^3.

1.9 Proposed research

The lack of reliable information on the thermodynamic properties of iron in the low-density region prevents us from developing an accurate equation of state to describe its thermodynamic response to shock waves. Consequently, it would affect the impact energy distribution and thus cause different geochemical and geodynamic consequences such as the amount of iron vaporized and the extent of iron-silicates

equilibration. The aim of the present work is to close the knowledge gap of the liquid-vapor equilibrium of iron and to improve our understanding of the behavior of iron during giant impacts. In particular, we

1. assess whether the planets' core undergoes partial vaporization during giant impacts (Chapter 3),
2. implement a new technique to compute the liquid-vapor equilibrium and the critical point for a metallic system and validate it with sodium for which experimental data are available (Chapter 4),
3. apply this technique to iron (Chapter 5).

Before that, a brief introduction of first-principles simulation is provided, which is fundamental for our research (Chapter 2). At last, a summary of the results is given and future work is outlined (Chapter 6).

Chapter 2

Ab initio molecular dynamics: a conceptual framework

Contents

2.1 Introduction

In the present study, we employ *ab initio* molecular dynamics (AIMD) and Monte Carlo method to determine the physical properties of iron in the low-density region since it is experimentally difficult to access the low-density and high-temperature conditions. This chapter's focus is on the molecular dynamics method, and the introduction of the Monte Carlo method will be left to Chapter 4. The roadmap of this chapter is as following:

1. We start with the time-dependent Schrodinger equation that governs electron and nucleus dynamics (Eq. 2.1). By applying the Born-Oppenheimer approximation, we show the fast electrons would adiabatically follow the slow nuclei, and stay at the ground state for a large band gap system or the thermal ground state for the small band gap system. If we treat nuclei as classic particles and neglect their quantum effects, the nuclei follow Newton's second law of motion (Eq. 2.10 and 2.9). The force exerted on the ions is obtained from the position

derivative of the electronic potential energy. For a small band gap system, we show the electronic potential energy should include the contribution of the excited states (Eq. 2.11). For a large band gap system, the effect of the excited states is not pronounced, and thus the electronic ground state energy acts as the electronic potential energy.

2. The remaining problem is how to obtain the electronic potential energy, where the electron excited states must be included since we focus on the metallic iron at high temperature. The direct method is to find all eigenfunctions and eigenvalues for the electronic Hamiltonian. But for this, we need to know the kinetic energy and electron-electron coulomb energy operators for the interacting electron system. One the one hand, these terms are unknown. On the other hand, it is extremely difficult to find numerical solutions. Finite-temperature density functional theory provides an alternative and cost-effective way. It shows the electronic potential energy is a unique functional of the electronic density. It simplify the problem since there are only three spatial coordinates in the electronic density. In order to find the thermal ground state electronic density, the Kohn-Sham scheme maps the interacting electron system onto a fictitious non-interacting system, where they share the same thermal ground state electronic density. The solution of Kohn-Sham equation leads to the electronic potential energy.

3. Although the iron atom in the solid phase below or close to the Curie temperature and at ambient pressure contains a non-vanishing magnetic moment, whether the liquid iron at a high temperature like 3500 K is still magnetic is uncertain. But if it does, we need to consider spin dynamics that occur in the paramagnetic state. However, the finite-temperature density functional theory and its spin-polarized extension fail to describe the magnetism at high temperature as they fail to capture the longitudinal and transversal fluctuation.

Since the aim is to build a conceptual framework, the mathematical vigour and proof are not pursued. Any reader being interested in mathematical physics may refer to the excellent book by Eschrig (1996) for more details.

2.2 Deriving classical molecular dynamics

For a system with N nuclei and N_e electrons, The starting point of our discussion is the time-dependent Schrodinger equation,

$$\mathrm{i}\hbar\frac{\partial\Psi(\{\boldsymbol{R}\}_N,\{\boldsymbol{r}\}_{N_e},t)}{\partial t}=H\Psi(\{\boldsymbol{R}\}_N,\{\boldsymbol{r}\}_{N_e},t), \tag{2.1}$$

where $\{\boldsymbol{r}\}_{N_e}$ and $\{\boldsymbol{R}\}_N$ denote a set of electron and nuclei coordinates, $\hbar$ is the reduced Planck constant, t is the time and H is the total Hamiltonian operator

Table 2.1: A summary of symbols used in Section 2.2.

H	the total Hamiltonian operator of the system
T_e	the kinetic energy operator of electrons
T_i	the kinetic energy operator of ions
V_{e-e}	the electron-electron Coulomb interaction operator
V_{e-i}	the electron-ion Coulomb interaction operator
V_{i-i}	the ion-ion Coulomb interaction operator
N	the total number of nuclei in the system
N_e	the total number of electrons in the system
$\{\boldsymbol{R}\}_N$	a set of nuclear coordinates $\{\boldsymbol{R}_0, \boldsymbol{R}_1, .., \boldsymbol{R}_N\}$
$\{\boldsymbol{r}\}_{N_e}$	a set of electronic coordinates $\{\boldsymbol{r}_0, \boldsymbol{r}_1, .., \boldsymbol{r}_{N_e}\}$
$\Psi(\{\boldsymbol{R}\}_N, \{\boldsymbol{r}\}_{N_e}, t)$	the total wavefunction describing the dynamics of electrons and nuclei
H_{fast}	the Hamiltonian governing the fast degrees of motion in H
H_{slow}	the Hamiltonian governing the slow degrees of motion in H
$\Phi_l(\{\boldsymbol{r}\}_{N_e}; \{\boldsymbol{R}\}_N)$	the eigenfunction of H_{fast} at fixed $\{\boldsymbol{R}\}_N$
$E_l(\{\boldsymbol{R}\}_N)$	the eigenvalue of H_{fast} at fixed $\{\boldsymbol{R}\}_N$
l	the electronic state (For instance, $l = 0$ denotes the ground state $E_0(\{\boldsymbol{R}\}_N)$)
$\chi_l(\{\boldsymbol{R}\}_N, t)$	the expansion coefficient to expand $\Psi(\{\boldsymbol{R}\}_N, \{\boldsymbol{r}\}_{N_e}, t)$ by $\{\Phi_l(\{\boldsymbol{r}\}_{N_e}; \{\boldsymbol{R}\}_N)\}$
$F_0(\{\boldsymbol{R}\}_N)$	the effective potential energy governing the ions' motion in small band gap system
$E_0(\{\boldsymbol{R}\}_N)$	the potential energy governing the ions' motion in large band gap system
$\boldsymbol{P}_i$	the momentum of the ith nucleus

defined as,

$$H = T_e + T_i + V_{e-e} + V_{e-i} + V_{i-i}, \tag{2.2}$$

where T_e and T_i are the kinetic energy operator of electrons and ions, respectively, V_{e-e}, V_{i-i} and V_{e-i} are the electron-electron, electron-nuclear and nuclear-nuclear Coulomb interaction operator, respectively. Here the electron coordinates do not include the spin degrees of freedom meaning spatial orbitals are the same in their spin-up and spin-down electrons so that the band occupancy can be up to 2.

As the computational cost increases as the square of the number of coordinates, we need to avoid treating a large amount of coordinates simultaneously. To solve this problem, we can employ the Born-Oppenheimer (BO) approach (Born and Huang, 1954) to separate the fast electronic motion from the slow nuclear motion and to divide the total Hamiltonian into two parts,

$$H_{\text{fast}} = T_e + V_{e-e} + V_{e-i} + V_{i-i} \tag{2.3}$$

$$H_{\text{slow}} = T_i. \tag{2.4}$$

The solution of Eq. 2.3 at fixed nuclei configurations $\{\boldsymbol{R}\}_N$ is given by,

$$H_{\text{fast}}\Phi_l(\{\boldsymbol{r}\}_{N_e}; \{\boldsymbol{R}\}_N) = E_l(\{\boldsymbol{R}\}_N)\Phi_l(\{\boldsymbol{r}\}_{N_e}; \{\boldsymbol{R}\}_N), \tag{2.5}$$

where $\Phi_l(\{\boldsymbol{r}\}_{N_e}; \{\boldsymbol{R}\}_N)$ and $E_l(\{\boldsymbol{R}\}_N)$ are resulted eigenfunction and eigenvalue,

here and thereafter the parametric dependence of any function on the nuclear coordinates is indicated by the symbol after the semicolon, and l denotes the electronic state. We stress that the parametric dependence means that $\frac{d\Phi_l(\{\boldsymbol{r}\}_{N_e};\{\boldsymbol{R}\}_N}{d\boldsymbol{R}_i}$ is always zero but $\frac{dE_l(\{\boldsymbol{R}\}_N)}{d\boldsymbol{R}_i}$ may and may not be zero, where i denotes the ith nucleus.

If Eq. 2.5 is known for all nuclei configurations, we can expand the total wavefunction Ψ as,

$$\Psi(\{\boldsymbol{R}\}_N, \{\boldsymbol{r}\}_{N_e}, t) = \sum_{l=0}^{\infty} \Phi_l(\{\boldsymbol{r}\}_{N_e}; \{\boldsymbol{R}\}_N)\chi_l(\{\boldsymbol{R}\}_N, t), \tag{2.6}$$

where $\chi_l(\{\boldsymbol{R}\}_N, t)$ is the expansion coefficient. The insertion of Eq. 2.6 into Eq. 2.1 followed by exploiting the orthonormalization condition of yields a coupled differential equations (see Eq. (2.6) in Marx and Hutter, 2009), which is challenging to handle. Therefore, some approximations need to be made to simplify the problem.

2.2.1 The large band gap system

For a system at a temperature that is much lower than its band gap, we can ignore the mixing between different electronic levels in Eq. 2.6 and use only the first term to expand the total wavefunction Ψ,

$$\Psi(\{\boldsymbol{R}\}_N, \{\boldsymbol{r}\}_{N_e}, t) = \Phi_0(\{\boldsymbol{r}\}_{N_e}; \{\boldsymbol{R}\}_N)\chi_0(\{\boldsymbol{R}\}_N, t). \tag{2.7}$$

where $\Phi_0(\{\boldsymbol{r}\}_{N_e}; \{\boldsymbol{R}\}_N)$ is the ground state wavefunction, defined in Eq. 2.5. It means electron always stays in its ground state ($l = 0$). Plugging the right-hand side term of both Eq. 2.7 and Eq. 2.5 into Eq. 2.1 leads to,

$$i\hbar\frac{\partial\chi_0(\{\boldsymbol{R}\}_N, t)}{\partial t} = (H_{\text{slow}} + E_0(\{\boldsymbol{R}\}_N)\chi_0(\{\boldsymbol{R}\}_N, t) \tag{2.8}$$

where $E_0(\{\boldsymbol{R}\}_N)$ is ground state energy ($l = 0$) at the fixed nuclei configuration $\{\boldsymbol{R}\}_N$ as defined in Eq. 2.5 when $l = 0$. If we treat the nuclei as classic particles and neglect the quantum effects, Eq. 2.8 can be transformed into,

$$M_i\frac{d\boldsymbol{R}_i^2}{dt^2} = -\nabla_i E_0(\{\boldsymbol{R}\}_N), \tag{2.9}$$

where M_i is the mass of the ith nucleus (Marx and Hutter, 2009).

Since the de Broglie thermal wavelength of an iron atom is much less than the average atomic distance in fluid iron, it may be reasonable to negelect the nuclei quantum effects (Hansen and McDonald, 2013). Approximating $\Psi(\{\boldsymbol{R}\}_N, \{\boldsymbol{r}\}_{N_e}, t)$ with only one term in Eq. 2.7 and neglecting the quantum effects of nuclei inevitably cause errors, which are supposed to be small. We have to live with it in order to

find a numerical solution.

2.2.2 The small band gap and metallic system

For a system that has a small band gap or is metallic like iron at high temperature (T) , we can expand Ψ in a similar way as Eq. 2.7 but needs to take into account the thermal excitation of electrons explicitly. The electronic subsystem cannot be described by a pure state but by a mixed state (Eq. 2.14). We can employ the similar procedure as in Section 2.2.1, which leads to,

$$M_i \frac{d\boldsymbol{R}_i^2}{dt^2} = -\nabla_i F_0(\{\boldsymbol{R}\}_N), \tag{2.10}$$

$$F_0(\{\boldsymbol{R}\}_N) = -\frac{1}{\beta} \ln \mathrm{Tr} \exp\left(-\beta H_{\mathrm{fast}}\right) \tag{2.11}$$

where $\beta = 1/k_{\mathrm{B}}T$, k_{B} is the Boltzmann's constant and $F_0(\{\boldsymbol{R}\}_N)$ is the effective potential energy of the electron subsystem at fixed nuclei configurations $\{\boldsymbol{R}\}_N$ including the free energy of the electrons and the coulombic attraction within nuclei. The details on the derivation of Eq. 2.11 can be found in Zwanzig (1957).

Eq. 2.11 suggests that electrons response instantaneously to the ionic motions and reach the thermal equilibrium (Alavi et al., 1994). We can also re-write Eq. 2.10 in a more compact way (Zwanzig, 1957) that will be used in Chapter 4,

$$\mathcal{Z} = \frac{1}{N! h^{3N}} \int\int \exp\left(-\beta\Big(\sum_{i=1}^{N} \frac{\boldsymbol{P}_i^2}{2M_i} + F_0(\{\boldsymbol{R}\}_N)\Big)\right) \prod_i^N d\boldsymbol{R}_i d\boldsymbol{P}_i. \tag{2.12}$$

where $\mathcal{Z}$ is the canonical partition function, N is the total number of ions, and $\boldsymbol{P}_i$ is the momentum of the ith nucleus. In Eq. 2.12, the electronic contribution to the partition function has been treated in a quantum-mechanical way, while the nuclei has been treated in a classic way under the action of the free energy of the electron system (Eq. 2.11).

2.2.3 Summary

In summary, this section has presented a practical way to solve Eq. 2.1 by separating the electronic motions from the nuclear motions. If we treat nuclei as classic particles and neglect their quantum effects, the nuclei follow Newton's second law of motion (Eq. 2.10 and 2.9). The force is obtained from the position derivative of the electronic potential energy. For the metallic system like iron, the electronic potential energy should include the contribution of the excited states (Eq. 2.11). In order to maintain the temperature of the system at a desired value (T), the Nosé thermostat (Nosé, 1984) is used. The conserved quantity becomes (Wentzcovitch et al., 1992),

$$E_{\mathrm{total}} = F_0(\{\boldsymbol{R}\}_N) + K_i + U_{\mathrm{thermo}} + K_{\mathrm{thermo}}. \tag{2.13}$$

where K_i the kinetic energy of ions, U_{thermo} and K_{thermo} are the potential and kinetic energy of the thermostat, respectively. It should be noted that Wentzcovitch et al. (1992) suggest $F_0(\{\boldsymbol{R}\}_N)$ can be calculated at an arbitrary temperature. However, we have shown in Eq. 2.11 that the electron subsystem must stay at the simulated temperature (T). For the sake of simplicity, we omit hereafter the parametric dependence of $\Phi_l(\{\boldsymbol{r}\}_{N_e};\{\boldsymbol{R}\}_N)$ on the ionic position $\{\boldsymbol{R}\}_N$. We also neglect the dependence of any function on independent variables like $\{\boldsymbol{R}\}_N$ and $\{\boldsymbol{r}\}_{N_e}$. For instance, $F_0(\{\boldsymbol{R}\}_N)$ will be written as F_0.

2.3 Finite-temperature density functional theory

Table 2.2: A summary of symbols used in Section 2.3.

F_0	same as $F_0(\{\boldsymbol{R}\}_N)$ but omitting its dependence on $\{\boldsymbol{R}\}_N$
Γ	a density matrix to describe the electronic subsystem at high temperature
$\{\psi_l\}$	an arbitrarily complete orthonormal basis set in the N_e particle Hilbert space
p_l	the probability of the system being found in the state ψ_l
$F[\Gamma]$	the Helmholtz free energy of the electronic subsystem as described by Γ
Γ_0	the density matrix to give the minimal $F = F_0$ for the electron subsystem
$\{\Phi_{0l}\}$	a complete orthonormal basis set to form Γ_0, and equal to $\Phi_l(\{\boldsymbol{r}\}_{N_e};\{\boldsymbol{R}\}_N)$
p_{0l}	the probability of the system being found in the state Φ_{0l}
n	the electron density
S	the entropy of an interacting electron system
ν_{ext}	the external potential due to electron-ion interactions V_{e-i}
Ω	the grand potential energy in the grand canonical ensemble
n_0	the ground state electron density that gives F_0
T_e	the kinetic energy of a non-interacting electron system
S_s	the entropy of a non-interacting electron system
$J[n]$	the classic Coulomb energy for a non-interacting electron system
$F_{xc}[n]$	the exchange-correlation contribution to the free energy
ν_{ks}	the Kohn-Sham external potential
ϕ_l	an arbitrarily complete orthonormal basis set in the single particle Hilbert space
f_l	the probability of the system being found in the state ϕ_l

2.3.1 Finite-temperature canonical-ensemble theory

In Eq. 2.11, the evaluation of F_0 requires information of all eigenvalues and eigenstates of H_{fast}, which needs a tremendous computational cost. The minimum principle may provide an alternative method that is easier to implement. Before describing this theorem, we need to introduce some terminology. For the canonical ensemble considering here, the electron subsystem is described by a density matrix, which is characterized by a probability distribution over all pure states that have the same particle number N_e,

$$\Gamma = \sum_{l=1}^{\infty} p_l \left|\psi_l\right\rangle \left\langle\psi_l\right|, p_l \geq 0, \sum_{l}^{\infty} p_l = 1 \tag{2.14}$$

where the Dirac bra-ket notation is used, $\{\psi_l\}$ forms a arbitrarily complete orthonor-

mal basis set in the N_e particle Hilbert space and is not necessarily equal to the eigenstates of H_{fast}, and p_l is the probability of the system being found in the state $|\psi_l\rangle$. Then we can define the Helmholtz free energy F as,

$$F[\Gamma] = F[\{p_l, \psi_l\}] = \sum_{l=1}^{\infty} p_l(\frac{1}{\beta}\ln p_l + < \psi_l|T_e + V_{e-e} + V_{e-i}|\psi_l >) + V_{i-i}. \quad (2.15)$$

The quantum statistical mechanics has shown in the thermal equilibrium, the Helmholtz free energy is at its minimum (see Chapter 3 in Parr and Yang, 1989),

$$F[\Gamma] \geq F[\Gamma_0] = F[\{p_{0l}, \Phi_{0l}\}] = F_0 \quad (2.16)$$

where Φ_{0l} are the eigenstates of H_{fast} at the fixed configuration $\{\boldsymbol{R}\}_N$, and p_{0l} is defined as,

$$p_{0l} = \frac{\exp(-\beta E_l)}{\sum_i^{\infty} \exp(-\beta E_l)}, \quad (2.17)$$

where E_i is the eigenvalues of H_{fast}. Eq. 2.16 sets up the variational principle to find F_0. However, the computational complexity is very similar to the direct calculation of eigenvalues and eigenstates of H_{fast}.

A more cost-effective method is density functional theory (DFT), which allows to perform the minimization over the electron density which depends on only three spatial coordinates. For a system with non-degenerate ground state, the Hohenberg-Kohn (HK) theorem (Hohenberg and Kohn, 1964) proves there is one-to-one correspondence between the external potential, the resulted non-degenerate ground state, and the associated ground state density. Therefore, any ground state observable including the ground state energy is a unique functional of electron density. The extension of this theorem to high temperature was pioneered by Mermin (1965), just one year after Hohenberg and Kohn published their seminal work. For the discussion of finite-temperature density functional theory, we need to define ensemble N-representable electron density associated with a density matrix (Γ) defined in Eq. 2.14 as,

$$n(\boldsymbol{r}) = N_e \sum_{l=0}^{\infty} p_l \int d^3\boldsymbol{r}_2 \int d^3\boldsymbol{r}_3 \cdots \int d^3\boldsymbol{r}_N \psi_l^*(\boldsymbol{r}, \boldsymbol{r}_2, \ldots, \boldsymbol{r}_N)\psi_l(\boldsymbol{r}, \boldsymbol{r}_2, \ldots, \boldsymbol{r}_N). \quad (2.18)$$

and rewrite the electron-nuclear Coulomb interaction operator in Eq. 2.5 as a functional of the electron density,

$$V_{e-i} = \int d^3\boldsymbol{r}\nu_{\text{ext}}(\boldsymbol{r})n(\boldsymbol{r}). \quad (2.19)$$

where ν_{ext} is the external potential due to electron-ion interactions. Mermin (1965) proved that in the grand canonical ensemble at a given temperature and chemical

potential, no two external potentials can lead to the same equilibrium density. This suggests the grand potential is a unique functional of electron density. Based on this fact, we can define a universal functional ($F_L[n]$) of the electron density which is independent of the external potential and the quantity

$$\Omega[n] = \int d\boldsymbol{r}\nu_{\text{ext}}n(\boldsymbol{r}) + F_L[n] \tag{2.20}$$

is at its minimum and equal to the grand potential Ω_0 when $n(r)$ is the equilibrium density $n_0(r)$. Mermin (1965) also mentioned about these arguments can be adapted to the canonical ensemble with a few minor changes, which has been given in the Chapter 3 of Parr and Yang (1989). With the help of the Lieb functional, we can contruct the density functional theory for the minimum principle in Eq. 2.15 as,

$$F_0 = \min_n F[n] = \min_n(F_L[n] + V_{e-i}[n]) + V_{i-i} \tag{2.21}$$

where the minimization is performed over all ensemble N-representable electron densities defined in Eq. 2.18, and $F_L[n]$ is a universal density functional independent of the external potential ν_{ext},

$$\begin{aligned} F_L[n] &= T_e[n] + V_{e-e}[n] + S[n] \\ &= \min_{\{\psi_l,p_l\}\to n} \sum_i^\infty p_l(\langle\psi_l|\, T_e\,|\psi_l\rangle + \langle\psi_l|\, V_{e-e}\,|\psi_l\rangle + \frac{1}{\beta}\ln p_l) \end{aligned} \tag{2.22}$$

where $\{\psi_l, p_l\} \to n$ is a constrained search over all sets $\{\psi_l, p_l\}$ that can generate n and $S[n]$ is the entropy of the interacting electron system. For more details on the Lieb functional and N-representable electron density, please refer to Chapter 2 in Engel and Dreizler (2013). If the definition domain of $F[n]$ includes densities that integrate to a fractional number of particles and $\frac{\delta F}{\delta n}$ exits, the minimum principle in Eq. 2.21 indicates it is possible to determine the ground state density by a variational equation,

$$\frac{\delta}{\delta n(\boldsymbol{r})}F[n] - \mu(\int d^3\boldsymbol{r}n(\boldsymbol{r}) - N_e) = 0 \tag{2.23}$$

where the Lagrange multiplier μ is used to impose the constraint,

$$\int d^3\boldsymbol{r}n(\boldsymbol{r}) = N_e. \tag{2.24}$$

2.3.2 Kohn-Sham formulation

We have built a varitional principle to find the F_0 based on Eq. 2.23. However, we still have no information on how to calculate $\langle\psi_l|\, T_e\,|\psi_l\rangle$ and $\langle\psi_l|\, V_{e-e}\,|\psi_l\rangle$. The Kohn-Sham formulation (Kohn and Sham, 1965) employs a mapping from the full interacting system with $V_{e-e} \neq 0$ onto a fictitious non-interacting ($V_{e-e} = 0$) system

where the electrons move within an effective potential ν_{ks},

$$\nu_{\text{ext}} \xleftrightarrow{V_{e-e}\neq 0} n_0 \xleftrightarrow{V_{e-e}=0} \nu_{\text{ks}}, \tag{2.25}$$

where we have assumed interacting ensemble N-representable electron density is also non-interacting ensemble N-representable. The Kohn-Sham method is exact since the non-interacting system yields the same ground-state density as the real system. We can then transformed Eq. 2.21 into,

$$\begin{aligned} F_0 &= \min_{n(\boldsymbol{r})}(T_e[n] + V_{e-e}[n] + S[n] + V_{i-i})(\text{interacting electron system}) \\ &= \min_{n(\boldsymbol{r})}(T_s[n] + J[n] + F_{xc}[n] + S_s[n] + V_{i-i})(\text{non-interacting electron system}) \end{aligned} \tag{2.26}$$

T_s is the kinetic energy of non-interacting electron system, S_s is the entropy of non-interacting electron system, $J[n]$ is the classic Coulomb energy by,

$$J[n] = \int d\boldsymbol{r} \int d\boldsymbol{r}' \frac{n(\boldsymbol{r}')n(\boldsymbol{r})}{|\boldsymbol{r}' - \boldsymbol{r}|}, \tag{2.27}$$

and $F_{xc}[n]$ is the exchange-correlation contribution to the free energy that includes the difference of the kinetic energy, entropy and Coulomb energy between the interacting electron system and the non-interacting electron system,

$$F_{xc}[n] = (T[n] + S[n]) - (T_s[n] + S_s[n]) + (V_{e-e}[n] - J[n]). \tag{2.28}$$

For the non-interesting system, we can express the electron density n with respect to the single particle states as,

$$n(\boldsymbol{r}) = \sum_{l=0}^{\infty} f_l \phi_l^*(\boldsymbol{r})\phi_l(\boldsymbol{r}), f_l \geq 0, \sum_{l=0}^{\infty} f_l = 1 \tag{2.29}$$

where $\{\phi_l\}$ forms a arbitrarily complete orthonormal basis set in the single particle Hilbert space and and f_l is the probability of the system being found in the state $|\phi_l\rangle$.

Plugging Eq. 2.29 into Eq. 2.26 leads to,

$$\begin{aligned} F_0 = \min_{\{\phi_l, f_l\}} \Big(\sum_{l=0}^{\infty} [f_l \langle \phi_l | - \frac{1}{2}\nabla^2 |\phi_l\rangle + \frac{1}{\beta}(f_l \ln f_l + (1-f_l)\ln(1-f_l))] \\ + \int d\boldsymbol{r} \int d\boldsymbol{r}' \frac{n(\boldsymbol{r}')n(\boldsymbol{r})}{|\boldsymbol{r}' - \boldsymbol{r}|} + F_{xc}[n] \Big) \end{aligned} \tag{2.30}$$

Based on the conclusion in Eq. 2.16, the minimization is obtained if ϕ_l are the

eigenfunctions

$$[-\frac{1}{2}\nabla^2 + \nu_{ks}(\boldsymbol{r})]\phi_l(\boldsymbol{r}) = \varepsilon_l\phi_l(\boldsymbol{r}) \tag{2.31}$$

and f_l is

$$f_l = \frac{1}{1+\exp[\beta(\varepsilon_l - \mu])} \tag{2.32}$$

where ε_l is the eigenvalues and μ is the chemical potential calculated from the constraint,

$$\sum_{l=0}^{\infty} f_l = N_e \tag{2.33}$$

and ν_{ks} is defined as,

$$\nu_{\mathrm{ks}}(\boldsymbol{r}) = \nu_{\mathrm{ext}}(\boldsymbol{r}) + \int \frac{n(\boldsymbol{r}')}{|\boldsymbol{r}-\boldsymbol{r}'|} + \frac{\delta F_{xc}[n]}{\delta n}. \tag{2.34}$$

Eq. 2.31 have to be solved self-consistently. And the resulted equilibrium density can be inserted into Eq. 2.26 to obtain F_0 (see Chapter 9 in Parr and Yang, 1989).

In the finite-temperature density functional theory, the physically meaningful quantity is F_0 and its analytic derivative with respect to the atomic position and cell volume from which the force and electronic pressure are calculated. It is questionable to use the quantity $F_0 - S_s$ as the internal energy for the interacting electron system since S_s is the electronic entropy of the fictitious non-interacting electron system. Besides, we cannot determine the heat capacity for the metallic system based on the fluctuation-dissipation theorem since FT-DFT provides no information on the fluctuation of the electronic internal energy.

2.4 *Ab initio* spin dynamics

2.4.1 Spin-polarized DFT at zero temperature

Magnetism comprises a large variety of phenomena that can be characterized by quantities such as the magnetic moment, the magnetic order and the ordering temperature and so on. Although there is no single theoretical approach to all magnetic phenomena, the spin-polarized version of DFT allows the access to the magnetic moment and the magnetic order at zero temperature. It can also serve to extract other quantities like exchange interactions that can serve as input for other theoretical approaches. In this section, we will present how to extend the Kohn-Sham formulation described in Section 2.3.2 to the spin-polarized case at zero temperature.

The basic variables of spin density functional theory are the scalar electronic density $n(\boldsymbol{r})$ and the vector of the magnetization density $\boldsymbol{m}(\boldsymbol{r})$. von Barth and Hedin (1972) have extended the DFT concept to spin-polarized systems by defining the

Hohenberg-Kohn-Sham spin density functional as,

$$E_0[n(\boldsymbol{r}),\boldsymbol{m}(\boldsymbol{r})] = \min_{n(\boldsymbol{r}),\boldsymbol{m}(\boldsymbol{r})}[T_e[n(\boldsymbol{r}),\boldsymbol{m}(\boldsymbol{r})] + V_{e-e}[n(\boldsymbol{r}),\boldsymbol{m}(\boldsymbol{r})] + V_{i-i}] \tag{2.35}$$

It means the internal energy is at a minimum when $n(\boldsymbol{r})$ and $\boldsymbol{m}(\boldsymbol{r})$ are the equilibrium electron and magnetization density, repectively. Here we choose the internal energy E_0 instead of the free energy F_0 since the electronic entropy at zero temperature is zero and $E_0 = \lim_{T\to 0} F_0$. Then we can map the interacting electron system to a non-interacting electron system and express $n(\boldsymbol{r})$ and $\boldsymbol{m}(\boldsymbol{r})$ with respect to the single particle states. The details are not given here, which can be found in Bihlmayer (2007). In this way, we are able to derive a spin-polarized version of Kohn-Sham equations without a magnetic field,

$$\left[\left(-\frac{1}{2}\nabla^2 + \int\frac{n(\boldsymbol{r}')}{|\boldsymbol{r}-\boldsymbol{r}'|} + \nu_{\text{ext}}(\boldsymbol{r})\right)\begin{pmatrix}1 & 0\\ 0 & 1\end{pmatrix} + \frac{\delta E_{xc}}{\delta \underline{n}(\boldsymbol{r})}\right] \times \begin{pmatrix}\phi_l^{\uparrow}\\ \phi_l^{\downarrow}\end{pmatrix} = \varepsilon_l \times \begin{pmatrix}\phi_l^{\uparrow}\\ \phi_l^{\downarrow}\end{pmatrix}, \tag{2.36}$$

where $\uparrow$ and $\downarrow$ denote the spin-up and spin-down states, and the density matrix is defined as,

$$\underline{n}_{\alpha,\beta}(\boldsymbol{r}) = \sum_{l=1}^{\infty}\phi_l^{*,\alpha}(\mathrm{r})\phi^{\beta}(\mathrm{r}), \alpha,\beta = \uparrow \text{ or } \downarrow . \tag{2.37}$$

It can be decomposed into a scalar and vectorial part, correponding to the charge and magnetization density,

$$\underline{n}(\boldsymbol{r}) = \frac{1}{2}\left[n(\boldsymbol{r})\begin{pmatrix}1 & 0\\ 0 & 1\end{pmatrix} + \underline{\boldsymbol{\sigma}}\boldsymbol{m}(\boldsymbol{r})\right] = \frac{1}{2}\begin{pmatrix}n(\boldsymbol{r}) + m_z(\boldsymbol{r}) & m_x(\boldsymbol{r}) - im_y(\boldsymbol{r})\\ m_x(\boldsymbol{r}) + im_y(\boldsymbol{r}) & n(\boldsymbol{r}) - m_z(\boldsymbol{r})\end{pmatrix}, \tag{2.38}$$

where $\underline{\boldsymbol{\sigma}}$ is the Pauli matrices. And the magnetic moment is defined as,

$$\boldsymbol{M}_I = \int_{\Omega_I}\boldsymbol{m}(\boldsymbol{r})d\boldsymbol{r}, \boldsymbol{e}_I = \frac{\boldsymbol{M}_I}{|\boldsymbol{M}_I|}, \tag{2.39}$$

where Ω_I is a sphere centered at Ith atom and $\boldsymbol{e}_I$ is the orientation of the local magnetic moment.

2.4.2 Spin dynamics at high temperature

We can use the method described in the last section to simulate magnetic systems and determine their ground state accurately. But at high temperature, we need to consider the magnetic excitations consisting of the Stoner single particle and collective excitation (Kaul, 2007). The single particle excitation is due to the transfer of an electrons-hole pair in the band of opposite spins. The collective excitation is caused by a spin flip from atom to atom and can be further divided into the transversal and longitudinal fluctuation (Kaul, 2007). They would change the orientation and magnitude of the local magnetic moment from one site to the other, respec-

tively. When the temperature reaches the Curie point or above, the transversal and longitudinal fluctuation destroy the long-range magnetic order and the ferromagnetic system would become paramagnetic. However, the individual atom may still contain a non-vanishing magnetic moment. We can explain the presence of spin dynamics or magnetic excitations at high temperatures by analogy with atom vibrations in a perfect lattice. For the NVT ensemble in thermodynamic equilibrium, the Helmholtz free energy should be at its minimum. At high temperatures, atom vibration increases the internal energy but brings in extra entropy due to the increased disorder. The overall effect is the entropy gain is larger than the cost of the increasing internal energy. Similarly, although spin dynamics increases the internal energy, the system would obtain more entropy due to the magnetic disorder.

Electronic structure calculations within DFT can be viewed as a modern extension of the Stoner-type description of magnetism (Abrikosov et al., 2016). It is capable of reproducing ground-state magnetic properties of 3d transition metals accurately, whose magnetism comes from the imbalance between the number of spin-up and spin-down itinerant 3d electrons. However, DFT fails to describe the magnetism at finite temperature and significantly overestimates the Curie temperatures of iron by a factor of five due to its inability of treating the transversal and longitudinal fluctuation (Abrikosov et al., 2016).

To find a scheme to capture these fluctuations at high temperatures, we start again with the time-dependent Schrodinger equation but need to include the spin degrees of freedom explicitly, then precede to separate different dynamic time scales. Following this, Antropov et al. (1995) partition the total Hamiltonian into a slow-motion part that relates to the spin density and nuclear motion. By introducing the rigid spin approximation and neglecting the longitudinal fluctuation, the time evolution of the spin density is described by a rotation of the magnetization density inside the atomic spheres. The remaining electronic Hamiltonian at fixed atomic positions and the local magnetic moment direction plays the role of the potential energy for the movement of nuclei and the magnetic moment direction. Therefore, we can write the equation of motion for the direction of the local magnetic moment and nuclei (Ma et al., 2017) as,

$$\mathcal{Z} = \frac{1}{N!h^{3N}} \int\int\int \exp\left(-\beta\Big(\sum_{I=1}^{N} \frac{\boldsymbol{P}_I^2}{2M_I} + F_0(\{\boldsymbol{R}\}_N, \{\boldsymbol{e}\}_N)\Big)\right) \prod_{i}^{N} d\boldsymbol{R}_i d\boldsymbol{P}_i d\boldsymbol{e}_i. \tag{2.40}$$

where $\boldsymbol{e}_i$ is a unit vector of the local magnetic moment associated with ith atom. $F_0(\{\boldsymbol{R}\}_N, \{\boldsymbol{e}\}_N)$ is the effective potential energy at fixed $\{\boldsymbol{R}\}_N$ and $\{\boldsymbol{e}\}_N$ that can be tacked by finite-temperature constrained spin-polarized density functional theory (Ma and Dudarev, 2015). It means we need to extend the theory in Sec. 2.4.1 to include the electronic entropy and replace $E_0[n(\boldsymbol{r}), \boldsymbol{m}(\boldsymbol{r})]$ with $F_0[n(\boldsymbol{r}), \boldsymbol{m}(\boldsymbol{r})]$. In addition, the band occupancy needs to be chosen based on Eq. 2.32. Band

structure calculations suggest the magnetization density in Fe is well localized and each iron atom could be associated with a local magnetic moment that behaves in a Heisenberg-like manner (Abrikosov et al., 2016). Therefore, the rigid spin approximation might be reasonable at least for iron. However, we cannot apply this method to Ni since it does not develop a well localized magnetic moment and the longitudinal fluctuation plays a dominant role (Abrikosov et al., 2016).

Both experimental (Waseda and Suzuki, 1970) and theoretical studies (Lichtenstein et al., 2001) have suggested the liquid Fe is in the paramagnetic state with a non-vanishing local magnetic moment. Although we may use the method described above to study the effect of spin dynamics, it is too expensive to do so. We need to further simplify the problem into a manageable size. For this, we re-consider the argument of dynamic timescales. Abrikosov et al. (2016) suggest the spin de-coherence time is 10^{-14}- 10^{-15} s which is very close to the characteristic timescale of electrons (10^{-15} s). Therefore, we may apply the adiabatic approximation to the orientation of the local magnetic moment as well and re-write Eq. 2.40 as,

$$\mathcal{Z} = \frac{1}{N!h^{3N}} \int \int \exp\left(-\beta\Big(\sum_{I=1}^{N} \frac{\boldsymbol{P}_I^2}{2M_I} + F_0(\{\boldsymbol{R}\}_N)\Big)\right) \prod_{i}^{N} d\boldsymbol{R}_i d\boldsymbol{P}_i. \tag{2.41}$$

where we have integrated out the magnetic degrees of freedom compared to Eq. 2.40, and $F_0(\{\boldsymbol{R}\}_N)$ is defined as,

$$F_0(\{\boldsymbol{R}\}_N) = -\frac{1}{\beta} \sum_{\{\boldsymbol{e}\}_m} \exp(-\beta F_l(\{\boldsymbol{e}\}_m, \{\boldsymbol{R}\}_N)) \tag{2.42}$$

And the force on the $\{\boldsymbol{R}\}_N$ is,

$$f = \sum_m p_m f_m(\{\boldsymbol{e}\}_m, \{\boldsymbol{R}\}_N), p_m = \frac{\exp[-F_0(\{\boldsymbol{e}\}_m, \{\boldsymbol{R}\}_N)]}{\sum_i^{\infty} \exp[-F_0(\{\boldsymbol{e}\}_i, \{\boldsymbol{R}\}_N)]}, \tag{2.43}$$

which can be calculated by the self-consistent KKR-CPA method (Pindor et al., 1983). This equation is equivalent to the disordered local momentum picture introduced by Gyorffy et al. (1985). However, the KKR-CPA method has difficulties to be integrated into the plane wave density functional theory code. Instead, Alling et al. (2010) develop the magnetic sampling method to obtain the force by averaging over a few magnetic configurations with randomly distributed spin-up and spin-down local magnetic moments,

$$f = \frac{\sum_{i=1}^{N_c} f_i(\{\boldsymbol{e}\}_i, \{\boldsymbol{R}\}_N)}{N_c}. \tag{2.44}$$

Although Eq. 2.44 differ slightly from Eq. 2.43, Alling et al. (2010) have shown for a large amount of magnetic configurations these two formula are equivalent. In

present work, we will employ the magnetic sampling method to study the effect of the paramagnetic state on the physical properties of liquid iron at high temperatures and also discuss the magnetic state on its critical point in Chapter 5.

2.4.3 Approximate paramagnetism by either non-magnetism or ferromagnetism?

One might wonder whether it is appropriate to approximate paramagnetism by non-magnetism or ferromagnetism as the application of Eq. 2.41 to study the paramagnetic phase is expensive. We can solve this problem from the perspective of the Helmholtz free energy of the electron-ion system (not just the electronic free energy!). If the magnetic fluctuation in the paramagnetic phase is substantial, an extra magnetic entropy would be induced. Then neither the non-magnetic state nor the ferromagnetic phase shares the same Helmholtz free energy as the paramagnetic phase.

Despite this, it is conventional and quite popular to model the paramagnetic state by the ferromagnetic state for iron-related materials. Then an empirical correction for the magnetic entropy is added to the free energy of the ferromagnetic state. The widely used term for the magnetic entropy is $k_{\mathrm{B}}\ln(m+1)$, where m is the average magnitude of the local magnetic moment. It is derived from the quantum mechanical entropy per magnetic atom ($k_{\mathrm{B}}\ln(2S+1)$), where for a given total spin angular momentum S its projection on the z-axis can take $2S+1$ values. As discussed by Khmelevskyi (2018), the generalization from the quantum spin space to the classic spin space is problematic. For a local magnetic moment with the magnitude of m, it can point to more than $m+1$ directions. Tsuchiya et al. (2006) used the term $k_{\mathrm{B}}\ln(n(2S+1))$ to calculate the paramagnetic entropy of magnesiowustite, where n is the electronic configuration degeneracy whose value is 3 for the high-spin phase and 1 for low-spin phase. It is unclear why the electronic configuration degeneracy enters the magnetic entropy term. To show this, in the high-spin magnesiowustite, there are six electrons for Fe^{2+}; two of them occupy the two e_g orbitals and three of them the three t_{2g} orbitals. The remaining electron would occupy one of the three t_{2g} orbitals. We denote the occupancy as p_1, p_2, p_3, where the sum of $p_1+p_2+p_3$ is one. In each case, the quantum magnetic entropy is still $k_{\mathrm{B}}\ln(2S+1)$. Therefore, the total quantum magnetic entropy is

$$\begin{aligned} S_{\mathrm{total}} &= p_1 \times k_{\mathrm{B}}\ln(2S+1) + p_2 \times k_{\mathrm{B}}\ln(2S+1) + p_3 \times k_{\mathrm{B}}\ln(2S+1) \\ &= (p_1+p_2+p_3) \times k_{\mathrm{B}}\ln(2S+1) \\ &= k_{\mathrm{B}}\ln(2S+1). \end{aligned} \tag{2.45}$$

Although one electron can occupy one of the three t_{2g} orbitals in the high-spin state of magnesiowustite, the total quantum magnetic entropy is $k_{\mathrm{B}}\ln(2S+1)$. Considering the great uncertainty in the magnetic entropy, we should avoid estimating the free energy of the paramagnetic phase by giving an empirical correction to the free energy of the ferromagnetic phase.

Chapter 3

Partial core vaporization during giant impacts

Contents

3.1 Introduction

Once differentiated, the core of planets and planetesimals is dominated by liquid or solid iron, alloyed with nickel and various lighter elements (Hirose et al., 2013). Because of its obvious geophysical significance, considerable effort was put to determine both theoretically and experimentally the phase diagram of iron (Alfe et al., 1999; Campbell, 2016; Caracas, 2016; Tateno et al., 2010) up to Earth's inner core conditions (around 360 GPa and 6000 K) and beyond. Recently, a complete set of equations of state (EOS) was proposed, covering 7 - 30 g/cm^3 densities and 10,000 – 1,000,000 K temperatures (Sjostrom and Crockett, 2018).

Much less is known about the thermodynamic and thermophysical properties of iron below 1 GPa and above its melting point (around 1850 K). Hixson et al. (1990) have measured the liquid iron density at 0.2 GPa up to 4000 K. Grosse and Kirshenbaum (1963) measured the liquid-vapor equilibrium density up to the boiling point at 1 bar and 3160 K. In order to obtain the critical point, a large extrapolation must be made. The first method is to employ empirical equations of state with several adjustable parameters, which can be determined from available experimental data (Fortov and Lomonosov, 2010; Medvedev, 2014); the second one is to use the law of rectilinear diameter (Grosse and Kirshenbaum, 1963). However, it is unclear whether these extrapolations work at high temperature where no experimental data are available.

Indeed, the regime of low densities and high temperatures, still not yet well characterized, is typical for the after-shock state of proto-planetary cores occurring in the aftermath of catastrophic events such as giant impacts. The Earth's Moon formed after such a giant impact between the proto-Earth and Theia, an astronomical body whose most commonly accepted size is that of Mars (Asphaug, 2014; Canup, 2004b). Hydrodynamic impact simulations show that it results in the formation of a disk (Canup, 2012; Canup and Righter, 2000; Ćuk and Stewart, 2012) or a synestia (Lock et al., 2018). The disk might be iron-depleted, producing a small Moon's core. However, results of these simulations heavily rely on available EOS. An experimental result on iron found the shock pressure required for vaporization when compressed from ambient conditions and then decompressed to 1 bar to be around 507 (+65, -85) GPa (Kraus et al., 2015), lower than previous estimates of 887 GPa (Pierazzo et al., 1997). This implies that the cores of a large number of the planetesimals from the late stage of accretion largely vaporized during the impacts (Kraus et al., 2015).

In order to assess whether the core of the planets undergoes significant vaporization during a giant impact, we employ *ab initio* molecular-dynamics simulations to explore iron over a wide density region encompassing the critical point (CP) and the Hugoniot lines of the shocked cores. In addition, we characterize the structural and transport properties of iron including diffusion coefficients, viscosity and thermal conductivity in the low-density region, which may provide a better constraint on

the behavior of iron in the proto-lunar disk.

3.2 Simulation details

3.2.1 *Ab initio* molecular dynamics

Ab initio molecular dynamics simulations were performed by VASP code (Kresse and Furthmüller, 1996; Kresse and Furthmüller, 1996). We used the NVT ensemble, where $N = 108$ atoms, V is the volume of simulated system, and the temperature T is maintained by the Nosé thermostat (Nosé, 1984). A Verlet algorithm is used to integrate the Newton's equation of motion with a timestep of 1 fs. The total simulation time at each temperature and density condition is at least 10 ps. The interatomic forces were calculated by employing the projector augmented wave (PAW) method (Blöchl, 1994; Kresse and Joubert, 1999) within the framework of finite-temperature density functional theory (Hohenberg and Kohn, 1964; Kohn and Sham, 1965; Mermin, 1965). The PBE formalism (Perdew et al., 1996) for the exchange correlation term and the valence electron configurations ($3d^7 4s^1$) for the pseudopotential were used. The partial occupancy for the electronic calculation were calculated using a Fermi smearing scheme with a width at simulated temperature. The energy cut-off for the plane-wave basis set was set to 550 eV. The break condition for the electronic self-consistent loop was 10^{-4} eV. The number of electronic bands was adapted to the temperature conditions such as to cover the entire spectrum of the fully and partially occupied states and to include enough non-occupied bands. The convergence of the pressure tensor and the energy are on the order of a few percent when compared to a grid of $4 \times 4 \times 4$ k-points generated by Monkhorst-Pack scheme (Monkhorst and Pack, 1976) and a kinetic energy cut-off of 850 eV.

It should be noted that both experiments (Waseda and Suzuki, 1970) and theoretical simulations (Lichtenstein et al., 2001) suggest that liquid iron might be in a paramagnetic state. As discussed by Marqués et al. (2015), spin-polarized MD simulations yield an inherent long-range ferromagnetic order. In order to avoid such residual magnetic state, we decided to perform non-spin-polarized simulations to approximate the paramagnetic state of liquid iron at low pressure and high temperature. This is the mean field approximation of the paramagnetic state, even if it neglects the spin fluctuations whose effects will be discussed in Chapter 5.

3.2.2 Construction of the spinodal line

During the simulations at low temperatures, with decreasing density, the pressure reaches a local minimum. This marks the liquid spinodal point: the minimal density at which the liquid is stable. At densities lower than the spinodal, the liquid is unstable and cavitation occurs (Speedy, 1982). Under further expansion, the pressure starts to increase and the local maximum marks the gas spinodal: the maximum density at which the gas is metastable. Between the gas and liquid spinodal den-

sities, neither gas nor liquid can exist as a single phase, but rather they co-exist. This is similar to the van der Waals model. In order to fit the pressure-density curves we employ a simple third-order polynomial function. This method has been successfully used by other theoretical studies on super-cooled silicon (Vasisht et al., 2011). Spinodal lines with negative pressure have been reported in experiments (Green et al., 1990), classic MD simulations on the metastable extension of liquid water (Poole et al., 1992), and first-principles MD on the metastable extension of liquid silicon (Zhao et al., 2016).

3.2.3 Structural analysis

The short-range order in the fluid is revealed by the pair distribution function ($g_{Fe-Fe}(r)$),

$$g_{Fe-Fe}(r) = \frac{V}{N(N-1)} \langle \sum_i \sum_{j \neq i} \delta(r - r_{ij}) \rangle \tag{3.1}$$

where r is the correlation length, r_{ij} is the distance between atoms i and j, N is the total number of iron atoms in the simulations, V is the total volume of the system, and $\langle\rangle$ is the ensemble average.

3.2.4 The mean-square displacements

The mean-square displacements (MSD) are defined as,

$$MSD(\tau) = \langle [r_i(t_0 + \tau) - r_i(t_0)]^2 \rangle \tag{3.2}$$

where the values are averaged over the total number of atoms and time origins (t_0) and τ represents a sliding time window spanning a portion of the trajectory. The asymptotic slope of the mean square displacement with respect to time yields the diffusion coefficient D in the long-time limit,

$$D = \frac{1}{6} \lim_{\tau \to \infty} \frac{MSD(\tau)}{\tau}. \tag{3.3}$$

3.2.5 Velocity autocorrelation function

We calculate the normalized velocity autocorrelation function as,

$$\Phi(\tau) = \frac{\langle v(0)v(\tau) \rangle}{\langle v(0)v(0) \rangle}, \tag{3.4}$$

where $v(t)$ is the velocity of a particle at time t. The self-diffusion coefficient D is given by the time integral of the velocity autocorrelation function by,

$$D = \lim_{t \to \infty} \frac{1}{3} \int_0^t d\tau \langle v(0)v(\tau) \rangle \tag{3.5}$$

3.2.6 Entropy calculations

The Fourier-transform of the velocity auto-correlation function yields the total movement of the atoms in the fluid defined as,

$$F(\nu) = \int_0^\infty \Phi(\tau) \cos 2\pi\nu\tau d\tau \tag{3.6}$$

The entropy can then be obtained by integrating over the vibrational part of this spectrum, in the same way as we do for solids. However, Eq. 3.6 captures not only the agitation of the atoms but also their diffusion. The latter is zero in solids, which allows us to directly obtain the entropy; but for fluids by definition it is finite and positive, and thus must be removed from the spectrum of Eq. 3.6. For this we employ the two-phase thermodynamic method (Lin et al., 2003) to decompose the total spectrum of Eq. 3.6 into a diffusive, gas-like part and a purely vibrational solid-like part,

$$F(\nu) = (1 - f_g)F_s(\nu) + f_g F_s(\nu) \tag{3.7}$$

where f_g is the gas-like fraction. The entropy stemming from the gas-like and the solid-like parts is obtained using the hard sphere model and the harmonic oscillator model respectively. This method gives a reasonable estimation of entropy for pure liquid metals (Desjarlais, 2013). We verify again our implementation and use the same parameters as Desjarlais (2013) and conduct simulations at 0 GPa and 1800 K for liquid iron. We obtain a value for the entropy of 11.05 k_B/atom, compared to 12.00 k_B/atom in Desjarlais (2013) . The discrepancy comes from the magnetic entropy, which is estimated to be about 1 k_B/atom (Desjarlais, 2013) and which we did not include in our calculation.

3.2.7 Viscosity

The viscosity is given by the famous Green-Kubo formula,

$$\eta = \frac{V}{k_B T} \int_0^\infty \langle P_{\alpha\beta}(t) P_{\alpha\beta}(0) \rangle dt \tag{3.8}$$

where V is the total volume, k_B is the Boltzmann constant, T is the temperature, $P_{\alpha\beta}$ stands for the off-diagonal element of the stress tensor and t denotes the correlation time.

3.2.8 Electrical and thermal conductivity

The electrical and thermal conductivity were calculated based on 20 configurations, equally spaced by 500 fs using the Kubo-Greenwood formalism (Greenwood, 1958; Kubo, 1957). This was successfully applied to the Earth's outer core (Pozzo et al., 2012). The Brillouin zone was sampled with the Baldereschi point (Baldereschi, 1973). A test with a k-points mesh of $4 \times 4 \times 4$yields results within 1 % difference to using only the Baldereschi point.

We calculate the dynamic Onsager coefficients using the Kubo-Greenwood formula (Pozzo et al., 2012),

$$L_{lm}(\omega) = (-1)^{l+m} \frac{2\pi e^2 \hbar^2}{3m_e^2 \omega V} \sum_{\mathbf{k}} \sum_{i,j=1}^{n} \sum_{\alpha=1}^{3} w(\mathbf{k})[f(\varepsilon_{i,\mathbf{k}}) - f(\varepsilon_{j,\mathbf{k}})] \times |\langle \Psi_{j,\mathbf{k}} | \Delta_\alpha | \Psi_{i,\mathbf{k}} \rangle|^2 [\varepsilon_{j,\mathbf{k}} - \mu]^{l-1} [\varepsilon_{i,\mathbf{k}} - \mu]^{m-1} \delta(\varepsilon_{j,\mathbf{k}} - \varepsilon_{i,\mathbf{k}} - \hbar\omega) \quad (3.9)$$

where e and m_e are the electron charge and mass respectively, $\hbar$ is the reduced Plank's constant, V is the cell volume and n is the number of bands used in the simulations, α sum runs over the three spatial directions, $\Psi_{i,\mathbf{k}}$ and $\varepsilon_{i,\mathbf{k}}$ are the Kohn-Sham wavefunctions and associated eigenvalues at the corresponding **k**-point, $f(\varepsilon_{i,\mathbf{k}})$ is the Fermi factor. The δ function is represented by a Gaussian with width equal to the average spacing between the eigenvalues. $w(\mathbf{k})$ is the weight of the particular **k**-point in the Brillouin zone.

The electrical ($\sigma(\omega)$) and thermal ($k(\omega)$) conductivity are obtained as,

$$\sigma(\omega) = L_{11}(\omega), \quad (3.10)$$

and

$$k(\omega) = \frac{1}{e^2 T}(L_{22}(\omega) - \frac{L_{12}(\omega)L_{21}(\omega)}{L_1 1\omega}). \quad (3.11)$$

The σ_0 and k_0 are the respective values of $\sigma(\omega)$ and $k(\omega)$ in the limit $\omega \to 0$. In order to verify our implementation, we conducted simulations at 328 GPa and 6350 K for liquid iron using exactly the same parameters as Pozzo et al. (2013). At these conditions, the density of liquid iron is 12.95 g/cm^3. We obtain an agreement better than 1 % for both types of conductivity, when compared to the values reported in Pozzo et al. (2013).

3.3 Results and discussion

3.3.1 The critical point

We perform first-principles molecular dynamics simulations in the 3000-15000 K temperature range and densities below 8 g/cm^3. This regime is characteristic of the aftermath conditions of giant impacts (Canup, 2004a). We compute the pressure dependence of the density along several isotherms (Fig. 3.1). We use a third-order polynomial expansion of the pressure as a function of density to identify the liquid spinodal and the position of the critical point, as detailed in the methodology. For iron, we identify a liquid spinodal point for all isotherms up to 9000 K. Along this latter isotherm the minimum pressure corresponding to the liquid spinodal is obtained at 2.40 g/cm^3. At 9000 K, we extend the simulations towards even lower densities, which allows us to observe also a maximum along the pressure-density curve. This corresponds to the gas spinodal, lying at 1.85 g/cm^3. Starting with the

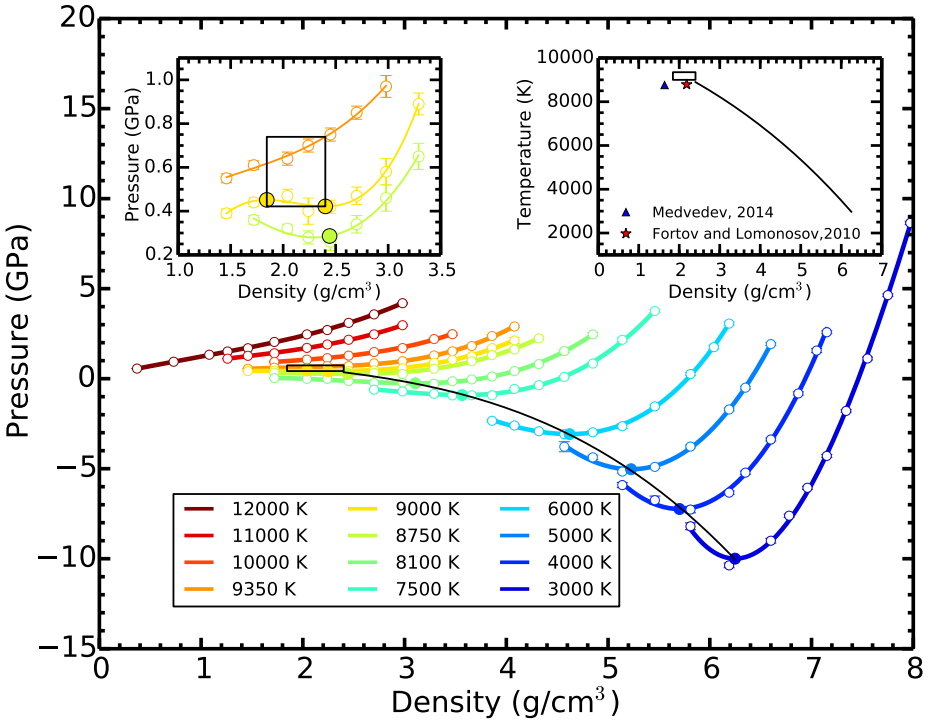

Figure 3.1: Variation of pressure as a function of density for iron along several isotherms. Along a given isotherm below the critical temperature, with volume expansion, the pressure may decrease to reach negative values. These negative pressures indicate the presence of hydrostatic tension in the system. According to the classic nucleation theory (Karthika et al., 2016), the first-order transitions need to overcome energy barriers due to the surface energy, which prevents the formation of the thermodynamic stable phase. Therefore, this stage is thermodynamically metastable but mechanically stable. The minimum of the pressure marks the liquid spinodal (solid symbols). Joining the spinodal points yield the spinodal line (the black solid line). At densities lower than that of the liquid spinodal the pressure starts to increase until it reaches a maximum, which marks the gas spinodal, as shown in the left inset figure. At densities between the two spinodal lines a two-phase mixture coexists. Because of technical computing limitations we compute the gas spinodal only at temperatures close to the critical one, that is 9000 K. Above the critical temperature (9350 K) the pressure decreases continuously with decreasing density, but does not show any minima or maxima. We obtain the critical point to be in the range 1.85-2.40 g/cm^3 and 9000-9350 K (black empty rectangle). The right inset shows comparisons of the critical point, between our estimate and the ones inferred from experiments (Fortov and Lomonosov, 2010; Medvedev, 2014).

9350 K isotherm the pressure varies monotonically without any local minimum or maximum; this is characteristic of the supercritical state. Therefore, the position of the CP is bracketed by the two spinodal lines, which intersect in the CP itself, and by the last isotherm with minima and maxima and the first isotherm with monotonical pressure variation. For iron, using the results of our simulations we predict that the CP lies in the 1.85-2.40 g/cm^3, and 9000-9350 K range (Fig. 3.1). These values correspond to pressure of 4-7 kbars.

3.3.2 Static structure

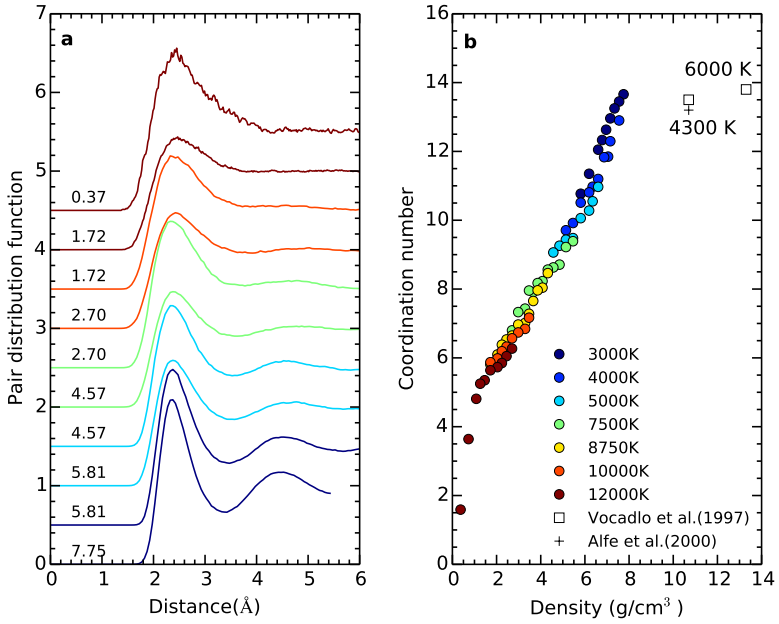

Figure 3.2: The static structure of hot fluid iron. (a) Pair distribution function for iron at selected temperatures and densities. The color of solid lines represents different temperatures, as shown in the legend of (b). The unit of those numbers is g/cm^3. (b) The coordination number calculated by counting the number of atoms within the first minimum of $g(r)$ from a central atom. There is a weak dependence of the coordination number with the temperature. However, its density dependence is very strong below 7.75 g/cm^3, then saturate at a value of 13 up to 6000 K and 13.3 g/cm^3 (Alfè et al., 2000; Vočadlo et al., 1997), which is the condition at Earth's inner-outer core boundary.

Several typical pair distribution functions (PDF) calculated from the MD simulations are shown in Fig. 3.2(a). As the periodic boundary condition is used, the maximum correlation length is limited to half of the cell length. All PDFs start at zero, and continue as such up to a certain distance that defines the exclusion radius. This is caused by the strong repulsive force between any two atoms that prevents atoms from staying too close to each other. In the iron simulations, the exclusion radius depends weakly on the density and temperature; it decreases from 1.9 Å at

3000 K and 7.75 g/cm^3 to 1.8 Å at 12000 K and 0.37 g/cm^3 indicating a decline of repulsive force over this temperature and density regime.

The first peak in PDF, usually considered as a good approximation for the average bond distance in the fluid, occurs at 2.5 Å, with a height of 2.0 at 3000 K and 7.75 g/cm^3. These values remain relatively constant over a large range of temperature and density conditions, but the peak broadens with an increasing of temperature due to thermal activation. Previous *ab initio* molecular dynamics simulations at 1850 K and around 6.95 g/cm^3 also reported the main peak position of the PDFs at around 2.5 Å (Marqués et al., 2015).

The first minimum of the PDF marks the end of the first coordination sphere. At 3000 K and 7.75 g/cm^3, this lies at 3.3 Å and remains relatively constant over a large range of temperature and density conditions. We observe a second peak (the second coordination shell) at 4.5 Å, which again broadens with an increasing of temperature. Above 7500 K and below 2.70 g/cm^3, the positions of the first minimum and of the second peak become less obvious. And at 12000 K and 0.37 g/cm^3, the PDF decays steadily to a value close to one without an apparent minimum point. Due to the small cell size used here, we could not observe the long-distance behaviour in PDF beyond 6 Å.

The integral of the PDF up to the first minimum gives the coordination numbers (CNs). The Fe-Fe coordination as a function of density and temperature has been shown in Fig. 3.2(b). We observe a weak dependence of the coordination number with temperature. For example, at a density of about 6 g/cm^3, the coordination number decreases from about 11 at 3000 K down to about 9.5 at 7500 K, and by extrapolation down to about 8 at 12000 K. However, density has a more pronounced effect on the changes in coordination number. Along the 3000 K isotherm the coordination number increases from about 9.5 at about 6 g/cm^3 up to 13.5 at 8 g/cm^3. At 3000 K and 7.75 g/cm^3 (about 5 GPa in pressure) the coordination is around 13.6, indicating a very close-packed liquid. Actually the value of 14 seems to be a saturation value for coordination in liquid iron at high pressures and densities, i.e. at 6000 K and 13.3 g/cm^3, the conditions at inner-outer core boundary inside the Earth, as was shown in other previous *ab initio* MD studies (Alfè et al., 2000; Vočadlo et al., 1997). The change in slope around 7.75 g/cm^3 implies that probably the compression mechanism above this density is likely to be caused by the change in the second coordination shell. With decreasing density along the same isotherm, the Fe-Fe coordination decreases to around 10.8 at a density of 5.81 g/cm^3. In the supercritical region, at 12000 K, the Fe-Fe coordination drops from 6.3 at 2.7 g/cm^3 density to 1.6 at 0.37 g/cm^3. A change in slope of the density-coordination dependence occurs around 1.46 g/cm^3 along 12000 K. At the critical point, the Fe-Fe coordination number is around 6.

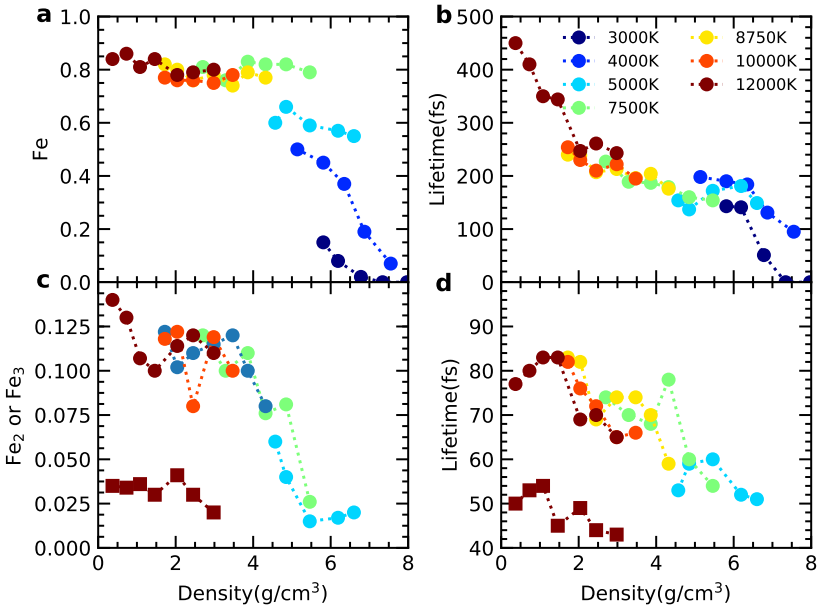

Figure 3.3: Speciation of isolated clusters of hot fluid iron at low densities and high temperatures, representing a good approximant to the structure of the gaseous iron. In (a) and (b), the relative abundance and the average lifetimes of isolated iron atom are displayed. In (c) and (d), we have shown the abundance and lifetimes of iron dimer (Fe_2) represented by the circles, and iron trimer (Fe_3) in squares. Other clusters are not shown as their abundance are below 0.005. In the supercritical regime (10000 K and 12000 K), the iron fluid is dominated by long-lived monoatomic and diatomic clusters; at low temperatures we retrieve more familiar polymerized melts.

3.3.3 Speciation

The coordination number as obtained from PDF only gives an average information on the number of atoms that surrounds a central iron atom. The distribution of the bond lengths and the lifetimes of atomic clusters are still missing. Consequently, we also use a geometric criterion to analyse the interatomic connectivity at every configuration generated during our simulations. The geometric cut-off length for two atoms to be considered connected, i.e. bonded, is chosen to be the radius of the first coordination sphere that is the first minimum of PDF. Then the size of any given iron coordination polyhedron is defined as the number of atoms within the range of the first minimum of PDF. Once the individual atoms forming a given coordination polyhedron are identified, we monitor the time they obey the geometrical criterion for bonding to define the polyhedron lifetime.

Fig. 3.3(a) shows the coordination of atoms at different conditions. In general, we observe, as expected, a depolymerization of the fluid with decreasing temperature. At 3000 K, from 7.97 g/cm^3 to 6.78 g/cm^3, the iron is highly polymerized with few

or no isolated Fe atoms. With further decrease of density, we observe the presence of isolated Fe atoms with an increasing abundance from 0.02 at 6.78 g/cm^3 to 0.15 at 5.81 g/cm^3 indicating a gradual depolymerization. Along the 4000 K isotherm, the abundance of isolated iron atoms increases rapidly from 0.07 at 6.78 g/cm^3 to 0.50 at 5.14 g/cm^3. Above 7500 K and below 5.46 g/cm^3, we observe a nearly constant concentration of 0.85 of isolated iron atoms, irrespective of the temperature. The lifetime of isolated Fe atoms is shown in Fig. 3.3(b); in general, the increase of temperature and the decrease of density result in rising their lifetime. In the supercritical regime, at 12000 K, the lifetime of isolated atoms increases linearly with decreasing the density. At the lowest density of 0.37 g/cm^3 calculated in the present study, the lifetime is around 450 femtoseconds. We also observed some small Fe_2 dimers starting to appear from 5000 K and 6.60 g/cm^3, as illustrated in Fig. 3.3(c). There is a weak temperature dependence of the Fe_2 abundance, with a major role played by the density. The abundance of Fe_2 clusters increases considerably in the 5.46 to 4.32 g/cm^3 density range. Below 5.46 g/cm^3 density, the abundance of Fe_2 fluctuates around 0.11 until 1.08 g/cm^3, then increases again to 0.14 at further decreasing density to 0.37 g/cm^3. We only find a small amount of iron trimers (Fe_3) at 12000 K. The lifetime of Fe_2 and Fe_3 clusters (Fig. 3.3(d)) is below 100 femtoseconds, shorter than that of Fe. Our results suggest the critical iron fluid is mainly atomic with the Fe dimers being the next most abundant species.

3.3.4 Velocity autocorrelation function

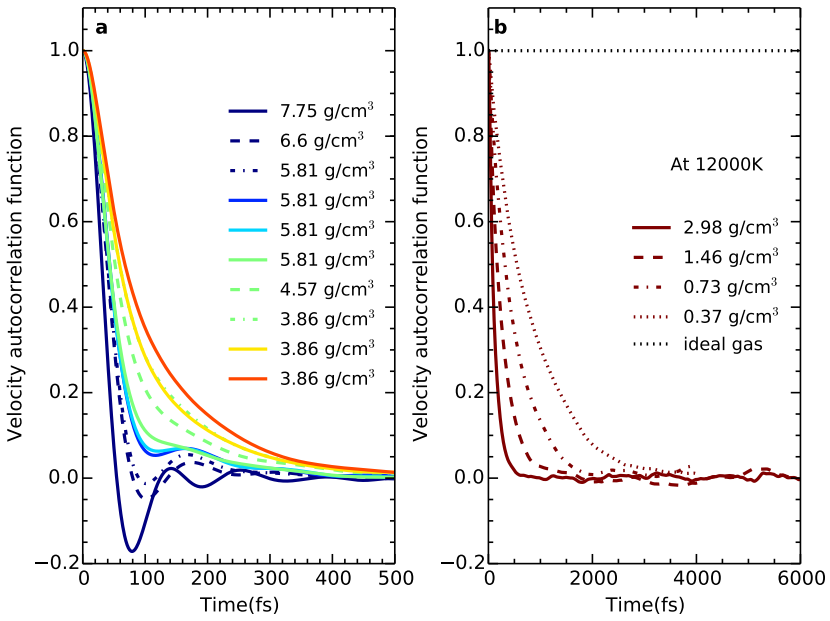

Figure 3.4: (a) The overall trend of velocity autocorrelation function from 3000 K and 7.75 g/cm^3 to 10000 K and 3.86 g/cm^3. (b) Velocity autocorrelation function along the supercritical isotherm 12000 K as a function of density.

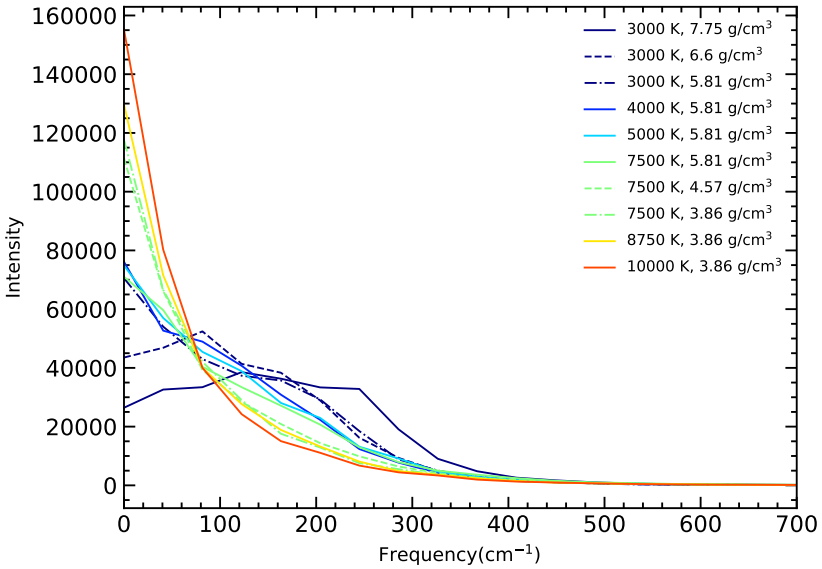

Figure 3.5: Vibrational spectrum of fluid iron calculated by Fourier transform of the velocity autocorrelation function shown in Fig. 3.4(a). At 3000 K and 7.75 g/cm^3, we observe a broad peak from 0-400 cm^{-1}, which is caused by breathing-types vibrations of the first coordination shell.

As a time-dependent correlation function, the velocity autocorrelation function (VAF) not only reveals the underlying dynamical processes like diffusional and vibrational motions operating in an atomic or molecular system at a microscopic scale, but also shows a direct connection with the macroscopic properties like the diffusion coefficient. These facts offer a good reason to study VAF, whose straightforward calculation details are provided in Section 3.2.5. We plot the overall trend from 3000 K and 7.75 g/cm^3 to 10000 K and 3.86 g/cm^3 in Fig. 3.4(a). At 7.65 g/cm^3 and 3000 K, VAF decays to reach a first minimum at a value of 80 fs. The formation of this first minimum is generally attributed to the cage effect formed by the nearest neighbors, which exert a restoring opposite force on the central atom when this encounters the cage during its vibration. There are two more minima at larger correlation times. Globally, the three observed minima represent different vibrational modes. With further decreasing density to 5.81 g/cm^3 at 3000 K, as the atoms become increasingly spaced, only two minima are found, and their positions are shifted to longer correlation times (i.e. low frequency) due to a decrease of the interaction strength (also see Fig. 3.5). With increasing temperature at fixed density of 5.81 g/cm^3, the minimum becomes less obvious and disappears at 7500 K where a single exponential decay is present, indicating the cage structure can no longer hold the Fe atoms due to the large thermal velocity at high temperature. The VAF decay is weakly dependent on temperature, but appears at relatively similar densities.

To illustrate the dependence of the VAF with the density, we show its variation along the 12000 K isotherm in Fig. 3.4(b). The decay of VAF becomes faster at

high densities since collisions occur more frequently due to the relatively short distances between atoms, which break correlations. The decay time of VAF at 12000 K and 0.37 g/cm^3 is around 2500 fs, suggesting that at these conditions, only 12 independent configurations are sampled during a 30 ps simulation. The situation would become even worse when the temperature and density are below 12000 K and 0.37 g/cm^3 since the correlation time increases with decreasing temperature and density. Reed and Flurchick (1994) found the statistical inefficiency, which represents the average time needed to sample two statistically uncorrelated configurations during an MD simulation, is almost linearly scaling with the inverse of density. For the low-density phase, an intrinsic problem is that there are two times scales: the inter-collision time and collision duration. As the collision duration is very short, the atoms move in space for a very long time before the next collision occurs. A common method to speed up the correlation time is to use a larger time step. But a very large time step would cause missing collisions and thus decreasing accuracy of sampling of the configurational space. Reed and Flurchick (1994) proposed a hybrid algorithm that combines the time-driven simulation with event-driven simulation, which is frequently used in the hard-sphere models. This may provide a promising solution to the time scale problems. However, many questions need to be answered before its practical implementations combined with density functional theory will become available, especially on how to define a collision radius.

3.3.5 Diffusion

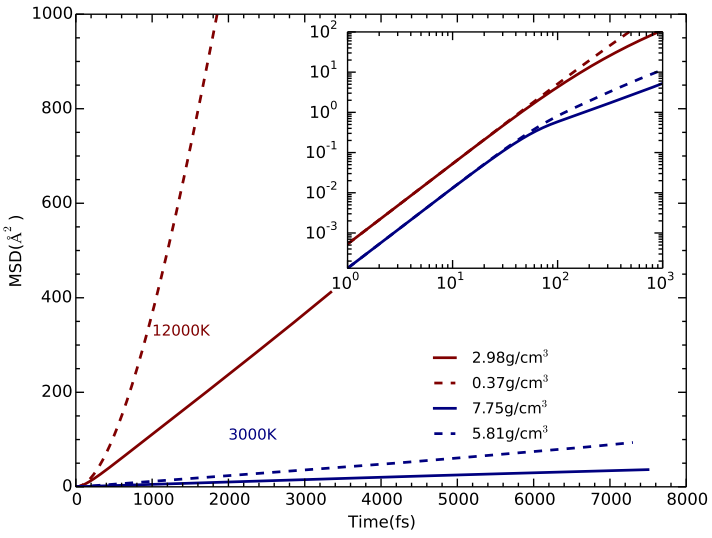

Figure 3.6: The mean-squared displacement (MSD) of fluid iron at selected densities and temperatures. The inset shows a log-log zoom-in plot for short times. The inset outlines a slope change that separates the two characteristic regions of the diffusion: ballistic, for times less than about 100 fs, and diffusive, at higher times.

The mean square displacements (MSD) measure the average distance that atoms move during a reference time window. We show in Fig. 3.6 four examples that cover the whole studied temperature range from 3000 to 12000 K and density range from 7.75 to 0.37 g/cm^3. The total diffusion process can be divided into two stages, as seen by the change of slope in the log-log plot in the inset of Fig. 3.6. The first part, on the order of about 100 fs, is the ballistic part dominated by the free particle motion before collision. The second part is dominated by the diffusion of the particles; in this region the square displacement linearly scales as the function of time, where the slope of the MSD yields the diffusion coefficient.

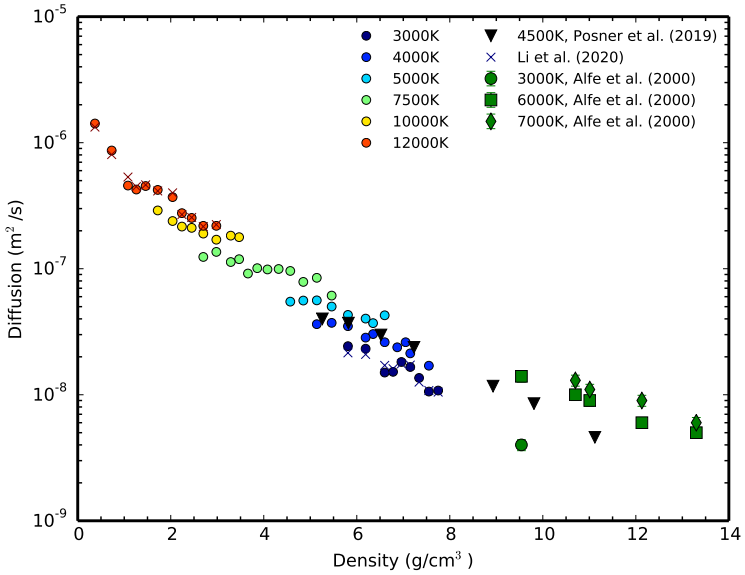

Figure 3.7: The temperature and density dependence of the self-diffusion coefficients of fluid iron. The solid circles and black crosses represent diffusivities determined from velocity autocorrelation function and mean-squared displacement, respectively. The green squares and black triangles denote several self-diffusion coefficients of liquid iron at high densities and temperatures previously reported in the literature (Alfè et al., 2000; Posner et al., 2017).

We also calculate the diffusion coefficient by integrating the velocity autocorrelation function, as shown in Fig. 3.7. The diffusivity increases by two orders of magnitude from about 1.0×10^{-8} m^{2}s^{-1} at 7.75 g/cm^3 and 3000 K to about 1.3×10^{-6} m^{2}s^{-1} at 0.37 g/cm^3 and 12000 K. At high densities and low temperatures, the diffusion coefficients correspond to distances travelled by the iron atoms on the order of about 2.5 cm in 24 hours, which would ensure highly efficient chemical equilibration close to the surface of the iron droplets. At low densities and high temperatures, the diffusion coefficients correspond to displacements on the order of 0.5 m in 24 hours, which would contribute significantly to the chemical equilibration inside large-scale fluid

volumes. As expected, the increasing temperature and decreasing density would increase the diffusivity. There is an excellent agreement between the values of the diffusion coefficients obtained using the two methods (the slope of the MSD and the integration of the VAF). Our values also compare well with previous theoretical studies in liquid iron (Alfè et al., 2000; Posner et al., 2017), at higher pressures and lower temperatures.

3.3.6 Viscosity

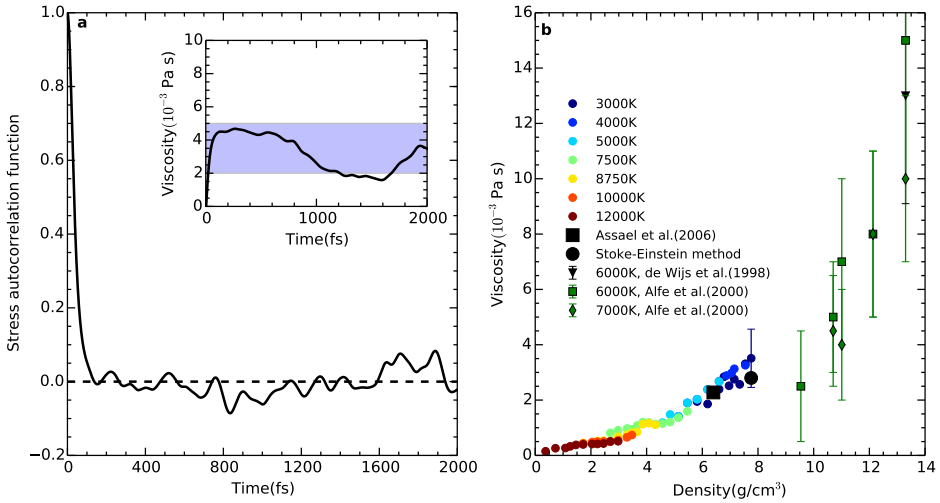

Figure 3.8: Viscosity of fluid iron varying as a function of temperature and density. (a) Stress autocorrelation function for fluid iron at 3000 K and 7.75 g/cm^3 calculated by averaging over three off-diagonal stress tensor and normalizing by dividing the value at time zero. The inset shows the integral of the average stress autocorrelation function as a function of time. The shaded areas denote the fluctuation of the viscosity. (b) The overall overview of viscosity of fluid iron as a function of temperature and density. The black square represents an experimental value at 2500 K and 6.40 g/cm^3 (Assael et al., 2006), which is close to our 3000 K isotherm. The black solid circles are the viscosity at 3000 K and 7.75 g/cm^3 determined from the Stoke-Einstein relation, which is in a fair agreement with the prediction by the Green-Kubo method.

The viscosity of iron was computed previously only in its high-density liquid state (Alfè et al., 2000; de Wijs et al., 1998) and applied to the dynamics of the liquid outer core of the Earth. We obtain the viscosity from the self-correlation of the shear components stress tensor. As a general rule this method requires much longer simulations times than are needed to obtain the other properties. We can improve the quality of the results by averaging over all the three shear components of the stress tensor. Fig. 3.8(a) displays the stress autocorrelation function (SAF) for fluid iron at 3000 K and 7.75 g/cm^3. After 0.15 ps, SAF decays to zero with a still large noise, about 5% compared with the value at t = 0. The inset in Fig. 3.8(a) shows the

viscosity integral as a function of time. After 0.4 ps, the shear viscosity fluctuates within the range 3.5×10^{-3}-5×10^{-3} Pa s.

We present the variation of viscosity as a function of density along several isotherms in Fig. 3.8(b). The values of viscosity at conditions typical to the outer parts of the protolunar disk, i.e. low density and high temperature, are in the range 0.5×10^{-3} to 4×10^{-3} Pa s. They show a decreasing trend with decreasing density, but due to the large scatter in values, we cannot identify any reliable trend with temperature. The values that we obtain for conditions specific to the protolunar disk are one order of magnitude smaller than in the Earth's outer core, estimated to be on the order of 2×10^{-3}-15×10^{-3} (Alfè et al., 2000; de Wijs et al., 1998). Assael et al. (2006) compiled viscosity data for liquid iron from 1850 K and 7.0 g/cm^3 to 2500 K and 6.40 g/cm^3. We find the viscosity at 3000 K and 6.40 g/cm^3 of 2.1×10^{-3} Pa s to be comparable to the corresponding value at 2500 K and 6.40 g/cm^3 of 2.276×10^{-3} Pa s (Assael et al., 2006).

At 3000 K and 7.75 g/cm^3 we perform a further check and compute the viscosity using the Stoke-Einstein relations, which connects diffusion coefficient to estimate the viscosity:

$$\eta = \frac{k_{\mathrm{B}} T}{2\pi a D}, \tag{3.12}$$

where η is the viscosity, k_{B} is the Boltzmann constant, T is temperature, D is the diffusion coefficient and a is the effective atomic diameter chosen to be the radius of the first peak in the radial distribution function from Fig. 3.2. This method has been used in previous work to determine the viscosity of liquid iron at Earth's core conditions (de Wijs et al., 1998). By applying this method, the estimate viscosity is 2.8×10^{-3} Pa s, where a fair agreement with Green-Kubo method is achieved.

3.3.7 Electrical and thermal conductivity

We used the Kubo-Greenwood formalism (Greenwood, 1958; Kubo, 1957) to determine the electrical and thermal conductivities. In this method, the electron-ion collisions are accurately described, while the electron-electron scattering and is neglected and its effect remains unclear (Dufty et al., 2018). All calculated electrical, thermal conductivity and the Lorentz constant of pure fluid iron as a function of density and temperature are shown in Fig. 3.9. Along 3000 K isotherm, the electrical conductivity decreases from 1.2×10^6 Ω^{-1} m^{-1} at 7.76 g/cm^3 to 0.8×10^6 Ω^{-1} m^{-1} at 5.81 g/cm^3, while the thermal conductivity declines from 80 Wm^{-1}K^{-1} to 40 Wm^{-1}K^{-1}. Along other isotherms, the electrical and thermal conductivity decrease monotonically upon a decreasing density as well.

At a density that is beyond 6.19 g/cm^3, the electrical conductivity decreases with temperature, as expected for a typical metal. The increasing temperature would generally enhance the electron-ion collisions causing a decrease of the relaxation

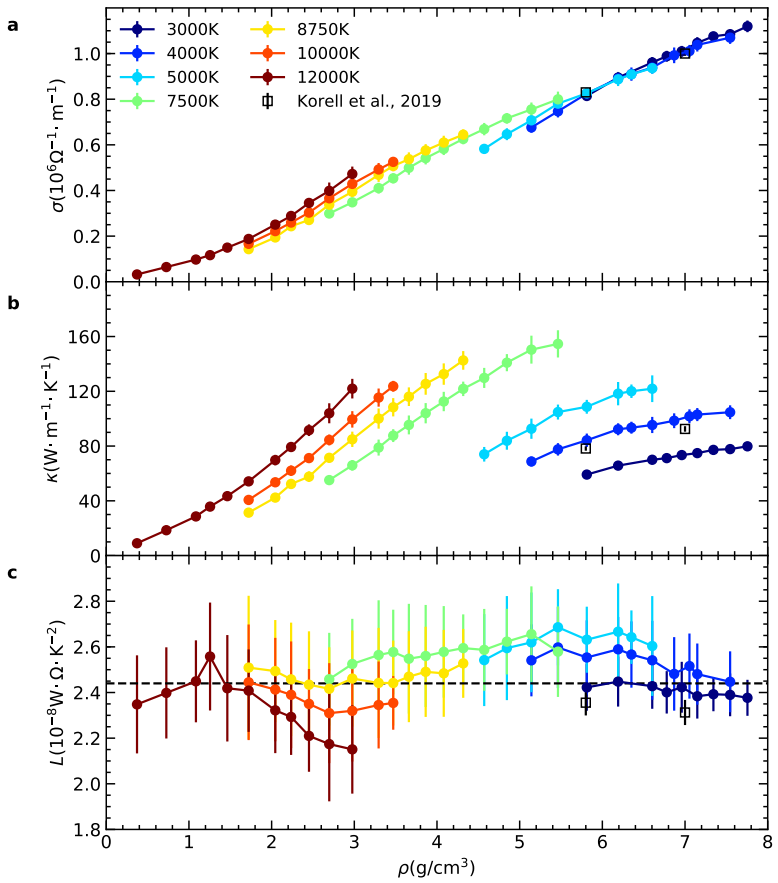

Figure 3.9: Electrical conductivity (a), thermal conductivity (b) and Lorentz number (c) of the fluid iron as a function of density and temperature. The Lorentz number is defined as $L = k/\sigma T$. The results from our work are represented as solid circles colored based on temperature. The theoretic results at around 3500 K and 6.22 g/cm^3 are from Korell et al. (2019) shown as black squares. The black dashed line in (c) represented the ideal Lorentz number of 2.44.

time and electrical conductivity. Below 6.19 g/cm^3, the trend of electrical conductivity as a function of temperature is reversed, where the electrical conductivity increases with temperature. It indicates the fluid iron at these conditions is more like a semiconductor, where the temperature dependence may be as a result of the increasing concentration of carriers due to thermal excitation. The observed change of temperature dependence around 6.19 g/cm^3 suggests a possible metal-non-metal transition and has also been observed in the other expanded metals like aluminium (Recoules et al., 2002).

Our calculated Lorentz number (Fig. 3.9(c)) almost keeps constant around 2.44 $\times$ 10^{-8} W Ω K^{-2} over the whole temperature and density range in this study. Compared with Korell et al. (2019), it is no surprise that a very good agreement is reached as the same method and DFT package are used.

3.3.8 Hugoniot lines

The behavior of materials under shock waves can be described using the Rankine-Hugoniot equations. These equations relate the density, pressure, and internal energy after shock to the initial state by,

$$E - E_0 = (P + P_0)(V_0 - V)/2 \tag{3.13}$$

where E, P, V are the internal energy, pressure and volume, respectively. And the 0 subscript denotes the initial state. The MD simulations that we performed at various isotherms contain all the information needed to build the Hugoniot EOS (see Fig. 3.10).

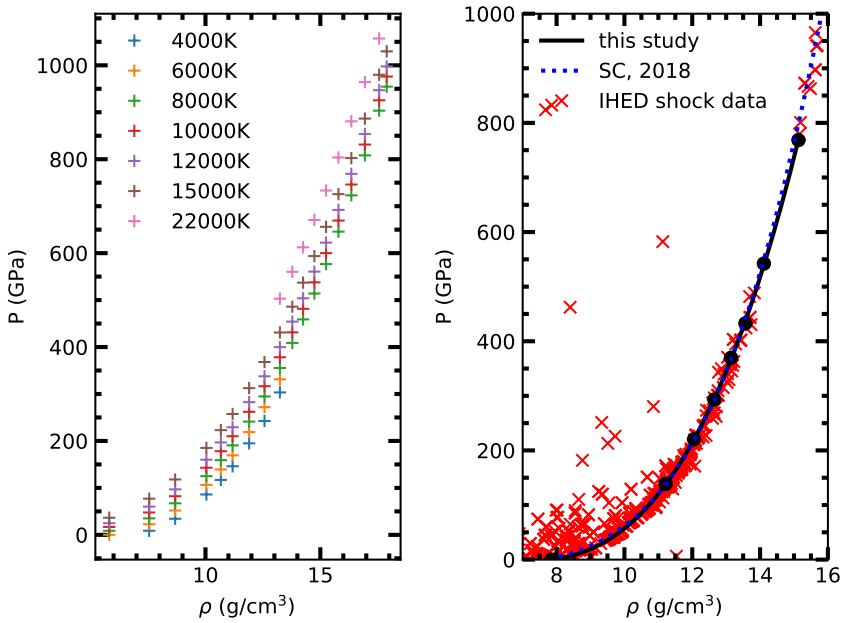

Figure 3.10: (a) Pressure as a function of density along several isotherms for liquid iron. (b) We have calculated the principal Hugoniot line with a initial condition of 300 K and 7.874 g/cm^3, which compares well with theoretical simulation results by Sjostrom and Crockett (2018) and shock experiments.

We consider two representative initial states. The first case has iron at 1 GPa and 1500 K, conditions similar to what we could expect to have in small planetesimals. For these conditions that we call warm Hugoniot the EOS intercepts the iron melting curve at 130 GPa. Previous shock experiments (Chen and Ahrens, 1997) on face-centered cubic iron with an initial condition of 1570 K and 1 bar show that the Hugoniot intercepts the iron melting curve at 80 GPa. In the second case we consider the initial state at 40 GPa and 4000 K, which may be representative for the state

of the core in Mars-sized impactors (Canup, 2004a). At these conditions iron is already molten. Fig. 3.11(a) shows the computed Hugoniot lines for these two cases. During shocks the temperature can easily reach thousands of degrees and the pressures hundreds of GPa. These would be typical conditions for the core state during giant impacts.

The actual amount of vaporization after an impact depends on entropy achieved. The entropy at the boiling point was estimated at 15.84 k_B/atom at 3100 K and 1 bar (Kraus et al., 2015). If the peak shock conditions during impact exceed this entropy value, then the onset of vaporization may take place and part of the shocked material can vaporize upon release and cooling (Ahrens and O'Keefe, 1972). We compute the entropy of the liquid iron along the two Hugoniot lines and at the spinodal points (Fig. 3.11) as a function of temperature from the vibrational spectra (see Section 3.2.6). For peak shock conditions at 15000 K, we estimate that entropy can reach 19.1 k_B/atom and 18.6 k_B/atom along the warm and the hot Hugoniot curves respectively. At these conditions the entropy is high enough to result in partial vaporization of the iron core. Our results show that above 7500 K, the entropy along the warm Hugoniot is less than along the hot Hugoniot. The entropy difference between these two Hugoniot lines is relatively small (0.5 k_B/atom) in the 7500 K to 15000 K range. If we relate entropy to the peak shock pressure, based on the computed entropy along the warm Hugoniot line, we find that the shock pressure required to reach the onset of vaporization upon release and cooling is 312 GPa. This is less than previous estimates of 390 GPa (Kraus et al., 2015). Along the hot Hugoniot, the onset vaporization pressure is 365 GPa. This is only slightly higher than that of warm Hugoniot.

3.3.9 Vaporization of small planetesimals

The onset of core vaporization can easily be reached in case of impacts of small planetesimals, like the ones that might have occurred either during the first stages of formation of the solar system, or during the late veneer. As a model example we consider a differentiated planetesimal with a mantle made of enstatite ($MgSiO_3$) and a core made of iron; we set the core-mantle boundary at 1 GPa and 1500 K (Raymond et al., 2009). We approximate the shock wave as a planar wave (Melosh, 2011) traveling through the two layers. However, this yields a simplified estimate of the peak pressure and does not thoroughly describe the pressure distributions in these bodies. When the impact occurs, shock waves travel through the silicate layers of the two bodies. At the core-mantle boundary, because of the density contrast between silicates and iron, the shock wave is partly reflected, going backward into the mantle, and partly transmitted, going forward into the core. Assuming a steady shock in a model $MgSiO_3$-based mantle(Militzer, 2013) and in the iron core, the impedance match method allows us to determine the properties of the reflected wave in the mantle and the transmitted wave in the core (Forbes, 2013). Fig. 3.12 illustrates the propagation of the shock wave according to this model through the

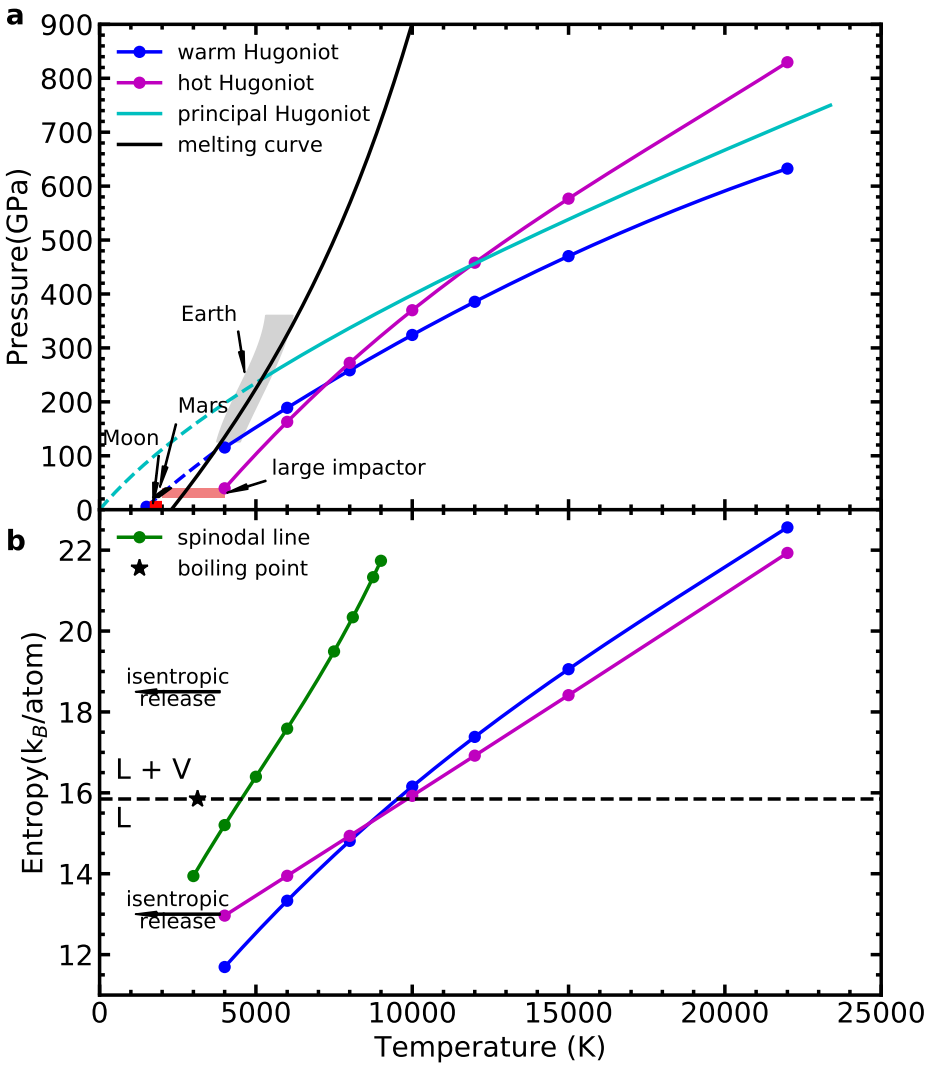

Figure 3.11: Computed Hugoniot lines for iron starting from two realistic initial states. (a) Temperature - pressure plots for various impact scenarios. The principal Hugoniot (Sjostrom and Crockett, 2018) that starts at ambient conditions and the melting curve of iron (Bouchet et al., 2013) are shown for reference only. For a smaller impactor like Moon, we approximate the initial state conditions as 1 GPa and 1500 K; for a large impactor like Mars, the initial state is set at 40 GPa and 4000 K. The Hugoniot lines cross because the gains in temperature and pressure is not linear with respect to changes in initial conditions. The shaded area represents estimated temperature gradients ranges in the metallic cores of the different objects involved in the impact (Antonangeli et al., 2015; Hirose et al., 2013; Stewart et al., 2007). (b) Computed entropy along the two Hugoniot lines. The star indicates the experimentally estimated entropy of boiling liquid iron at 3000 K, marked also by the dashed line.

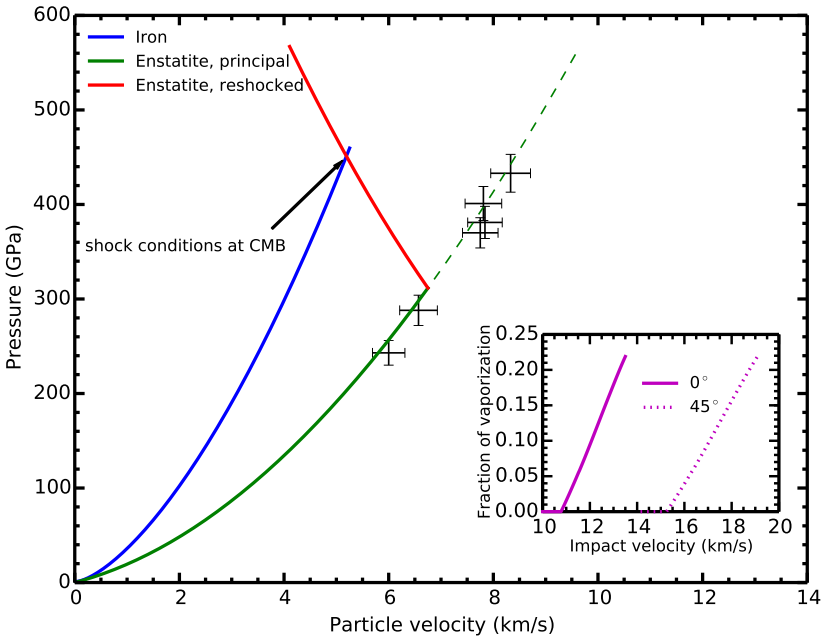

Figure 3.12: Graphical representation of the impedance match analysis for the core of the small impactor. The shock wave generated at the moment of the impact travels through the impactor's mantle assumed to be homogeneous. The shock state at the core-mantle is given by the $MgSiO_3$ principal Hugoniot line (green line) estimated based on previous *ab initio* simulations (Militzer, 2013). More recent experimental Hugoniot data points are represented by crosses (Fratanduono et al., 2018). At the core-mantle boundary the shock wave splits in two opposite waves. The one traveling forward enters the core. The final state in the core is given by the intersection between the re-shocked $MgSiO_3$ Hugoniot (red line) and the iron Hugoniot (blue line) with an initial state at 1 GPa and 1500 K (the warm Hugoniot in Fig. 3.11). The inset shows the fraction of iron that would vaporize from the corresponding impactor's core as a function of the impact velocity.

planetesimal.

As the shock proceeds through the mantle of the impactor this can lead to partial fragmentation. During this process the mantle fragments and can detach from the core leaving behind bare fragments of shocked core. In the post-shocked state, fragments of planetesimal core without mantle confinement can undergo an isentropic release into vacuum. In this case, if the entropy reached during the shock is high enough, the core may partly vaporize; otherwise it will remain liquid and accrete to the impacted body, or escape gravitationally and eventually crystallize.

For heads-on collisions of small planetesimals, the impact velocity required to onset vaporization is around 11.5 km/s. With an impact velocity around 13.5 km/s, peak pressure and temperature reach 450 GPa and 15000 K (Fig. 3.12). At these conditions about 22 % of iron would vaporize. In contrast, oblique impacts greatly reduce the peak pressure, due to a $\sin(\theta)$ factor where θ is the obliquity (Pierazzo and Melosh, 2000a). For the maximum frequency impact angles of 45° (Pierazzo and Melosh, 2000b), the velocity threshold to onset vaporization increases to 15.3 km/s. With mean impact velocities at 14.5 km/s and median impact angles at 40°, around 70% of the impacts of N-body simulations (Raymond et al., 2009) yield velocities larger than our threshold. This suggests that core vaporization is a common process during planetary formation. During the collision with the Earth's mantle, the core of the incoming planetesimal can be efficiently mixed into the molten silicate pond locally produced by the impact itself or into a pre-existing larger magma ocean. If such impacts happen after the Earth's core formation, this process would then increase the amount of highly siderophile elements that is seen today trapped and dispersed into the Earth's mantle.

3.3.10 Vaporization during giant impacts

In the case of giant impacts, the geometry effect plays an important role in controlling the shock peak conditions. As the validity of the impedance matching method is limited to the impacts where the lateral dimension of the impactor is small compared to the distance the shock wave has propagated (Melosh, 2011), it has only a limited applicability. However, the entropic and pressure criteria for vaporization still hold. For impacts with Mars-sized bodies, because of the hotter initial state of their cores, our simulations suggest a vaporization pressure of only 312 GPa. This is again smaller than previous estimations by Kraus et al. (2015) suggesting that even more iron will be vaporized than previously thought. However, the amount of iron that can be vaporized depends also on the local pressure conditions as the process of the impact itself takes its due course. As the predicted pressure thresholds for vaporization can be easily reached, a large amount of iron receives enough entropy to vaporize. The entropy threshold can even be easier exceeded due to the entropy gain after the first and secondary shocks and the conversion of gravitational potential energy to internal energy (Carter et al., 2020; Nakajima and Stevenson, 2015). Once again during this process the confinement of core fragments by the surrounding

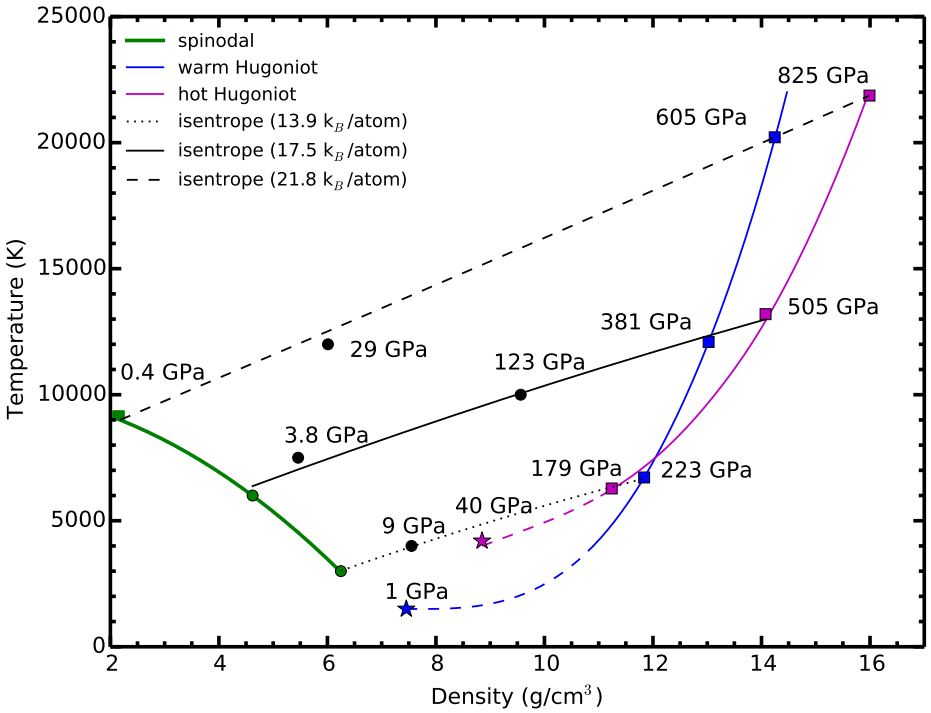

Figure 3.13: Isentropic release of the iron core starting from various peak conditions attained during large impacts. The shocked material gains entropy that is conserved during the release. If this entropy is larger than that of the boiling point then partial vaporization may occur. We compute the entropy along the spinodal and the Hugoniot lines at different temperatures, which allows us to map the entropy increase during various impact scenarios. We find that the entropy of the critical point, at 21.8 k_{B}/atom, is reached for impacts with peak pressures of 605 GPa in the case of small planetesimals or for peak pressures of 825 GPa in the case of Mars-sized objects. Peak pressures of 312 GPa are enough to provide entropy higher than the entropy at boiling of iron at 1 atm, i.e. 15.84 k_{B}/atom (Kraus et al., 2015). These conditions can be easily exceeded during giant impacts between the proto-Earth and Theia, but could also be reached in almost half of the impacts with planetesimals during the late veneer. However, the liquid-vapor dome is reached only if the density, and hence the pressure, is allowed to decrease sufficiently. This can happen if the mantle is stripped away when fragments of the core are allowed to decompress without the mantle confinement.

mantle may prohibit the isentropic expansion and thus the vaporization (Fig. 3.13). But if during the impact parts of the mantle are detached from fragments of the core (Nakajima and Stevenson, 2015), then during the isentropic release these fragments will then undergo partial vaporization. Part of the vapor will remain in the outer part of the disk and eventually condense to form the Moon's core while the rest will fall into the central body and mix into the magma ocean.

Kendall and Melosh (2016) suggest fully mixing between impactor's core and proto-Earth Magma Ocean can be achieved for iron blobs that are less than 100 km across. Consequently, core fragmentation, promoted by partial vaporization during release, will enhance equilibrium and/or mixing between the impactor's core and the molten silicates, on a larger degree than the previous estimations of hydrodynamic simulations, which generally predicted the impactor's core directly merge into the Earth's core (Canup, 2012; Ćuk and Stewart, 2012). Then the mixing process can easily explain the recent W-isotope data, which require at least 30 % core-mantle equilibration in the aftermath of the giant impact (Nimmo et al., 2010; Rudge et al., 2010; Touboul et al., 2015).

3.4 Conclusions

In this chapter, we perform *ab initio* molecular dynamics to determine the position of the critical point of iron, and to characterize the fluid iron over a wide density and temperature range. Based on our calculations, we predict the critical point of iron to be in the 9000-9350 K temperature range and 1.85-2.40 g/cm^3 density range, corresponding to a pressures range of 4-7 kbars. We find that the low-density fluid is highly depolymerized, its structure dominated by isolated atoms and dimers. The coordination number increases strongly with density below 7.75 g/cm^3, then saturates at a value of 14 that persists at least up to 6000 K and 13.3 g/cm^3, which is the condition at the Earth's inner-outer core boundary. The viscosity of iron in the outer parts of the protolunar disk is also extremely low, on the order of 10^{-3} Pa s, which is one order of magnitude smaller than the value in the Earth's liquid outer core (de Wijs et al., 1998). A low viscosity implies a limited role in the global energy budget of the disk, a term oftentimes neglected in magneto-hydrodynamic simulations, and a possible presence of turbulence as the primary mechanism of transporting mass in the disk. Finally, the computed electronic and thermal conductivities decrease with the density, suggesting a gradual reduction of the metallic character. We do not observe any discontinuity in the density dependence of the electric conductivity. The only visible effect is that the electric conductivity falls more rapidly as the density decreases below 5.14 g/cm^3.

The determination of the Hugoniot lines and our estimations of the amounts of entropy gained during giant impacts show that the core of Theia underwent partial vaporization. This would easily explain the recent W-isotope data which requires at least 30% core-mantle equilibration in the aftermath of the giant impact (Nimmo

et al., 2010; Rudge et al., 2010; Touboul et al., 2015). Moreover, during the late veneer, a large fraction of the planetesimals' cores would undergo partial vaporization. This would help mixing the highly siderophile elements into magma ponds or oceans (Rubie et al., 2015).

Chapter 4

Ab initio Gibbs ensemble method and its application to sodium

Contents

4.1 Introduction

In the previous chapter, we used the spinodal line to estimate the position of the critical point of iron. As discussed by Binder et al. (2012), the spinodal line is due to the presence of an interface between the liquid and vapor phases as a result of the finite size effect. In this chapter, we present the Gibbs ensemble (GE) Monte Carlo (MC) method, which was first developed by Panagiotopoulos (1987) and is able to determine the liquid-vapour equilibrium without an explicit interface between two phases. In this method, we simulate two independent phases by two boxes at the same time and allow them to exchange volume and particles to reach the chemical equilibrium. Following this way, it directly mimics the macroscopic equilibrium at a microscopic level but avoids the interface issues allowing for a more reliable determination of the phase equilibrium. At this stage, we limit ourselves to the NVT version of the Gibbs ensemble where the number of particles (N), the total volume (V) of two boxes and the temperature (T) is fixed. As this method relies on a reasonable number of particle exchanges to achieve the same chemical potential, it is not very useful for studying equilibria involving high-density phases.

In the classical Gibbs ensemble scheme (Panagiotopoulos, 1987), the potential energy evaluated from a force field is used in the acceptance criterion for a trial move. This can be extended to include *ab initio* simulations, where the internal energy of the electron-ion system plays a similar role as the potential energy in the classical scheme. In the pioneering work of McGrath et al. (2005), the GEMC method has been combined with KS-DFT – often referred as *ab initio* (*ai*GEMC) – to improve its accuracy. Ever since different groups have applied the *ai*GEMC technique to calculate the liquid-vapor equilibrium line of water (McGrath et al., 2006a,b; Schienbein and Marx, 2018), methanol, methane (McGrath et al., 2011) and argon (Goel et al., 2018). All above materials are insulators and have a critical point that is below 700 K. Due to the relatively large band gaps, the thermal excitation of electrons in these systems is not significant, while it may play an important role in determining the phase equilibrium of metallic systems at high temperature. In order to capture the thermal excitations of electrons, it is necessary to make full use of FT-KS-DFT which explicitly includes the contribution of excited electronic states. Because of the extra electronic entropy term in FT-KS-DFT framework, a great care should be given to the electronic contribution as the excited states also play a role in the acceptance ratio. This problem is of considerable conceptual importance, and thus warrants a brief outline of statistical mechanics derivations in order to find an appropriate energy term that can be used in the acceptance criterion for a MC trial move. Here we chose the Monte Carlo method due to its simplicity for practical implementations. But the generalization to Gibbs ensemble molecular dynamics is straightforward (e.g. Palmer and Lo, 1994).

4.2 Statistical mechanics of the Gibbs ensemble

4.2.1 Partition function in the Gibbs ensemble

We start with Eq. 2.12, then perform the integral over the momenta $\{\boldsymbol{P}\}_N$ analytically and renormalize the coordinates $\{\boldsymbol{R}\}_N$ by the factor $L \equiv V^{1/3}$ leading to the standard configurational canonical NVT partition function $\mathcal{Z}^{\text{config}}(N, L, T)$ (Balian et al., 2007; Huang, 1987):

$$\begin{aligned} \mathcal{Z}(N,V,T) &= \frac{V^N}{N!\Lambda_{\text{dB}}^{3N}} \int \prod_{i=1}^{N} \mathrm{d}\boldsymbol{s}_i \ \exp\left(-\beta F_0(N, L, \{\boldsymbol{s}\}_N)\right) \\ &\equiv \frac{V^N}{N!\Lambda_{\text{dB}}^{3N}} \mathcal{Z}^{\text{config}}(N, L, T), \end{aligned} \tag{4.1}$$

where $\Lambda_{\text{dB}} = h/\sqrt{2\pi M k_B T}$ is the de Broglie wavelength, and $s_i \in [0;1]\ \forall i$, $F_0(N, L, \{\boldsymbol{s}\}_N)$ is an effective potential energy that is equal to $F_0(\{\boldsymbol{R}\}_N)$ as defined in Eq. 2.11. The Gibbs ensemble (Frenkel and Smit, 2001; Panagiotopoulos et al., 1988; Panagiotopoulos, 1987) is a particular case of the canonical ensemble, made of two sub-

systems of volumes V_1 and V_2 containing respectively N_1 and N_2 particles. The two sub-systems are in contact with the same thermostat and can exchange volume and atoms, but the sum $N_1 + N_2 = N$ and $V_1 + V_2 = V$ are conserved. This construction ensures that all the intensive quantities are equal when equilibrium is reached: temperature (by construction), pressure ($P_1 = P_2$) and chemical potential ($\mu_1 = \mu_2$). The corresponding partition function for the Gibbs ensemble is written as the product of the partition functions of each sub-system by Eq. (4.1) and sum over all volumes and particle distributions:

$$\begin{aligned}\mathcal{Z}_{\text{Gibbs}} &= \sum_{N_1=0}^{N_{\text{tot}}} \int_0^{V_{\text{tot}}} \mathrm{d}V_1 \mathcal{Z}_1(N_1, V_1, T) \times \mathcal{Z}_2(N_2, V_2, T) \\ &= \sum_{N_1=0}^{N_{\text{tot}}} \int_0^{V_{\text{tot}}} \mathrm{d}V_1 \frac{V_1^{N_1} V_2^{N_2}}{N_1! N_2! \Lambda_{\text{dB}}^{3(N_1+N_2)}} \\ &\quad \times \mathcal{Z}_1^{\text{config}}(N_1, L_1, T) \times \mathcal{Z}_2^{\text{config}}(N_2, L_2, T). \end{aligned} \tag{4.2}$$

From Eq. 4.2, we can see that one microstate in the Gibbs ensemble is specified by six parameters $(N_1, L_1, \{\boldsymbol{s}\}_{N_1}, N_2, L_2, \{\boldsymbol{s}\}_{N_2})$. It is also interesting to note that the partition function written as in Eq. 4.2 includes the possibility for one box to be empty or vanishing volume. Although counter-intuitive, these states, if explored by the GEMC algorithm, must be taken into account (Smit et al., 1989).

4.2.2 Monte Carlo in the canonical ensemble

A direct computation of the integral appearing in Eq. (4.1) or Eq. (4.2) is in general not possible, but most of the time we only need to estimate ensemble averages such as:

$$\langle \mathcal{A} \rangle = \frac{1}{\mathcal{Z}^{\text{config}}(N, L, T)} \int \prod_{i=1}^{N} \mathrm{d}\boldsymbol{s}_i \; \mathcal{A}(N, L, \{\boldsymbol{s}\}_N) \exp\left(-\beta F_0(N, L, \{\boldsymbol{s}\}_N)\right). \tag{4.3}$$

For such calculations specific methods have been developed among which is the famous MC importance sampling algorithm introduced by Metropolis et al. (1953). As such approaches are fairly well-known, we will only give the key features for the sake of completeness and to introduce the notations that we will need when presenting our numerical results.

The Metropolis algorithm is a Markov chain Monte Carlo method that can draw a sequence of random samples from the probability distribution of

$$\rho(\{\boldsymbol{s}\}_N) = \frac{\exp\{-\beta F_0(N, L, \{\boldsymbol{s}\}_N)\}}{\mathcal{Z}^{\text{config}}(N, L, T)} \tag{4.4}$$

without the need to know $\mathcal{Z}^{\text{config}}(N, L, T)$. For a Markov process, we need to define a transition probability $P(\{\boldsymbol{s}'\}_N|\{\boldsymbol{s}\}_N)$, which is the probability of transitioning from the current state $\{\boldsymbol{s}\}_N$ to any other state $\{\boldsymbol{s}'\}_N$. The choice of $P(\{\boldsymbol{s}'\}_N|\{\boldsymbol{s}\}_N)$ needs to meet the detailed balance,

$$\rho(\{\boldsymbol{s}\}_N)P(\{\boldsymbol{s}'\}_N|\{\boldsymbol{s}\}_N) = \rho(\{\boldsymbol{s}'\}_N)P(\{\boldsymbol{s}\}_N|\{\boldsymbol{s}'\}_N), \tag{4.5}$$

to assure that the Markov process asymptotically reaches a unique stationary distribution such that,

$$\lim_{n\to\infty} P^n(\{\boldsymbol{s}\}_N|\{\boldsymbol{s}'\}_N) = \rho(\{\boldsymbol{s}\}_N), \tag{4.6}$$

which is independent of the initial state $(\{\boldsymbol{s}'\}_N)$. If the initial state is not sampled from $\rho(\{\boldsymbol{s}\}_N)$, we need to equilibrate the system and discard the initial part of simulations. Metropolis et al. (1953) separate $P(\{\boldsymbol{s}'\}_N|\{\boldsymbol{s}\}_N)$ into two parts as,

$$P(\{\boldsymbol{s}'\}_N|\{\boldsymbol{s}\}_N) = Q(\{\boldsymbol{s}'\}_N|\{\boldsymbol{s}\}_N)A(\{\boldsymbol{s}'\}_N|\{\boldsymbol{s}\}_N) \tag{4.7}$$

where $Q(\{\boldsymbol{s}'\}_N|\{\boldsymbol{s}\}_N)$ is the conditional probability of proposing a state $\{\boldsymbol{s}'\}_N$ given $\{\boldsymbol{s}\}_N$ and chosen to be symmetric meaning $Q(\{\boldsymbol{s}'\}_N|\{\boldsymbol{s}\}_N) = Q(\{\boldsymbol{s}\}_N|\{\boldsymbol{s}'\}_N)$, $A(\{\boldsymbol{s}'\}_N|\{\boldsymbol{s}\}_N)$ is the acceptance ratio by

$$A(\{\boldsymbol{s}'\}_N|\{\boldsymbol{s}\}_N) = \min(1, \frac{\rho(\{\boldsymbol{s}'\}_N)}{\rho(\{\boldsymbol{s}\}_N)}). \tag{4.8}$$

Then the general procedure for each MC step is:

- compute the potential energy $(F_0(N, L, \{\boldsymbol{s}\}_N))$ of the system in the old state $\{\boldsymbol{s}\}_N$,
- make a move proposal based on $Q(\{\boldsymbol{s}'\}_N|\{\boldsymbol{s}\}_N)$,
- compute the potential energy $(F_0(N, L, \{\boldsymbol{s}'\}_N))$ of the system in the new state $\{\boldsymbol{s}'\}_N$,
- compute the energy change,
- accepte or reject the move proposal based on $A(\{\boldsymbol{s}'\}_N|\{\boldsymbol{s}\}_N)$.

4.2.3 Monte Carlo in the Gibbs ensemble: implementation and setup

In the GEMC method, we simulate two independent phases by two boxes simultaneously and allow them to exchange volume and particles. To realize this, three types of trial moves (Figure 4.1) are considered, namely

- a random displacement of a randomly chosen particle in each box $(j = 1, 2)$ to

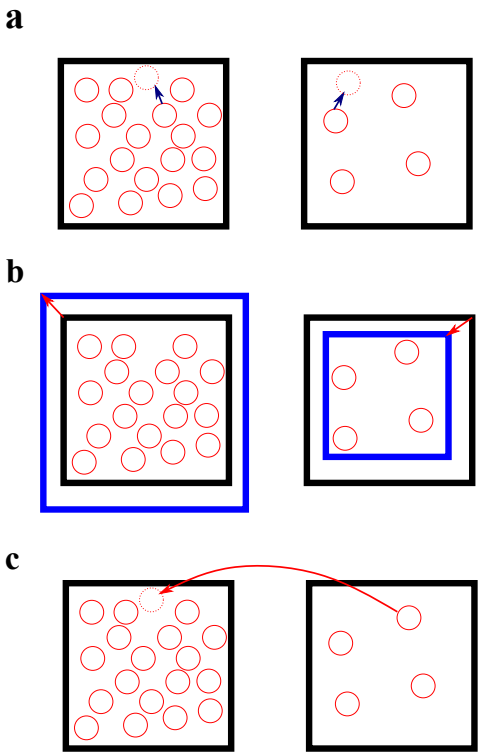

Figure 4.1: Three different Monte Carlo moves in the Gibbs ensemble method. (a) A random displacement of a randomly chosen particle in each box. (b) A random volume rearrangement. (c) The transfer of a randomly chosen particle between the two sub-systems. (see main text for more details)

relax both systems to the pre-defined temperature with an acceptance ratio of

$$A^j(\{\boldsymbol{s}'\}_{N_j}|\{\boldsymbol{s}\}_{N_j}) = \min(1, \frac{\exp\{-\beta F_0(N_j, L_j, \{\boldsymbol{s}'\}_{N_j})\}}{\exp\{-\beta F_0(N_j, L_j, \{\boldsymbol{s}\}_{N_j})\}}), \tag{4.9}$$

where we need to keep the volume (V_1, V_2) and number of particles (N_1, N_2) in both boxes unchanged,

- a random volume rearrangement $(V_1, V_2 \to V_1', V_2')$ to equate the pressure of these two boxes with an acceptance ratio of

$$A(V_1', V_2'|V_1, V_2) = \min(1, \left(\frac{V_1'}{V_1}\right)^{N_1} \left(\frac{V_2'}{V_2}\right)^{N_2} e^{-\beta\Delta(U_1+U_2)}), \tag{4.10}$$

where $\Delta U_j (j = 1, 2)$ is

$$\Delta U_j = F_0(N_j, L_j', \{\boldsymbol{s}\}_{N_j}) - F_0(N_j, L_j, \{\boldsymbol{s}\}_{N_j}), \tag{4.11}$$

and $V_1 + V_2 = V_1' + V_2' = V$

- a transfer of a randomly chosen particle between the two sub-systems ($N_1, N_2 \rightarrow N_1', N_2'$) to equate the chemical potential with an acceptance ratio of

$$A(N_1', N_2'|N_1, N_2) = \left(\frac{V_2}{V_1}\right)\left(\frac{N_1}{N_2'}\right) e^{-\beta\Delta(U_1+U_2)}, \tag{4.12}$$

  where $\Delta U_j (j = 1, 2)$ is

$$\Delta U_j = F_0(N_j', L_j, \{\boldsymbol{s}\}_{N_j'}) - F_0(N_j, L_j, \{\boldsymbol{s}\}_{N_j}), \tag{4.13}$$

  and $N_1 + N_2 = N_1' + N_2' = N$.

The derivation of the acceptance ratio can be found in Panagiotopoulos (1987). Here I show an example of how to derive Eq. 4.12. The relative weight of two microstates in the Gibbs ensemble is:

$$\frac{\rho(N_1', L_1', \{\boldsymbol{s}\}_{N_1'}, N_2', L_2', \{\boldsymbol{s}\}_{N_2'})}{\rho(N_1, L_1, \{\boldsymbol{s}\}_{N_1}, N_2, L_2, \{\boldsymbol{s}\}_{N_2})} = \frac{\frac{V_1'^{N_1'} V_2'^{N_2'}}{N_1'! N_2'! \Lambda_{\mathrm{dB}}^{3(N_1'+N_2')}} \exp\left(-\beta F_0(N_1', L_1', \{\boldsymbol{s}\}_{N_1'}\right) \exp\left(-\beta F_0(N_2', L_2', \{\boldsymbol{s}\}_{N_2'}\right)}{\frac{V_1^{N_1} V_2^{N_2}}{N_1! N_2! \Lambda_{\mathrm{dB}}^{3(N_1+N_2)}} \exp\left(-\beta F_0(N_1, L_1, \{\boldsymbol{s}\}_{N_1}\right) \exp\left(-\beta F_0(N_2, L_2, \{\boldsymbol{s}\}_{N_2}\right)}. \tag{4.14}$$

After plugging in $N_1 = N_1', N_2 = N_2', \{\boldsymbol{s}\}_{N_1} = \{\boldsymbol{s}\}_{N_1'}, \{\boldsymbol{s}\}_{N_2} = \{\boldsymbol{s}\}_{N_2'}$, it can be reduced to:

$$\frac{\rho(N_1, L_1', \{\boldsymbol{s}\}_{N_1}, N_2, L_2', \{\boldsymbol{s}\}_{N_2})}{\rho(N_1, L_1, \{\boldsymbol{s}\}_{N_1}, N_2, L_2, \{\boldsymbol{s}\}_{N_2})} = \left(\frac{V_1'}{V_1}\right)^{N_1}\left(\frac{V_2'}{V_2}\right)^{N_2} e^{-\beta\Delta(U_1+U_2)} \tag{4.15}$$

where ΔU_1 and ΔU_2 are defined in Eq. 4.11.

The implementation of the Markov chain described in the previous section is relatively straightforward. We define three probabilities $\eta_{\text{Displ.}} = 0.5$, $\eta_{\text{Vol.}} = 0.25$, and $\eta_{\text{Part.}} = 0.25$ for the choice among the different moves for each cycle, such as $\eta_{\text{Displ.}} + \eta_{\text{Vol.}} + \eta_{\text{Part.}} = 1$. We define $\delta s_{\max}$ as the maximal (normalized) particle displacement, which can be different for the two boxes, chosen such as to reach an acceptance ratio for moves of type (i) around 50% for each sub-system, and $\delta V_{\max}$ as the maximal volume exchange, similarly optimized for an acceptance rate of about 50%. The detailed values are compiled in Tab. 4.2.

In particular for sodium we used as initial conditions a liquid box of 17 Å with 80 atoms and an empty vapor box of 25 Å for the simulations below 2000 K, and a liquid box of 18 Å with 80 atoms and an empty vapor box of 18 Å at 2000 K. One accepted configuration at 2000 K served as starting point for the simulations at 2100K, 2200 K, 2300K and 2400 K. At 2500 K, we start with two 40-atoms boxes of

17 Å. In addition, we have performed an extra simulation at 2000 K with 120 atoms to estimate the finite-size effect, which is found to be small at this condition (see Figure 4.4). All the simulation boxes are cubic and the dimensions above define the edge of the box. The equilibrium values and their uncertainty were calculated using the autocorrelation technique (Frenkel and Smit, 2001). The error bars reported in the following sections are one-sigma error bars.

4.2.4 Setup of the DFT calculations

We compute the energy of the two sub-systems at each MC step using first-principles calculations in the projector augmented wave (PAW) method (Blöchl, 1994; Kresse and Joubert, 1999) of the DFT in the VASP (Kresse and Furthmüller, 1996; Kresse and Furthmüller, 1996) implementation. We employ the Generalized-Gradient Approximation in the Perdew-Burke-Ernzerhof formalism (Perdew et al., 1996) for the exchange correlation term. We treat the $3s^1$ as valence electron configurations for the PAW pseudopotentials. The partial occupancies for the electronic calculation are calculated using a Fermi-Dirac smearing scheme with a width corresponding to the nuclear temperature. The energy cut-off for the plane-wave basis set was set to 400 eV. The break condition for the electronic self-consistent loop was 10^{-4} eV. The number of electronic bands was adapted to the temperature conditions such as to cover the entire spectrum of the fully and partially occupied states and to include enough non-occupied bands. The Brillouin zone was sampled with the Baldereschi point (Baldereschi, 1973). A test with a grid of $2 \times 2 \times 2$ **k**-points yields results within 0.5% difference in energy. At each MC step, for each ionic configuration we compute the effect potential energy F_0 as defined in Eq.2.11 including the free energy of the electrons in a coulombic potential due to the ions and the ion-ion interaction. Our implementation is done outside of the VASP package (Kresse and Furthmüller, 1996), which is called only as an energy routine.

To compare with the Gibbs ensemble method, we also performed molecular dynamics simulations of the liquid phase in the DFT framework at several densities along the 2000 K isotherm. In order to stay consistent with the MC calculations we used the same DFT parameters for the MD simulations. The temperature was kept constant thanks to a Nosé thermostat (Nosé, 1984). We used a fixed volume cell containing 80 atoms. The time step was set to 2 fs for a total duration of 20 ps.

4.3 Results and discussion

4.3.1 Stationary state and equilibrium

At the very beginning of the simulation, there is a net particle flux from the liquid box to the vapor box since the latter is initially empty (Figure 4.2). The driving force is the difference in chemical potentials. Because of the random character of the acceptance of moves along the Markov chains, particles from the gas box may also be transferred to the liquid box. This is captured by fluctuations of the density

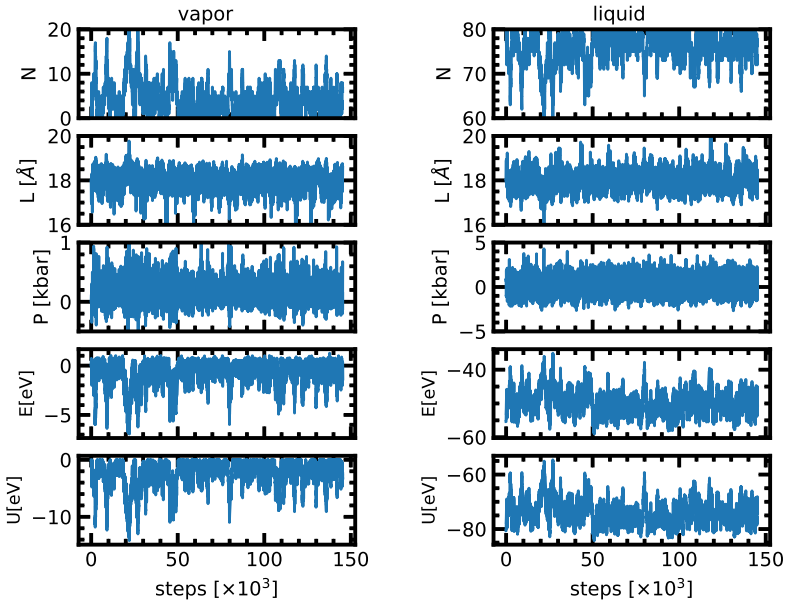

Figure 4.2: Evolution of the number of particles (N), cell length (L), pressure (P), internal energy (E) and effective potential energy (U) as a function of Monte Carlo steps in the vapor and in the liquid phase for the simulation at 2000 K.

in each of the two boxes. After about 20000-50000 attempted moves, both boxes have reached a stationary state and the equilibrium is achieved. At equilibrium, for a temperature of 2000 K the cell length of both boxes fluctuates around 18 Å. The pressure in the liquid phase is 0.0 ± 0.2 kbar and 0.08 ± 0.03 kbar for the vapor phase. The liquid phase has 76 atoms on average but the vapor phase only 4. The stationary state thus seems to correspond to a thermal, dynamical and chemical equilibrium.

The acceptance ratios reported in Tab. 4.2 are very satisfactory with typical values between 10 and 75 % for each move. The 1200 K simulation shows a very low acceptance rate for the particle exchange because the temperature is very low compared to the energy barrier. Since the acceptance rate is non zero, the results are still reliable since a long enough simulation has been run. Figure 4.2 shows the evolution of different quantities as a function of the MC step at 2000 K. Table 4.1 lists all the values of the thermodynamic quantities.

4.3.2 Liquid-vapor equilibrium

As can be seen from Figure 4.3, at low temperature there is a clear distinction between the low-density and the high-density phase that corresponds to the liquid and vapour phase. It is then possible to determine the average thermodynamic quantities of both the vapor and the liquid phases by averaging over each distinct distribution.

Table 4.1: Thermodynamic averages for the liquid and vapor phases for the *ab inito* Gibbs ensemble simulations. The uncertainties correspond to the one-sigma error bar.

Temperature (K)	N_{vap}	N_{liq}	ρ_{vap} (g/cm^3)	ρ_{liq} (g/cm^3)	P_{vap} (kbar)	P_{liq} (kbar)	U_{vap} (eV)	U_{liq} (eV)
1200	0.04 ± 0.02	79.96 ± 0.02	9e-5 ± 4e-5	0.60±0.01	2e-4±1e-4	-0.36±0.35	-0.011±0.008	-83.47± 0.16
1500	0.52 ± 0.32	79.48 ± 2.35	0.001 ± 0.0008	0.58 ±0.01	0.003±0.001	-0.37±0.34	-0.23±0.04	-81.55± 0.32
1800	2.26 ± 0.67	78.74 ± 1.52	0.014 ± 0.004	0.54 ±0.01	0.06 ± 0.03	-0.21 ± 0.28	-1.01 ± 0.33	-78.94 ± 0.45
2000	4.22 ± 1.86	75.78 ± 1.88	0.03 ± 0.01	0.50 ±0.02	0.08±0.03	0.0±0.2	-2.33±0.37	-74.19± 0.67
2000[1]	7.48 ± 2.90	112.52 ± 3.22	0.04 ± 0.01	0.51 ± 0.02	0.10 ±0.01	0.20 ±0.34	-4.34 ± 1.51	-111.38 ± 1.03
2100	7.20 ± 1.59	72.80 ± 2.42	0.05 ± 0.01	0.46 ± 0.02	0.12 ± 0.05	0.20 ± 0.23	-69.44 ± 1.45	-5.11 ± 1.93
2200	12.27 ± 2.35	59.20 ± 6.29	0.074 ± 0.02	0.43 ±0.05	0.15±0.08	0.44±0.50	-8.06±1.54	-55.99± 6.52
2300	14.47 ± 3.84	57.07 ± 12.22	0.15 ± 0.04	0.42 ±0.07	0.13 ±0.52	0.36 ±0.67	-10.35 ± 3.28	-52.97± 11.89
2400[2]	38.37 ± 5.44	41.63 ± 5.32	0.28 ± 0.04	0.26 ±0.03	0.33±0.13	0.43±0.11	-32.25±0.98	-34.63± 0.74
2500[2]	38.54 ± 6.60	41.46 ± 7.98	0.31 ± 0.03	0.32 ±0.04	0.44±0.24	0.46±0.20	-31.42±1.71	-38.27± 0.84

[1] We perform an extra simulation at 2000 K with 120 atoms to estimate the finite-size effect on the liquid-vapour equilibrium density.

[2] At 2400 and 2500 K, only one phase is present. The density, pressure, effective energy of gas and liquid phase indicate the average properties in each box.

Table 4.2: Acceptance ratio for the different moves in the present *ab initio* Gibbs ensemble study at 1200, 1500, 1800, 2000, 2100, 2200, 2300, 2400 and 2500 K. The maximum displacement $\delta s_{\max}$ is in reduced coordinates of [0,1).

Temperature	Particle displacement in Box1		Particle displacement in Box2		Volume exchange		Atom swap
[K]	acceptance ratio	$\delta s_{\max}$	acceptance ratio	$\delta s_{\max}$	acceptance ratio	$\delta V_{\max}[\text{Å}^3]$	acceptance ratio
1200	0.50	0.035	0.78	0.23	0.55	300	0.006
1500	0.41	0.052	0.73	0.16	0.50	420	0.07
1800	0.58	0.05	0.41	0.10	0.45	700	0.13
2000	0.54	0.055	0.50	0.13	0.60	550	0.18
2000[1]	0.48	0.04	0.39	0.1	0.46	700	0.14
2100	0.52	0.07	0.54	0.1	0.56	700	0.21
2200	0.49	0.072	0.58	0.08	0.57	710	0.26
2300	0.61	0.07	0.45	0.10	0.52	800	0.29
2400	0.53	0.078	0.55	0.08	0.59	650	0.39
2500	0.50	0.078	0.53	0.08	0.52	650	0.37

[1]We perform an extra simulation at 2000 K with 120 atoms to estimate the finite-size effect on the liquid-vapour equilibrium density.

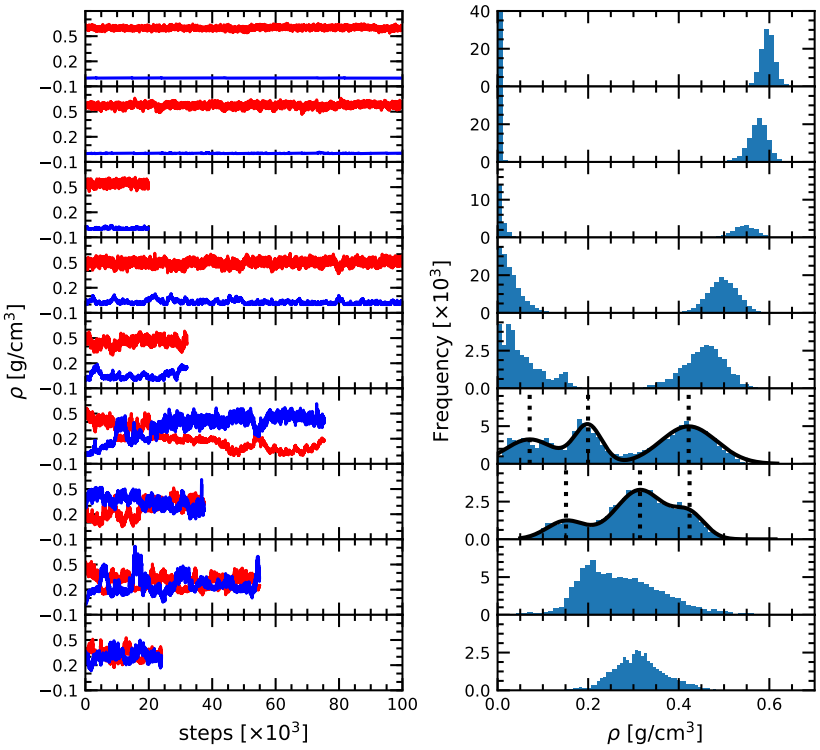

Figure 4.3: (A) Density *versus* Monte Carlo steps for the Gibbs ensemble simulations at 1200, 1500, 1800, 2000, 2100, 2200, 2300, 2400 and 2500 K from top to bottom, respectively. (B) Corresponding unnormalized probability distribution functions.

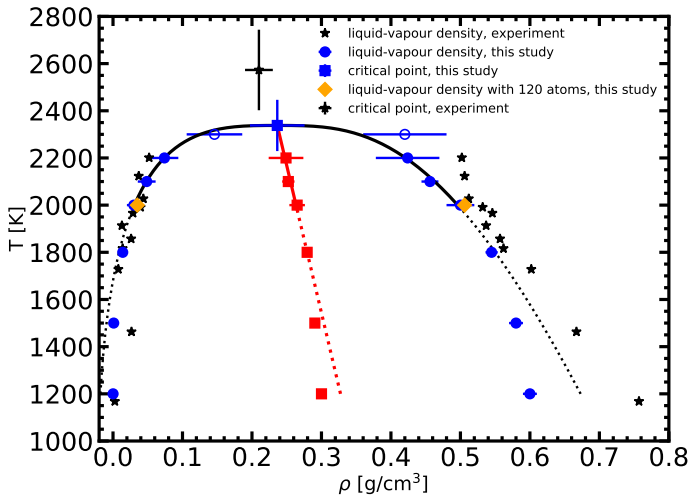

Figure 4.4: Liquid-vapor equilibrium of Na obtained from the *ab initio* Gibbs ensemble simulations (blue circles) and its comparison with the experiment (Dillon et al., 1966) (black stars). The blue line is a fit of the equilibrium line using the scaling law and the red line is the law of rectilinear diameter with $A = 0.80 \pm 0.02$ and $B = 0.07 \pm 0.01$ parameters (see text for more details).

As temperature increases the two peaks become less and less separated, eventually preventing for a clear difference between the two phases. As we approach the critical temperature, the simulations have a higher probability of switching identity or even having two phases at once in the same simulation box. The latter is due to a comparable magnitude of the surface tension effect and the entropy contribution as already observed by Smit et al. (1989). It results in the appearance of three peaks in the density distribution plot. In order to better quantify the density of the three phases (gas, liquid and the mixed phase), we fitted the three peaks by three Gaussian functions (solid black line in Figure 4.3) as suggested by Smit et al. (1989). The center of the Gaussian is assumed to be the average density of each phase and its width is the standard deviation entering in the determination of the uncertainty. The low density peak corresponds to the gaseous phase and the high density peak to the liquid phase. The middle peak, close to the average density of the two boxes is the mixed phase, and is disregarded in the liquid-vapor equilibrium analysis. At 2300 K, the fluctuations become extremely large and we thus decided to only show the results in the density plot for reference but not to use them for the fit since they offer too loose a constraint on the critical point. For 2400 and 2500 K both boxes reach a very similar equilibrium and seem identical. This means that these conditions are above the critical point.

Based on the equilibrium densities, we can plot a vapor-liquid coexistence curve as shown in Figure 4.4. In general we obtain a good agreement compared to ex-

perimental data available in the literature (Dillon et al., 1966). At 1200 K, the saturated liquid density is 20% lower than that of experiments, which may be due to the choice of the exchange correlation functional that has already been noted in previous studies of argon (Goel et al., 2018). A precise direct determination of the critical point is made difficult by the finite size of our system since the correlation length is expected to tend to infinity at the critical point; this cannot be captured within our small simulation cells. The critical point may however be approximated using the law of rectilinear diameter (Rowlinson and Swinton, 1982):

$$\rho_L + \rho_V = 2\left[\rho_c + B\left(1 - \frac{T}{T_c}\right)\right] \tag{4.16}$$

together with the scaling law (Rowlinson and Widom, 1982)

$$\rho_L - \rho_V = A\left(1 - \frac{T}{T_c}\right)^{\beta}, \tag{4.17}$$

where ρ_L and ρ_V are the densities of the coexisting liquid and vapor, at a given temperature T. The fitted parameters are the critical temperature T_c and density ρ_c, and the two constants A and B. β is the critical exponent, which is fixed here at 0.326 (Wilding, 1995), as for other three dimensional systems (Frenkel and Smit, 2001; Rowlinson and Widom, 1982).

We obtained the critical point by applying the scaling law to all data points above 2000 K. Using our data we obtain our best fit with $A = 0.87 \pm 0.1$ and $B = 0.19 \pm 0.03$. The critical point lies at 2338 ± 108 K and 0.24 ± 0.03 g/cm^3. We stress here that the density values at 1800 K are compatible with the extrapolation of the scaling law, providing confidence in our fit. Our theoretical critical temperature is slightly lower than the experimental value at 2573 ± 171 K (Dillon et al., 1966), and the critical density is similar to the experimental value of 0.21 ± 0.02 g/cm^3. We want to underline that both our values and the experimental ones are the result of extrapolations, as in both cases it is too challenging to obtain equilibrium data in the very vicinity of the critical point. With this in mind, the good agreement that we obtain between our calculations and experiments confirms the suitability of the *ab initio* Gibbs ensemble method for the determination of accurate coexistence curves. We also include the Clausius-Clapeyron plot of the saturated vapor pressure and density as a function of the inverse temperature in Figure 4.6. We obtain a nice affine behavior for both the logarithm of the density and of the pressure on these plots. We also have a relatively good agreement with the experimental density data.

In order to check our Gibbs ensemble results, we also performed a set of *ab initio* molecular dynamics simulations in the canonical ensemble at 2000 K for different densities. This allows us to analyse the structure of the liquid and to determine the corresponding spinodal point (Speedy, 1982). Figure 4.5 shows the variation of pressure as a function of the density along the 2000 K isotherm. This curve exhibits

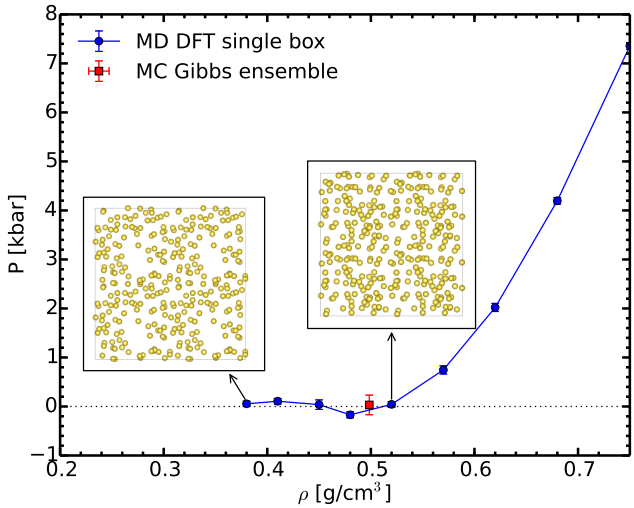

Figure 4.5: Pressure evolution during the isothermal volume expansion for sodium at 2000 K. The insets show the snapshots at 0.52 and 0.38 g/cm^3, respectively.

a clear minimum close to 0.48 g/cm^3; this is the liquid spinodal point. This is the smallest density at which the liquid is metastable. Above this density the fluid is homogeneous, as shown for example in the insets of Figure 4.5. At lower densities, in the unstable branch, bubbles form proving that the liquid becomes unstable. The density of the spinodal point is close yet lower than the equilibrium density of 0.50 ± 0.02 g/cm^3 predicted by the Gibbs ensemble method. We thus have a full consistency between these two completely different methods ensuring the reliability of the Gibbs ensemble method.

4.3.3 Structure of the liquid

We compare the structure of the liquid as we obtain it using the MC Gibbs ensemble and the MD approach. We analyse the radial distribution function (RDF)(also see Section 3.2.3) and stress here that the calculation of the RDF in the Gibbs ensemble is performed on a series of snapshots, and the number of particles and volume of each phase fluctuate. Figure 4.7 shows the RDF at several temperatures as extracted from our Gibbs ensemble simulations. The main peak lies around 3.5 Å. Along the vapor-liquid equilibrium line, the position of the peak changes slightly and broadens due mostly to the temperature effects. The spherical integration of the RDF from 0 to its first minimum gives the coordination number. At 2000 K and 0.52 g/cm^3 the agreement of the RDF as obtained in the MC and in the MD simulations is excellent. As the two methods start from different initial configurations and use different paths, they give a remarkable consistent outcome as they explore the configurational space. While this is not an absolute proof that we achieved ergodicity, it strongly suggests that our simulations are satisfying it.

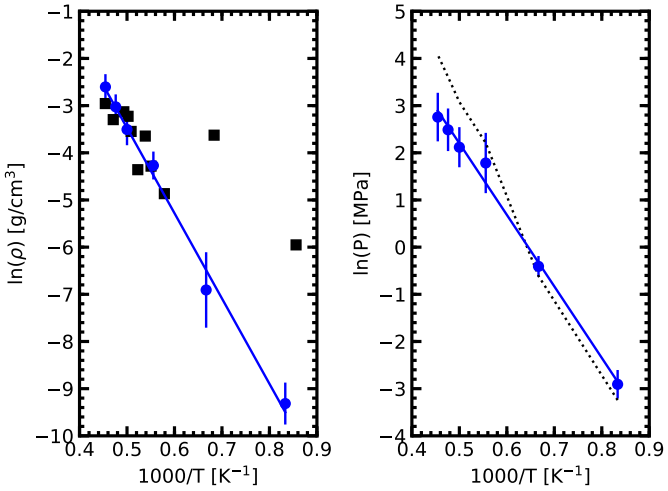

Figure 4.6: Clausius-Clapeyron plot of the logarithm of the saturated vapor pressure and density as a function of the inverse temperature. The solid black squares are experimental date (Dillon et al., 1966). The dashed line on the right graph denotes the pressures from fitting vapor density to the ideal gas law. As expected, a good agreement with calculated pressure is achieved in the low density range. In the high density region, a deviation is observed.

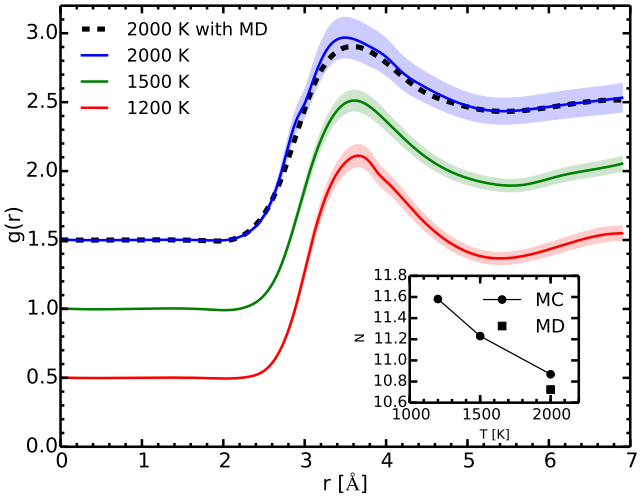

Figure 4.7: Radial distribution function (RDF) $g(r)$ at 1200, 1500 and 2000 K in the liquid phase as computed with the Gibbs ensemble MC simulations (full lines) and with the MD one at 0.52 g/cm^3, 2000 K (dotted line). The shaded areas correspond to our estimate of the one-sigma uncertainty. The curves were shifted for readability. The inset shows the coordination number as a function of the temperature.

4.4 Conclusions

We have implemented the *ab initio* Gibbs ensemble algorithm and performed a series of simulations to compute the liquid-vapor equilibrium line and the critical point of sodium. We emphasize the electronic contribution at finite temperature, which is essential for metallic systems, but not always clearly explained in the literature. The effective nuclear potential energy defined in Eq. 2.11 should be used in the acceptance rule for a MC trial move in the Gibbs ensemble. We demonstrated that our simulations reached a mechanical and chemical equilibrium and the calculated phase coexistence curve and critical point of sodium are in a good agreement with the experimental results. The comparison of our results with molecular dynamics also showed very good consistency. Therefore, we confirm the reliability and validity of the *ab initio* Gibbs ensemble method.

Chapter 5

Ab initio Gibbs ensemble study of the liquid-vapor equilibrium and critical point of iron

Contents

5.1 Introduction

Iron, as the major constitutive material of the metallic core in a telluric planet and as a basic engineering material, has received and continues to receive considerable attention from academics across multiple disciplines. Significant efforts were made for studying the thermodynamic and thermophysical properties of its liquid and solid phases for a wide range of temperature and pressure conditions by either experimental or theoretical methods. These information have been used, on the one hand, to design new technological devices, and on the other hand, to infer the physical state and investigate the thermodynamic evolution of planetary cores. Recent developments in the field of extreme shock experiments and giant impact simulations led to an increased interest in obtaining a complete thermal equation of state (EOS) that can describe all vapor, liquid and solid phases of iron (Canup, 2004a). However, only a few studies have been performed to examine the vapor-liquid equilibrium (VLE) and the critical point (CP) of iron (Assael et al., 2006; Grosse and Kirshenbaum, 1963; Hixson et al., 1990). The scarceness of data inhibited building an accurate set of EOS for iron that spans a wide-enough density and temperature

region to cover all the different phases of interest. These limitations cause problems in predicting the chemical and dynamic consequences in a giant impact simulation. Therefore, it is imperative to close the knowledge gap of the VLE and CP of iron.

However, it is still challenging to determine the VLE and CP experimentally above 4000 K. Computer simulations might provide an alternative option and sometimes are the only viable way. The Gibbs ensemble Monte Carlo (GEMC) method, coupled to finite-temperature density functional theory, has just opened up the possibility of studying the VLE and CP for a metallic system with a reasonable computational cost. Its first application to sodium has shown an excellent agreement with available experimental results (see Chapter 4). Unfortunately, we cannot directly apply this technique to iron due to the additional complication from the high-temperature magnetism.

Both experiments (Waseda and Suzuki, 1970) and theoretical simulations (Lichtenstein et al., 2001) suggest that the liquid iron might be in a paramagnetic state with a non-vanishing local magnetic moment at ambient pressure. Therefore, we need to take into account the magnetic excitation or the magnetic degrees of freedom, including the transversal fluctuation, which changes the orientation of the local magnetic moment, and the longitudinal fluctuation that modifies the magnitude of the local magnetic moment (Kaul, 2007). We must remind the readers that a spin-polarized DFT calculation with a fully self-consistent electronic optimization to find the electronic ground state will only yield the size and direction of the local magnetic moment that corresponds to the zero temperature on the magnetic degrees of freedom (Gambino et al., 2020). As pointed out by Abrikosov et al. (2016), the variation in the size and orientation of the local magnetic moment observed in the spin-polarized *ab initio* molecular dynamics simulations is only a direct impact of atom vibrations.

Several new approaches have been developed to study the magnetic excitation. Among them, the accurate one is based on the dynamic mean-field theory (Lichtenstein et al., 2001). Because of the computational limitations and poor tractability, this technique is still limited to a small system size that is insufficient to properly describe the structural disorder of a fluid, even metallic like iron. To reduce the complexity to a manageable extent, we first note that each iron atom can be associated with a well-defined local magnetic moment that behaves in a Heisenberg-like manner, although $3d$ itinerant electrons cause the magnetism (Abrikosov et al., 2016). It suggests that the longitudinal fluctuation might play a limited role and is thus often neglected. We can further simplify the problem by considering that the magnetic fluctuations adiabatically follow the atomic motions. This treatment is a special case of the disordered local moment molecular dynamics (DLM+MD), where the paramagnetic state is realized by the statistical average of many different random magnetic configurations known as the magnetic sampling method (Alling et al., 2010). In this way, we treat the atomic vibrations and the transversal fluctuations on a similar footing. However, the incorporation of the magnetic degrees

of freedom into the *ai*GEMC method is too expensive. Fortunately, as we shall see later, the paramagnetic state can be well approximated by the ferromagnetic state in terms of the liquid-vapor equilibrium densities.

In the present study, we employed the *ai*GEMC method to determine the liquid-vapor equilibrium line and the critical point of iron in the non-magnetic (NM) and ferromagnetic (FM) state. Then we used DLM+MD method to determine the equilibrium density for the liquid iron from 1800-7500 K at 0 GPa, where the paramagnetic (PM) state is treated by the magnetic sampling method.

5.2 Simulation details

In the *ai*GEMC method, we simulate two independent phases (liquid and vapor) by two boxes simultaneously but allow them to exchange volume and particles to achieve the chemical equilibrium. We employed finite-temperature density functional theory (Hohenberg and Kohn, 1964; Kohn and Sham, 1965; Mermin, 1965) as implemented in the Vienna Ab initio Simulation Package (VASP) (Kresse and Furthmüller, 1996; Kresse and Furthmüller, 1996) to compute the effective potential energy for the Monte Carlo acceptance criteria. The Perdew-Burke-Ernzerhof functional (Perdew et al., 1996) and the projector augmented wave (PAW) potential (Blöchl, 1994; Kresse and Joubert, 1999) with $3d^7 4s^1$ as valence electrons were used. The partial occupancies for the electronic structure calculation were calculated using a Fermi-Dirac smearing scheme with a width corresponding to the simulation temperature. The energy cut-off for the plane-wave basis set was set to 400 eV and the Brillouin zone was sampled with the Baldereschi point (Baldereschi, 1973). For the *ab initio* molecular dynamics simulations, we used the same DFT parameters as the MC calculations to be consistent. The temperature was controlled by the Nosé thermostat (Nosé, 1984). The timestep of the *ai*MD simulation was set to 1 fs for a total simulation time of at least 3 ps. For the paramagnetic phase, the transversal fluctuation is taken into account by the magnetic sampling method. We exploited 40 magnetic configurations at every MD step to obtain the average force exerted on atoms, where the initial local magnetic moments for the electronic minimization were set to be orientated in a randomly spin-up or down direction but with a zero total magnetic moment in the simulation cell (Alling et al., 2010). For the ferromagnetic phase, we reinitialized the system to be ferromagnetic at every MD step in order to prevent the electronic subsystem from getting stuck in a local minimum during the electronic minimization. In this study, we used 80 atoms for both *ai*GEMC and *ai*MD simulations. But an extra *ai*GEMC simulation with 108 atoms at 7500 K has been performed to estimate the finite size effects.

5.3 Results and Discussion

5.3.1 The liquid-vapor equilibrium line from *ai*GEMC simulations

5.3.1.1 The nonmagnetic case

First, we approximate the paramagnetic state by a nonmagnetic simulation. We plot the density evolution as a function of MC step in Fig. 5.1(a). In order to verify that the simulation results are independent of the initial condition, including the starting volume and atomic positions for each box and the total volume of the two boxes, we perform two *ai*GEMC simulations at 3500 K. The first simulation employs two identical boxes, each with 40 particles and the same atomic position. The second simulation starts with one empty box and one box with 80 atoms. However, these two simulations have different total volumes.

In the former case, we observe an instantaneous phase separation, *i.e.* all the atoms move into one box, leaving the other one empty (Fig. 5.1(a)). When the atoms are transferred into one fully populated box, its volume also changes to accommodate this amount of atoms. Even if one box becomes empty, there is still a volume exchange between the two boxes. Eventually, the simulation converges to 10.11^3 Å^3 for the liquid box, which corresponds to 7.18 ± 0.03 g/cm^3 density. In the second case, we did not observe any particle transfer between the two boxes, but the volume exchange is still present. Its final volume is 10.15^3 Å^3, which corresponds to 7.10 g/cm^3 $\pm$ 0.05 density. Consequently, we observe that the two simulations yield the same density for the liquid iron phase, suggesting that the value of the density we obtain using this procedure is reliable.

As we approach the critical point, we observe that the density of the equilibrium liquid drops with increasing temperature. We also observe the appearance of the first atoms in the vapor box at 5000 K, and the equilibrium vapor density increases with increasing temperature. At 7500 K, we perform another simulation with 108 iron atoms to estimate the finite-size effects, which is found to be small.

We plot the unnormalized density probability distribution functions in Fig. 5.1(b). There are two well-separated peaks in the density histogram below 7500 K, which corresponds to the liquid and vapor phase. At 8500 K, there is a significant fluctuation in the density evolution since the temperature is very close to the critical temperature. At 9500 K, the two boxes frequently exchange their identities, and a single peak is present, indicating the simulated temperature is above the critical temperature.

Coming back to the simulations at 3500 K, the extrapolated density of the vapor phase at this temperature should be on the order of 10^{-4} g/cm^3. It implies that we need to exploit a simulation cell of at least 200^3 Å^3. Due to the limitation on the computation facilities, we could not further increase the simulation cell beyond the 70^3 Å^3 which is used in the present study at 3500 K. However, an empty vapor box should not affect the accuracy of the liquid equilibrium density and position of the

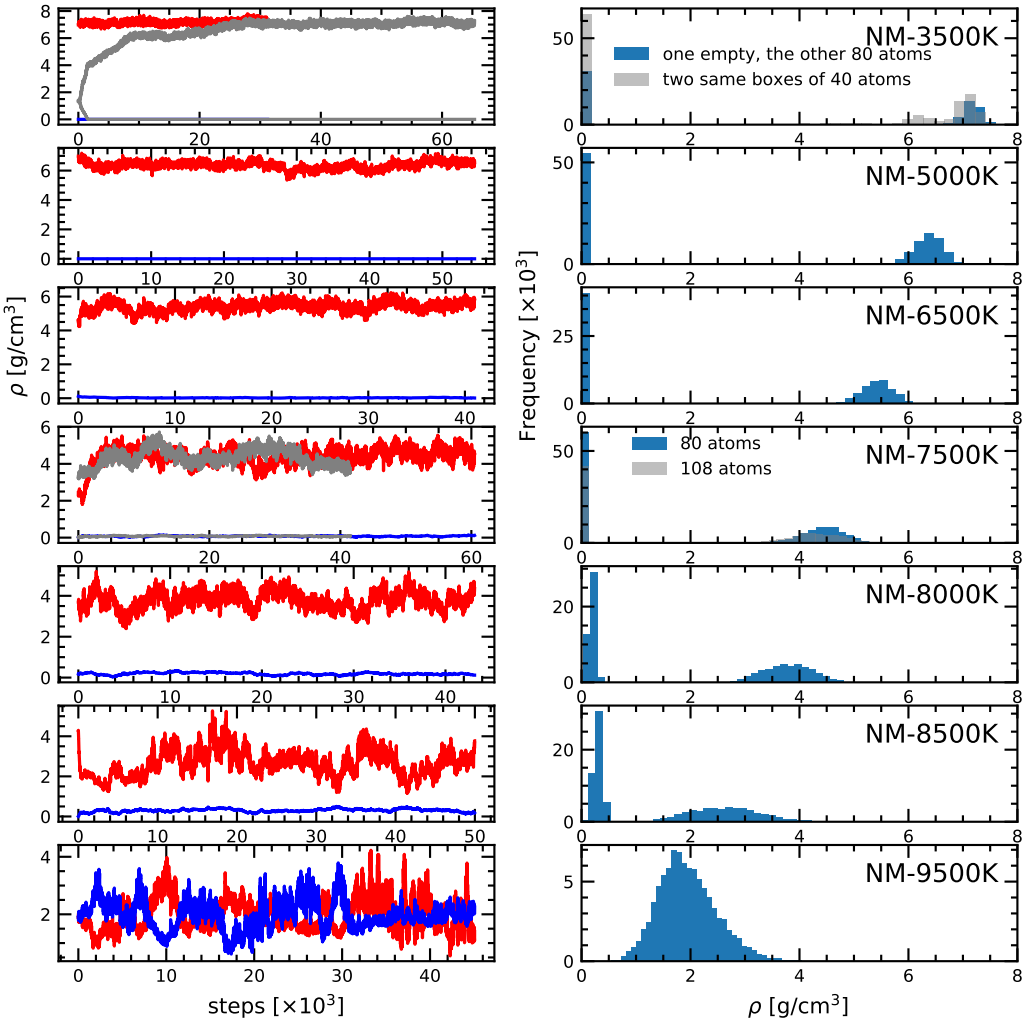

Figure 5.1: (a) The evolution of density as a function of Monte Carlo step from the *ai*GEMC simulations for iron in the nonmagnetic state at 3500, 5000, 6500, 7500, 8500 and 9500 K from top to bottom, respectively. (b) Corresponding unnormalized probability distribution functions. An extra simulation has been performed at 3500 K to examine whether the simulation results depend on the initial condition. By running the *ai*GEMC simulation with 108 iron atoms at 7500 K, we found the finite size effects are small at this condition.

critical point. The empty box without any atom acts like a pressure buffer and sets the pressure on the liquid phase to zero. Although the real equilibrium pressure at 3500 K is not zero if a sufficiently large simulation cell is employed, it should be very close to zero. As we will explain in Section 5.3.4, a variation of even 1 GPa in pressure only changes the density of the liquid by less than 1% at 3500 K. Therefore, the zero pressure density for the liquid phase is an excellent approximation to the equilibrium liquid density.

5.3.1.2 The ferromagnetic case

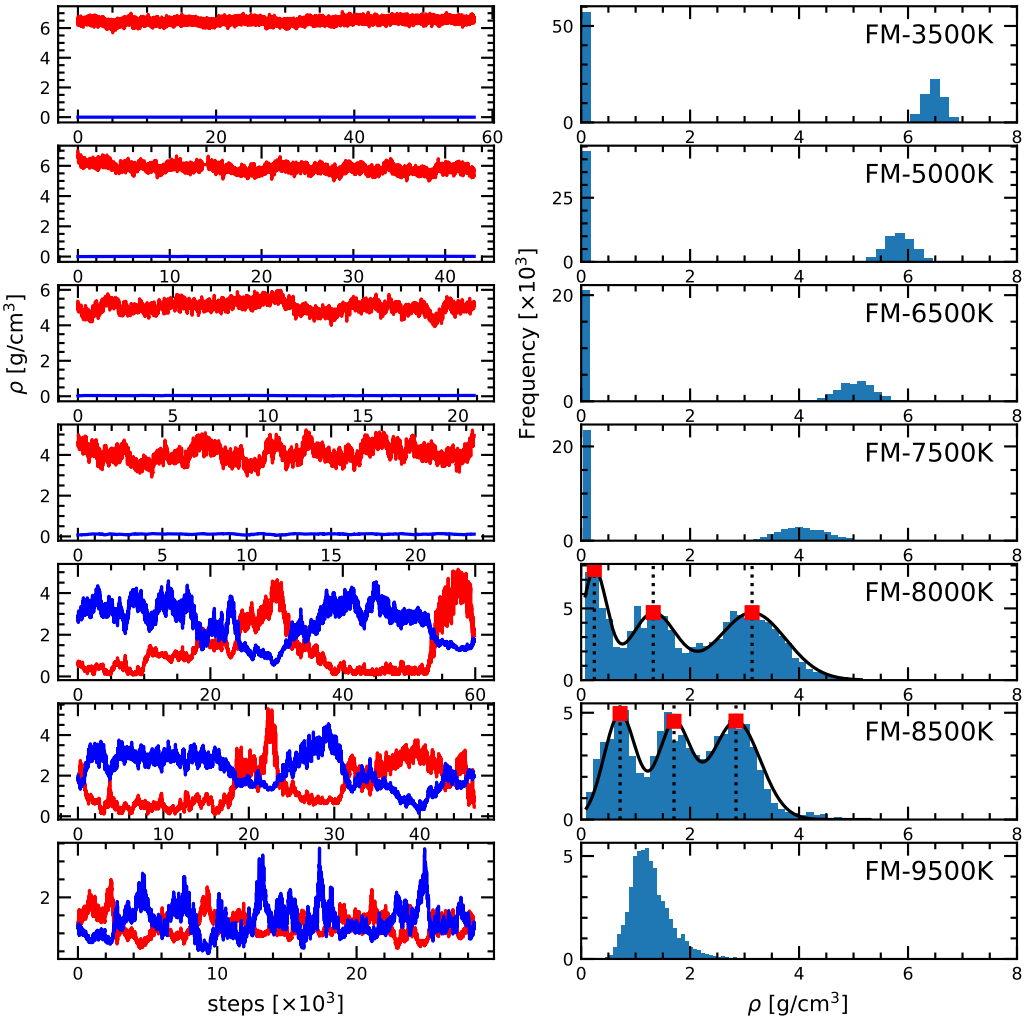

Figure 5.2: (a) The evolution of density as a function of Monte Carlo step from the *ai*GEMC simulations with iron in the ferromagnetic state at 3500, 5000, 6500, 7500, 8500, and 9500 K from top to bottom, respectively. (b) Corresponding unnormalized probability distribution functions.

In a second step, we take into consideration the magnetism and perform *ai*GEMC

simulations using the ferromagnetic state for iron. We plot the density evolution as a function of MC step and corresponding unnormalized probability distribution functions in Fig. 5.2. We recognize a very similar trend in the FM-*ai*GEMC simulations compared to the NM-*ai*GEMC simulations. At 3500 K, we start with one empty box and a full box with 80 atoms. We do not observe any particle transfers between the two boxes, but the volume exchange is still present. The simulation yields the liquid density of 6.47 ± 0.04 g/cm^3. With increasing temperature, the equilibrium liquid density falls. At 5000 K we start to observe a few atoms in the vapor box, and the equilibrium vapor density increases with increasing temperature. From the density histogram we can see two well-separated peaks in the density histogram below 7500 K and a significant fluctuation in the density evolution above 7500 K as the temperature is very close to the critical temperature. At 8000 K, we identify three peaks in the density histogram for the FM-*ai*GEMC simulation, where the middle peak is due to the comparable magnitude of the surface tension effect and the entropy contribution as already mentioned by Smit et al. (1989). At 9500 K, the two boxes frequently exchange their identities, and we only observe a single peak, suggesting the simulated temperature is above the critical temperature.

5.3.2 The critical point

The liquid-vapor equilibrium line for iron obtained from the *ai*GEMC simulations is plotted in Fig. 5.3. As the correlation length tends to be infinity near the critical point, a direct determination of the critical point from finite simulation cells is difficult. However, we might approximate it by applying the scaling law (Eq. 4.17) and the rectilinear law (Eq. 4.16) to the equilibrium liquid and vapor densities above 7500 K. This method has been successfully applied to sodium and the resulted critical point compare well with experimental results (see Chapter 4). For the ferromagnetic case, we obtain the critical point at 1.64 ± 0.23 g/cm^3 and 8690 ± 141 K. For the nonmagnetic case, the critical point lies at 1.41 ± 0.17 g/cm^3 and 8701 ± 100 K. The nearly identical critical point for iron in the nonmagnetic and ferromagnetic state indicates the effect of magnetic state of iron is limited. We extrapolate the saturated vapor pressure to the critical density and obtain the critical pressure of 2.0 kbar and 2.4 kbar for iron in the nonmagnetic and ferromagnetic state, respectively. The critical point obtained in the present study agrees very well with Medvedev (2014), which lies at 1.638 g/cm^3 and 8763 K. In their study, a semi-empirical equation of state for iron with several adjustable parameters was developed and these parameters were determined by fitting to available experimental data. Considering the scarceness of experimental data for iron in the low-density regime, the excellent agreement is unexpected.

5.3.3 The bulk modulus

If neglecting the difference between the NPT ensemble and the Gibbs ensemble with a continuous change in the number of atoms for each box, we can estimate the bulk

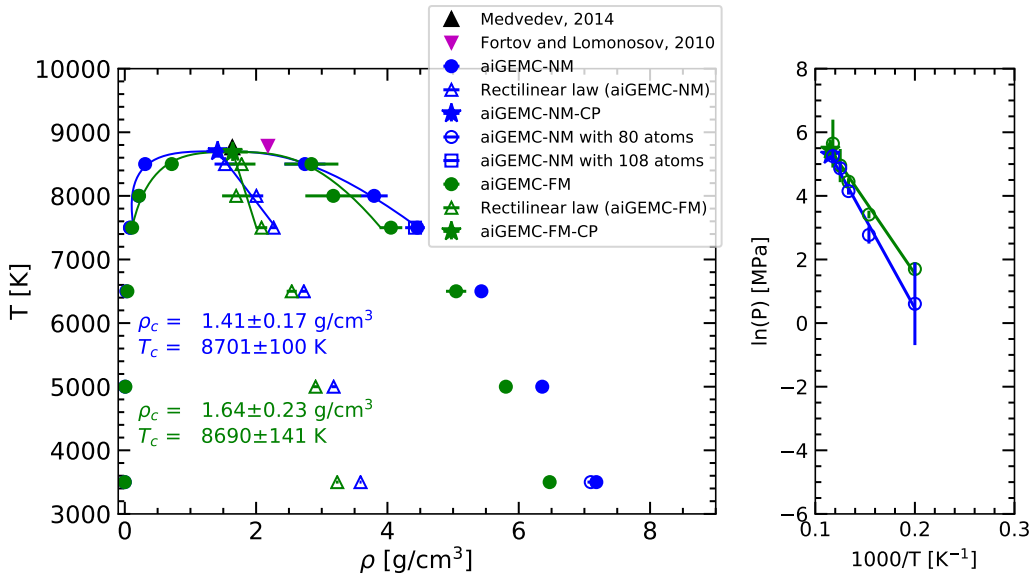

Figure 5.3: (a) The liquid-vapor equilibrium line for iron obtained from the *ai*GEMC simulations. The blue and green color denote simulations for iron in the nonmagnetic and ferromagnetic state, respectively. The solid circles represent the resulted liquid or vapor densities from the *ai*GEMC simulations, while empty triangles are densities determined by the law of rectilinear diameter. The blue and green line is a fit of the equilibrium liquid and vapor densities to the scaling law and the law of rectilinear diameter. The predicted critical point is represented by the solid stars. (b) The Clausius-Clapeyron plot of the logarithm of the saturated vapor pressure obtained from the *ai*GEMC simulations as a function of temperature.

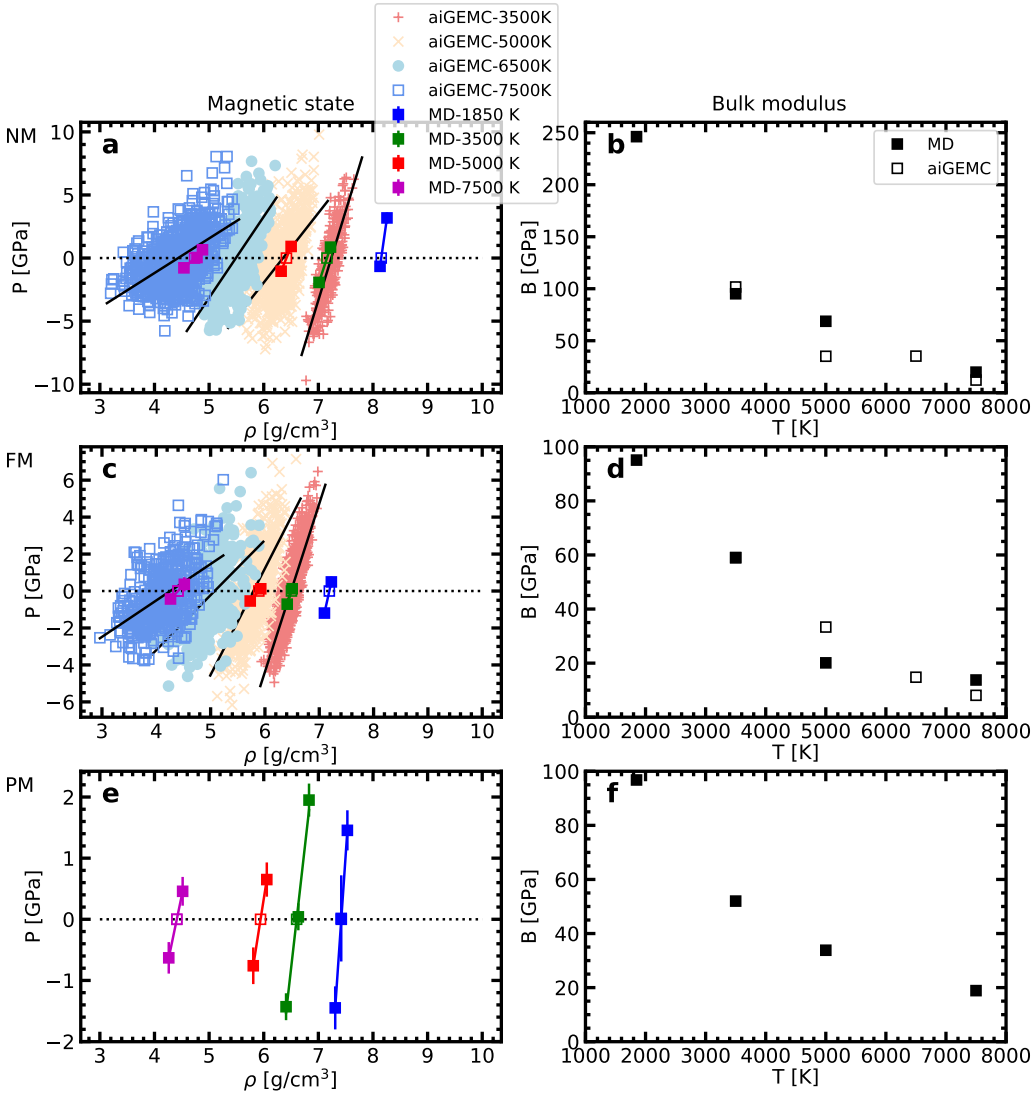

Figure 5.4: (a) The pressure-density fluctuation in the *ai*GEMC simulations for iron in the nonmagnetic (NM) and ferromagnetic state (FM) at 3500, 5000, 6500 and 7500 K. (b) The bulk modulus of the liquid iron phase defined as $\rho\frac{dP}{d\rho}$, where $\frac{dP}{d\rho}$ is derived by a linear fitting of the pressure-density data. In comparison, we also performed *ai*MD simulations for the liquid iron in the nonmagnetic, ferromagnetic and paramagnetic state (PM) to find the zero pressure density and estimate its bulk modulus.

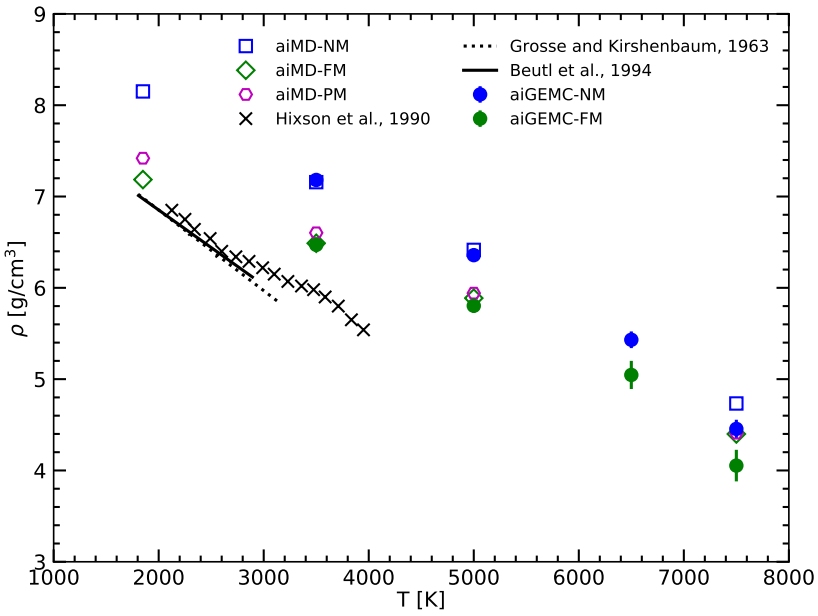

Figure 5.5: The zero pressure density up to 7500 K obtained from *ab initio* MD simulations. For comparison, we also plot the equilibrium liquid iron density derived from *ai*GEMC simulations and experimentally determined liquid iron density at around 0 GPa (Beutl et al., 1994; Grosse and Kirshenbaum, 1963; Hixson et al., 1990).

modulus for the liquid phase based on the pressure-density fluctuation (Fig. 5.4). The bulk modulus of the liquid iron phase in the NM state decreases from 250 GPa at 3500 K to 10 GPa at 7500 K, while in the FM state, it falls from 95 GPa at 7500K to 8 GPa at 7500 K. The large discrepancy at 3500 K is mainly due to the difference in the liquid iron density, which is 7.18 g/cm^3 in the NM state compared to 6.47 g/cm^3 in the FM state. The large bulk modulus for the liquid iron suggests a variation of 1 GPa in the pressure only changes the density by at most 1% at 3500 K and 10% at 7500 K. Therefore, we can safely use the density at 0 GPa to approximate the density at the liquid-vapor equilibrium density since the difference is insignificant. We could not give a reliable estimation of the bulk modulus at 8500 K due to a substantial density fluctuation. However, our previous MD simulations at 8100 K and 8750 K (see Fig. 3.1) suggest the bulk modulus should be very small since a pressure deviation of 2 kbar changes the density by 1 g/cm^3.

5.3.4 The liquid density at zero pressure from *ab initio* MD simulations

In order to estimate the density of liquid iron at zero pressure, we perform *ab initio* MD simulations in the NVT ensemble to extract the average pressure at two or three densities, from which the zero pressure density is obtained by a linear interpolation.

For the liquid iron in the FM state, we notice that the electronic optimizations in the *ab initio* MD simulation are often trapped in a local minimum. We show an example of such simulations starting with two different initial configurations at 3500 K and 6.63 g/cm^3 in Fig. 5.6. In both simulations, the liquid iron was initialized to be ferromagnetic, and the wavefunction and charge density extrapolation scheme as implemented in VASP was employed. From Fig. 5.6(a) and (d), we can see that there is a large energy drift, and the total magnetization of the system decreases steadily to zero and then oscillates around it. To reveal the origin of the energy drift, we select several snapshots and re-calculate the effective potential energy as defined in Eq. 2.13 by re-initializing the system to be ferromagnetic. The resulted potential energy is found to be lower than the one using the extrapolation scheme, and both the effect potential energy and the total magnetization fluctuates around a constant value. The energy difference might be caused by the different initial trial wavefunction employed as a starting point for the electronic optimization. As there are many local minima in the potential energy surface for a spin-polarized calculation, the electronic minimization algorithm may be trapped in such a minimum that is related to the initial conditions. Since the electronic minimization fixes the magnetic degrees of freedom at 0 K, the only physically meaningful magnetic configuration is the one with the lowermost effective potential energy. In this case, it is the ferromagnetic state. Therefore, in the present study we re-initialize the system to be ferromagnetic at every MD step in order to maintain the system to be ferromagnetic. We also stress that the simulations after 1 ps shown in Fig. 5.6(c) and (f) do not represent a paramagnetic state due to the lack of spin dynamics, even if the total magnetization is around zero.

We employ the DLM + MD method to evaluate the effect of paramagnetism on the liquid density at zero pressure. In order to determine the number of magnetic configurations needed to converge the force exerted on the atoms, we choose two snapshots from FM-*ai*MD simulations at 1850 K and 7.22 g/cm^3 and generate 1000 magnetic configurations by randomly assigning the initial magnetic moments in the up and down direction but with a zero total magnetic moment. In the DLM+MD scheme, we allow the electronic minimization and the spin dynamics is introduced by the average over many magnetic configurations. Fig. 5.8 and Fig. 5.9 show the force exerted on one randomly selected atom, pressure, the local magnetic moment of one randomly selected iron atom, the total magnetization, and their moving averages over magnetic configurations. We find that the force and pressure converged to 5% or better after employing more than 40 magnetic configurations. Therefore, we choose 40 magnetic configurations for the PM-*ai*MD simulations. It is also interesting to see that the selected atom in the first snapshot has a local magnetic moment of about 2.8 μ_B which is independent of the initial magnetic configuration, while in the second snapshot, it is more spread in a range of 0-2 μ_B. The difference may be caused by the variation in the local atomic environment.

The zero pressure densities of the liquid iron from *ai*MD simulations are plotted in Fig. 5.5. For iron in the nonmagnetic and ferromagnetic state, the determined

densities are in a good agreement with the values determined by the *ai*GEMC simulations with a difference that is less than 10%. In addition, the zero pressure density for iron in the paramagnetic state are very close to the values for iron in the ferromagnetic state, but is larger than the densities for iron in the nonmagnetic state. In order to understand this trend, we show the distribution of the local magnetic moment for iron atoms from FM-*ai*GEMC, FM-*ai*MD, and PM-*ai*MD simulations in Fig. 5.10. As expected, the magnetic moment distribution from FM-*ai*GEMC matches well with FM-*ai*MD simulations in all temperature conditions considered here. With increasing temperature, a small number of atoms flip their magnetic moment direction to be negative, and more particles become nonmagnetic. For the PM-*ai*MD simulation at 1850 K, there are two distinct peaks centered at 2.3 μ_B and -2.3 μ_B. Starting from 5000 K, the third peak at around 0 μ_B appears and its height increases with temperature, suggesting more atoms become nonmagnetic as well. The average size of the magnetic moment as a function of temperature is displayed in Fig. 5.11. It falls with increasing temperature due to the competing effect of the density, electronic Fermi smearing, and thermal motion. The decreasing density would cause the strong localization of the 3d electrons and boost the local magnetic moment, while the latter two factors reduce it. The average magnetic moment in FM is larger than PM, resulting in a larger effective atomic volume and thus a slightly lower zero pressure density. The decreasing average magnetic moment with temperature also reduces the difference of the zero pressure density between the nonmagnetic state and the magnetic state. Therefore, it is reasonable to expect that the magnetic state only slightly affect the critical point.

Comparing to the liquid iron densities determined by experiments at around zero pressure (Beutl et al., 1994; Grosse and Kirshenbaum, 1963; Hixson et al., 1990), our NM-*ai*MD and NM-*ai*GEMC simulations considerably overestimate the liquid density by 1.2 g/cm^3 (18%) at 1850 K, while the *ai*GEMC and *ai*MD calculations with iron in the FM or PM state overestimate the liquid density by 0.4 g/cm^3 (5%) at 1850 K. The improved agreement given by spin-polarized simulations compared to non-spin-polarized simulations confirms that the magnetism plays an important role in determining the physical properties of liquid iron at high temperature. At 3500 K, the liquid iron density in the ferromagnetic or paramagnetic state from our simulations is 0.4 g/cm^3 denser than the experimental value, although the experimental data are scattered above 3000 K. The discrepancy might be caused by the PBE exchange-correlation functional. Previous DLM-MD simulations for bcc and fcc iron at experimental densities from 300 K to 1662 K reported a negative pressure of 7 GPa, indicating PBE functional overestimate the zero pressure density (Alling et al., 2016). More experiments, especially at above 3500 K, are also needed in order to have a better insight into the origin of the discrepancy.

5.3.5 The structure of the fluid

We analyze the fluid structure by the radial distribution function (RDF) extracted from our *ai*GEMC and *ai*MD simulations. For the liquid phase, the main peak lies at 2.4 Å and almost keeps constant from 3500 K to 8500 K. For the vapor phase, we only show two cases at 7500, 8000 and 8500 K, where the vapor simulation box contains more than ten atoms that allow the computation of EDF. As expected, we fail to identify any local structure in the vapor phase. Our results suggest that the liquid iron in the NM state has a very similar structure to that in the FM and PM states. At 3500 K, the agreement of the RDF as obtained by the *ai*GEMC and the *ai*MD simulations is excellent. As the two methods start from different initial configurations and sample the configurational space with different paths, the remarkable consistency strongly suggests that our simulations achieved ergodicity, although this is not a formal proof. The RDF's spherical integration from 0 to its first minimum gives the coordination number, which drops from 13 at 3500 K to 7 at 8500 K for the liquid phase.

5.4 Conclusions

We have combined the *ai*GEMC method and the *ai*MD method to determine the liquid-vapor equilibrium and the critical point of iron in the nonmagnetic, ferromagnetic and paramagnetic states. The paramagnetic phase is treated by the magnetic sampling method. By comparing the liquid density at zero pressure from 1850 K to 7500 K, our study shows the FM liquid iron phase is a good proxy to the PM liquid iron phase in terms of liquid-vapor equilibrium densities. We also found the difference of the zero pressure density between the nonmagnetic state and the magnetic state drops with temperature due to the decreasing average magnetic moment. We predict the critical point lies at 1.69 g/cm^3 and 8814 K for the magnetic phase, and at 1.38 g/cm^3 and 8697 K for the nonmagnetic phase. The improved agreement with available experimental results given by spin-polarized simulations compared to non-spin-polarized simulations suggests we need to consider the magnetism in the simulations.

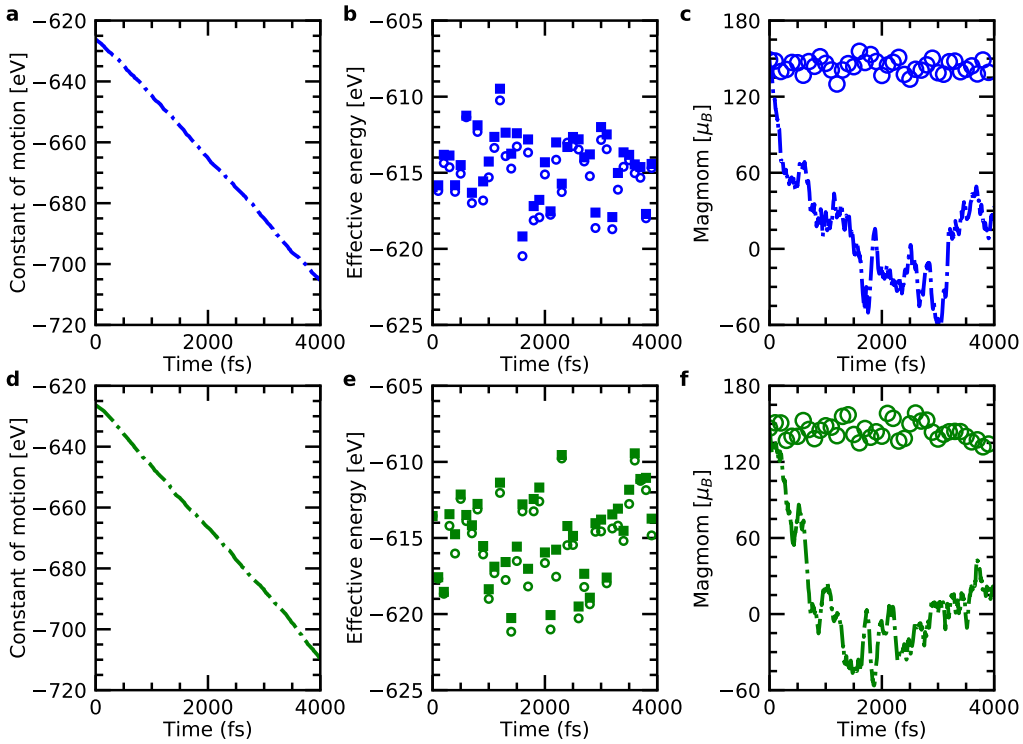

Figure 5.6: The constant of motion ((a) and (d)) as defined in Eq. 2.13, the effective potential energy (solid squares in (b) and (e)) as defined in Eq. 2.11 and the total magnetization (solid lines in (c) and (f)) of the system as function of time from the *ai*MD simulations starting with two different initial configurations at 3500 K at 6.63 g/cm^3. In both simulations, the system was initialized to be ferromagnetic at the first MD step and the wavefunction and charge density extrapolation scheme as implemented in VASP was employed for the following MD steps. We selected several snapshots and performed the electronic minimization by re-initializing the system to be ferromagnetic. The resulted effective potential energy and the total magnetization (empty circles in (b) and (c)) is lower and higher than the one calculated with the wavefunction extrapolation scheme, respectively. It suggests that for the spin-polarized simulations, the results of the electronic minimization depends on the initial trial wavefunction or charge density.

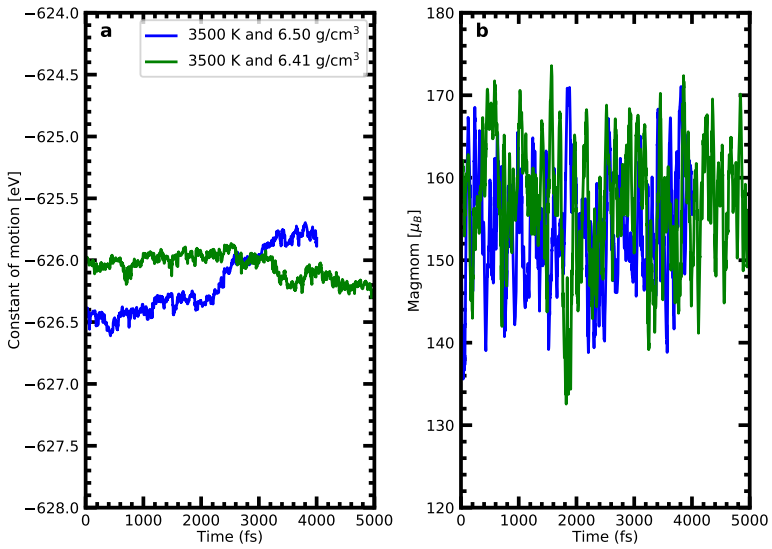

Figure 5.7: The constant of motion (a) and the total magnetization (b) of the system as function of time for FM-*ai*MD simulations at 3500 K and 6.50 g/cm^3 represented by the blue line, and 6.41 g/cm^3 represented by the green line, respectively. In both simulations, the system was initialized to be ferromagnetic at every time step.

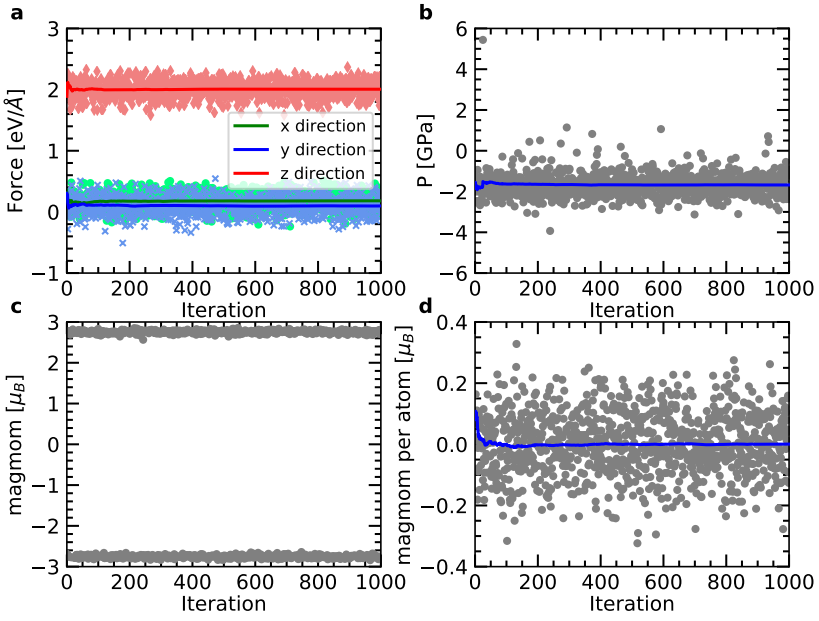

Figure 5.8: The calculated force for one randomly selected atom in the snapshot, pressure, the local magnetic moment for the selected atom, and the total magnetization of the different magnetic configurations. The accumulated average of the generated configurations is shown with a solid line.

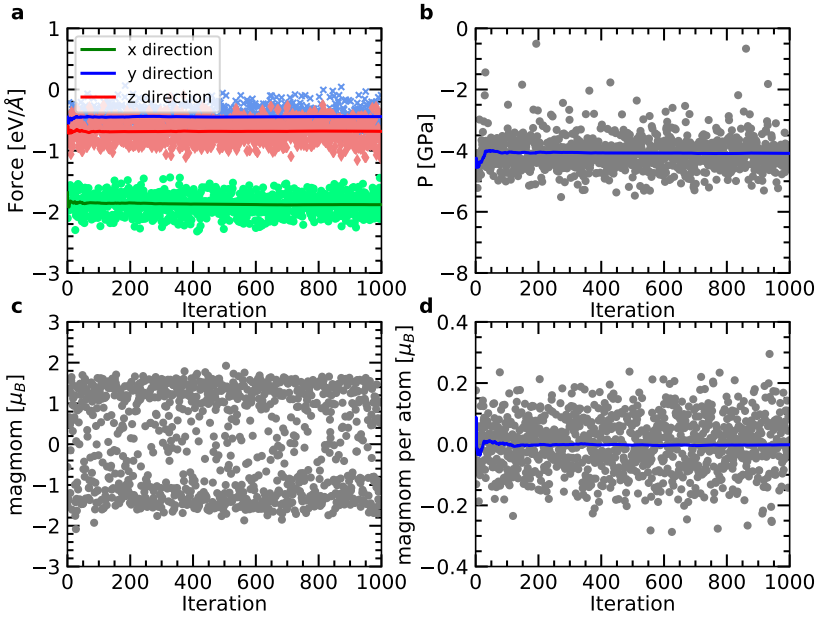

Figure 5.9: The information is the same as Fig. 5.8 but for a different snapshot.

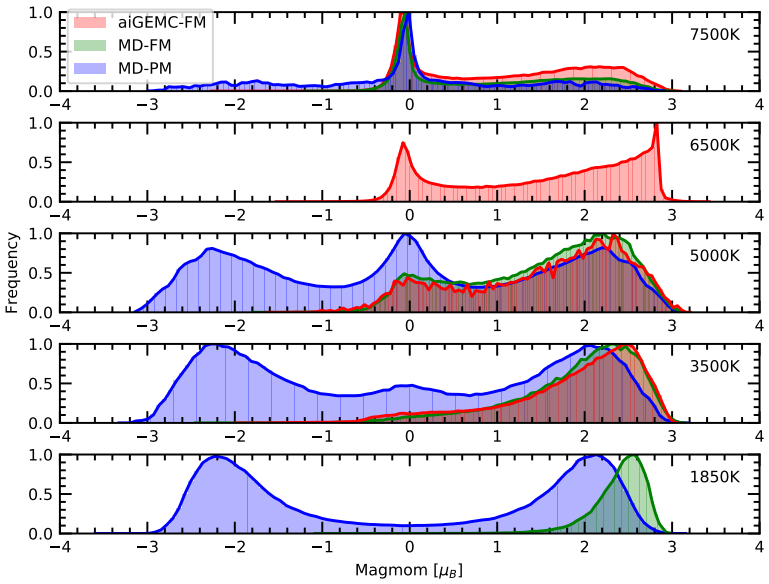

Figure 5.10: The histogram of resulting values of local magnetic moments from FM-*ai*GEMC, FM-*ai*MD, and PM-*ai*MD simulations at different temperatures.

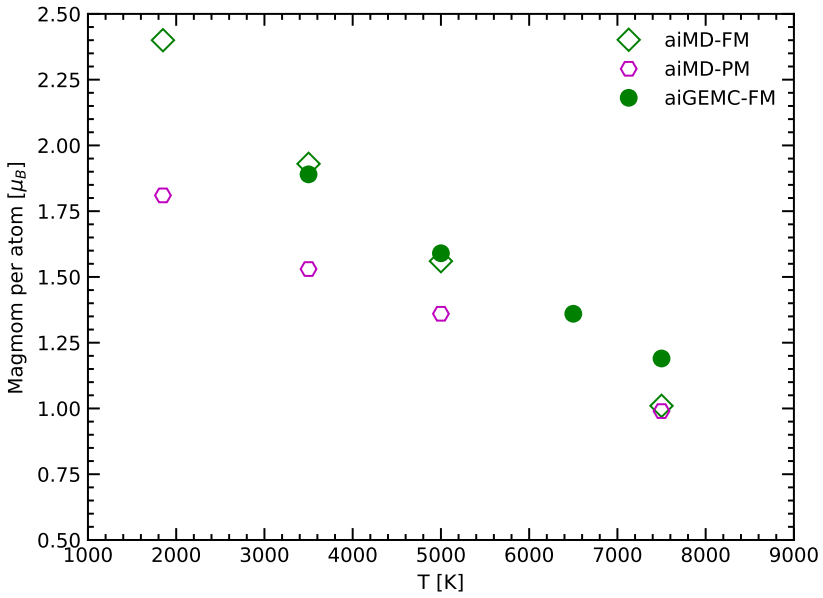

Figure 5.11: The average size of the local magnetic moment as a function of temperature derived from FM-*ai*GEMC, FM-*ai*MD, and PM-*ai*MD simulations.

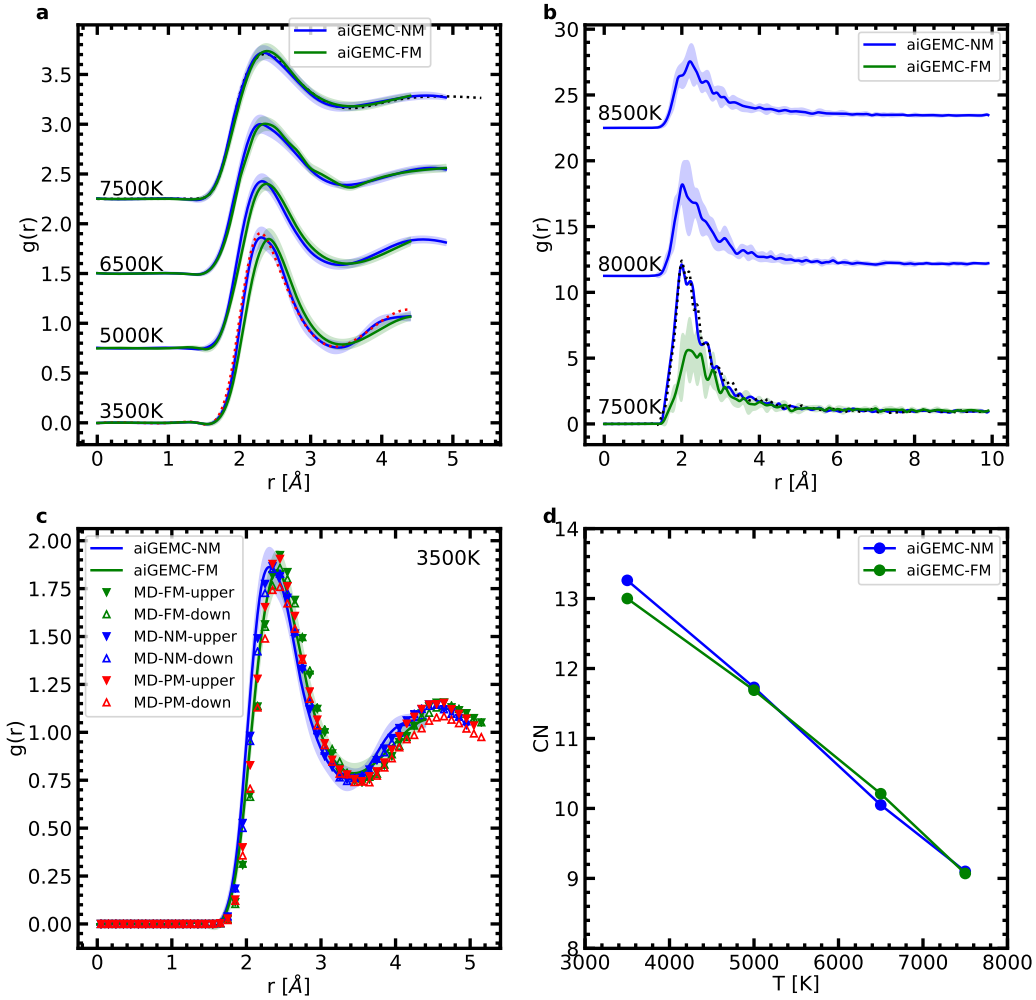

Figure 5.12: Radial distribution function ($g(r)$) for the liquid phase at 3500, 5000, 7500 and 8500 K (a), and for the vapor phase at 7500 K and 8500 K (b), as computed with the *ai*GEMC simulations. The shaded areas correspond to our estimate of the one-sigma uncertainty. The curves were shifted for readability. (c) Comparing the $g(r)$ resulted from *ai*GEMC simulations to that from *ai*MD simulations for iron in the different magnetic states at 3500 K. For *ai*MD simulations, we show two radial distribution functions that are at a density higher or lower than the zero pressure density. (d) The coordination number for the liquid iron as a function of temperature.

Chapter 6

Conclusions and future work

Contents

6.1 Conclusions

The prevailing theory to explain the origin of the Moon is the giant impact hypothesis, where a Mars-sized impactor collides with the proto-Earth, and the Moon is subsequently accreted from the proto-lunar disk made of the ejected materials. As laboratory-scale experiments are not able to simulate such planetary-scale impacts, our understanding of the giant impact mostly comes from hydrodynamic simulations. However, the outcome of these simulations depends heavily on the available equations of state to describe the thermodynamic response of the constitutive materials of the proto-Earth and of the impactor to extreme shock waves.

Iron as a building block material of the terrestrial planets naturally received significant attention. But the major effort has been put to determine its phase diagram up to the Earth's core conditions (126-360 GPa and 3000-7000 K) and beyond. The studies of iron at low densities and high temperatures are still scarce, causing great uncertainty in estimating its liquid-vapor equilibrium densities and the critical point. Consequently, it prevents us from developing an accurate equation of state for iron. As an essential ingredient in the hydrodynamic simulations, the equation of state would affect the impact energy distribution and thus cause different geochemical and geodynamic consequences, such as the amount of iron vaporized, the extent of iron-silicates equilibration, and the depth of the magma ocean. This study focuses on the thermodynamic and thermophysical properties of iron in the low-density regime to better understand iron's behavior during giant impacts.

In the first attempt, we employed *ab initio* molecular dynamics to study the mechanically stable limit of the liquid iron under the hydrostatic tension (i.e., the spinodal line), which helps locate the position of the critical point. We found the critical point lies in the temperature range of 9000-9350 K and the density range of 1.85-2.40 g/cm^3 corresponding to a pressures range of 4-7 kbars. We also computed two Hugoniot lines starting from two realistic initial states (1GPa and 1500

K, 40 GPa and 4000 K) to model the behavior of the iron core in planetesimals and planets during the impacts. By comparing the entropy values, determined by the two-phase thermodynamic method, along these Hugoniot lines to that at the boiling point of 1 bar and 3150 K, we found that the shock pressure required to reach the onset vaporization upon release and cooling is 312 GPa and 365 GPa, respectively. The application of the impedance matching method yields the peak condition achieved for a planetesimal colliding with the Earth. We found at least 70 % of the impacts in the late veneer results in a peak pressure larger than the threshold, suggesting the partial core vaporization is readily achieved. This would help mix the highly siderophile elements into magma ponds or oceans and explain the excess amount of siderophile elements in the Earth's mantle (Rubie et al., 2015). For giant impacts, the geometry effect plays an essential role in controlling the shock peak conditions, and the impedance matching method is no longer valid. However, considering the significantly lower threshold for vaporization than the previous estimation (887 GPa) which was developed based on an inaccurate equation of state, our study suggests that Theia's core underwent partial vaporization and previous hydrodynamic simulation underestimate the vapor production during giant impacts. After cooling down, the vaporized iron would condensate into a distribution of small droplets on the centimeter-level. It would enhance the iron-silicates equilibration and easily explain the recent W-isotope data that requires at least 30% core-mantle equilibration in the aftermath of the giant impact.

Additionally, we characterize the structural and transport properties of the fluid iron in the low-density region, including diffusion coefficients, viscosity, and thermal conductivity. They may provide a better constraint on iron's behavior in the proto-lunar disk. The diffusivity increases by two orders of magnitude from about 1.0×10^{-8} m^2s^{-1} at 7.75 g/cm^3 and 3000 K to about 1.3×10^{-6} m^2s^{-1} at 0.37 g/cm^3 and 12000 K. We found the low-density fluid is highly depolymerized and is mainly made of isolated atoms. The coordination number increases strongly with density below 7.75 g/cm^3, then saturates at a value of 14 that persists at least up to 6000 K and 13.3 g/cm^3, which is the condition at the Earth's inner-outer core boundary. The viscosity of iron in the outer parts of the proto-lunar disk is also extremely low, on the order of 10^{-3} Pa s. The computed electronic and thermal conductivities decrease with the density, suggesting a gradual reduction of the metallic character.

To better constrain the liquid-vapor equilibrium and the critical point of iron, we implemented the Gibbs ensemble Monte Carlo method, which avoids the interface issues and allows for a more reliable determination of the phase equilibrium. The Gibbs ensemble method, coupled with the density functional theory, has successfully been applied to the insulating system, where the internal energy of the electron-ion system is used in the Monte Carlo acceptance criteria. However, we need to consider excited electronic states for the metallic system at high temperatures. Therefore, it is necessary to utilize the finite-temperature density functional theory to capture these excited states. By taking a step back to statistical physics, we found the effective potential energy that includes the electronic free energy should be used in

the Monte Carlo acceptance criteria. Then we applied this method to sodium where several experimental data are available. The obtained liquid-vapor equilibrium and critical point are in good agreement with the experimental results, confirming our implementation's reliability and validity.

However, the application of this method to iron is not straightforward due to the extra complication from the paramagnetism of the fluid iron at high temperatures. We first performed *ab initio* Gibbs ensemble Monte Carlo simulations for iron in the nonmagnetic and ferromagnetic states. Based on the pressure-density fluctuation, we found the bulk modulus of the liquid iron from 3500 K to 7500 K is large enough that a variation of 1 GPa in pressure only changes the density by a few percent. Therefore, we can approximate the liquid-vapor equilibrium densities for the liquid branch with the densities at zero pressure in this temperature range. This is confirmed by our *ab initio* molecular dynamics simulation results. In order to evaluate the effect of the possible paramagnetism, we employed the disordered local moment molecular dynamics to investigate the liquid density at zero pressure, where the paramagnetic state is treated by the statistical average of many random magnetic configurations known as the magnetic sampling method. Our study shows the ferromagnetic liquid iron phase is a good proxy to the paramagnetic liquid iron phase in terms of liquid-vapor equilibrium densities. The improved agreement with available experimental results for the liquid iron density at around ambient pressure up to 4000 K given by spin-polarized simulations compared to non-spin-polarized simulations suggests we need to consider the magnetism in our simulations. Our preliminary results predict the critical point lies at 1.69 g/cm^3 and 8814 K for the magnetic iron phase, and at 1.38 g/cm^3 and 8697 K for the nonmagnetic iron phase. But we are running more simulations from 7500 K to 8500 K in order to accurately determine the critical point.

6.2 Future work

Within the time available, several problems could not be resolved. However, they are necessary to better understand the thermodynamic properties of iron in the low-density regime. It includes the following:

1. The role of exchange-correlation functional on the liquid-vapor equilibrium of sodium and iron. In this study, we employed the PBE-GGA exchange-correlation functional. It is a general trend that the GGA functionals underbind atoms, leading to a slighly longer bond length. Therefore, underestimating the liquid sodium densities around zero pressure, as we observed in Chapter 4, meets our expectations. For bcc iron at zero temperature, PBE underestimates its density as well. However, we found PBE overestimates the zero pressure densities of the liquid iron at high temperatures, even including the magnetism. Therefore, future work is needed to clarify the reason for the inconsistent performance of PBE on different iron phases. The inclusion

of dispersion interactions may change the phase equilibrium, which needs to be investigated in the future. However, we expect that the vapor may suffer a more significant impact since its bulk modulus is very small, and a tiny variation of pressure would shift the density considerably.

2. The effect of the longitudinal fluctuation of the magnetization on the liquid-vapor equilibrium of iron. The density difference of 0.5 g/cm^3 at 3500 K between experimental results and disorder local magnetic moment molecular dynamics simulations might be partially caused by the longitudinal fluctuation that is not considered in our study. It would shift the zero pressure densities to a lower value and improve the agreement with the experimental results. However, there is no consistent and cost-effective way to incorporate this effect in DFT calculations. Therefore, more works need to be done on improving the theoretical treatment for paramagnetism at high temperature.

Bibliography

Abrikosov, I. A., Ponomareva, A., Steneteg, P., Barannikova, S., and Alling, B. Recent progress in simulations of the paramagnetic state of magnetic materials. *Current Opinion in Solid State and Materials Science*, 20(2):85–106, 2016. (Cited on pages 30, 31 and 76.)

Ahrens, T. J. and O'Keefe, J. D. Shock melting and vaporization of lunar rocks and minerals. *The Moon*, 4(1-2):214–249, 1972. (Cited on page 51.)

Alavi, A., Kohanoff, J., Parrinello, M., and Frenkel, D. Ab initio molecular dynamics with excited electrons. *Physical Review Letters*, 73(19):2599, 1994. (Cited on page 23.)

Alfe, D., Gillan, M., and Price, G. The melting curve of iron at the pressures of the earth's core from ab initio calculations. *Nature*, 401(6752):462–464, 1999. (Cited on pages 14 and 34.)

Alfe, D. Temperature of the inner-core boundary of the earth: Melting of iron at high pressure from first-principles coexistence simulations. *Physical Review B*, 79 (6):060101, 2009. (Cited on page 15.)

Alfè, D., Kresse, G., and Gillan, M. J. Structure and dynamics of liquid iron under Earth's core conditions. *Physical Review B*, 61(1):132–142, 2000. (Cited on pages 40, 41, 46, 47 and 48.)

Alling, B., Körmann, F., Grabowski, B., Glensk, A., Abrikosov, I. A., and Neugebauer, J. Strong impact of lattice vibrations on electronic and magnetic properties of paramagnetic fe revealed by disordered local moments molecular dynamics. *Physical Review B*, 93:224411, 2016. (Cited on page 86.)

Alling, B., Marten, T., and Abrikosov, I. Effect of magnetic disorder and strong electron correlations on the thermodynamics of crn. *Physical Review B*, 82(18): 184430, 2010. (Cited on pages 31, 76 and 77.)

Antonangeli, D., Morard, G., Schmerr, N. C., Komabayashi, T., Krisch, M., Fiquet, G., and Fei, Y. Toward a mineral physics reference model for the Moon's core. *Proceedings of the National Academy of Sciences*, 112(13):3916–3919, 2015. (Cited on page 52.)

Antropov, V. P., Katsnelson, M., Van Schilfgaarde, M., and Harmon, B. Ab initio spin dynamics in magnets. *Physical Review Letters*, 75(4):729, 1995. (Cited on page 30.)

Asphaug, E. Impact Origin of the Moon? *Annual Review of Earth and Planetary Sciences*, 42(1):551–578, 2014. (Cited on page 34.)

Assael, M. J., Kakosimos, K., Banish, R. M., Brillo, J., Egry, I., Brooks, R., Quested, P. N., Mills, K. C., Nagashima, A., Sato, Y., and Wakeham, W. A. Reference Data for the Density and Viscosity of Liquid Aluminum and Liquid Iron. *Journal of Physical and Chemical Reference Data*, 35(1):285–300, 2006. (Cited on pages 47, 48 and 75.)

Baldereschi, A. Mean-value point in the brillouin zone. *Physical Review B*, 7:5212–5215, 1973. (Cited on pages 37, 65 and 77.)

Balian, R., Haar, D., and Gregg, J. *From Microphysics to Macrophysics: Methods and Applications of Statistical Physics*. Springer Berlin Heidelberg, 2007. (Cited on page 60.)

Barr, A. C. On the origin of earth's moon. *Journal of Geophysical Research: Planets*, 121(9):1573–1601, 2016. (Cited on page 12.)

Belonoshko, A. B., Lukinov, T., Fu, J., Zhao, J., Davis, S., and Simak, S. I. Stabilization of body-centred cubic iron under inner-core conditions. *Nature Geoscience*, 10(4):312–316, 2017. (Cited on page 14.)

Benz, W., Slattery, W., and Cameron, A. The origin of the moon and the single-impact hypothesis I. *Icarus*, 66(3):515–535, 1986. (Cited on page 10.)

Benz, W., Slattery, W., and Cameron, A. The origin of the moon and the single-impact hypothesis II. *Icarus*, 71(1):30–45, 1987. (Cited on page 11.)

Benz, W., Cameron, A., and Melosh, H. The origin of the moon and the single-impact hypothesis III. *Icarus*, 81(1):113–131, 1989. (Cited on page 11.)

Beutl, M., Pottlacher, G., and Jäger, H. Thermophysical properties of liquid iron. *International journal of thermophysics*, 15(6):1323–1331, 1994. (Cited on pages 84 and 86.)

Bihlmayer, G. Density-functional theory of magnetism. In Kronmüller, H., Parkin, S., Fähnle, M., Maekawa, S., and Zutic, I., editors, *Handbook of Magnetism and Advanced Magnetic Materials*. John Wiley & Sons, 2007. (Cited on page 29.)

Binder, K., Block, B. J., Virnau, P., and Tröster, A. Beyond the van der waals loop: What can be learned from simulating lennard-jones fluids inside the region of phase coexistence. *American Journal of Physics*, 80(12):1099–1109, 2012. (Cited on page 59.)

Blöchl, P. E. Projector augmented-wave method. *Physical Review B*, 50:17953–17979, 1994. (Cited on pages 35, 65 and 77.)

Born, M. and Huang, K. *Dynamical theory of crystal lattices*. Oxford University Press, 1954. (Cited on page 21.)

Bouchet, J., Mazevet, S., Morard, G., Guyot, F., and Musella, R. Ab initio equation of state of iron up to 1500 GPa. *Physical Review B*, 87(9):094102, 2013. (Cited on page 52.)

Cameron, A. The origin of the moon and the single impact hypothesis V. *Icarus*, 126(1):126–137, 1997. (Cited on page 11.)

Cameron, A. and Benz, W. The origin of the moon and the single impact hypothesis IV. *Icarus*, 92(2):204–216, 1991. (Cited on page 11.)

Cameron, A. and Ward, W. The origin of the moon. In *Lunar and Planetary Science Conference*, volume 7, 1976. (Cited on page 3.)

Campbell, A. J. Phase Diagrams and Thermodynamics of Core Materials. In Terasaki, H. and Fischer, R. A., editors, *Geophysical Monograph Series*, pages 191–199. John Wiley & Sons, 2016. (Cited on page 34.)

Canup, R. M. Forming a Moon with an Earth-like Composition via a Giant Impact. *Science*, 338(6110):1052–1055, 2012. (Cited on pages 34 and 56.)

Canup, R. M. and Righter, K., editors. *Origin of the earth and moon*. The University of Arizona space science series. University of Arizona Press, 2000. (Cited on page 34.)

Canup, R. M. Simulations of a late lunar-forming impact. *Icarus*, 168(2):433 – 456, 2004a. (Cited on pages 13, 38, 51 and 75.)

Canup, R. M. Dynamics of lunar formation. *Annual Review of Astronomy and Astrophysics*, 42(1):441–475, 2004b. (Cited on pages 3 and 34.)

Canup, R. M. and Asphaug, E. Origin of the moon in a giant impact near the end of the earth's formation. *Nature*, 412(6848):708–712, 2001. (Cited on pages 9 and 11.)

Canup, R. M. and Esposito, L. W. Accretion of the moon from an impact-generated disk. *Icarus*, 119(2):427 – 446, 1996. (Cited on page 9.)

Canup, R. M., Ward, W. R., and Cameron, A. A scaling relationship for satellite-forming impacts. *Icarus*, 150(2):288–296, 2001. (Cited on page 11.)

Canup, R. M., Visscher, C., Salmon, J., and Fegley Jr, B. Lunar volatile depletion due to incomplete accretion within an impact-generated disk. *Nature Geoscience*, 8(12):918–921, 2015. (Cited on page 4.)

Caracas, R. Crystal Structures of Core Materials. In Terasaki, H. and Fischer, R. A., editors, *Geophysical Monograph Series*, pages 55–68. John Wiley & Sons, 2016. (Cited on page 34.)

Carter, P. J., Lock, S. J., and Stewart, S. T. The Energy Budgets of Giant Impacts. *Journal of Geophysical Research: Planets*, 125(1), 2020. (Cited on page 54.)

Chen, G. Q. and Ahrens, T. J. High Pressure and High Temperature Equation-of-State of Gamma and Liquid Iron. *MRS Proceedings*, 499, 1997. (Cited on page 50.)

Ćuk, M. and Stewart, S. T. Making the moon from a fast-spinning earth: a giant impact followed by resonant despinning. *Science*, 338(6110):1047–1052, 2012. (Cited on pages 6, 7, 8, 9, 11, 34 and 56.)

Ćuk, M., Hamilton, D. P., Lock, S. J., and Stewart, S. T. Tidal evolution of the moon from a high-obliquity, high-angular-momentum earth. *Nature*, 539(7629): 402–406, 2016. (Cited on pages 6, 7 and 8.)

Dahl, T. W. and Stevenson, D. J. Turbulent mixing of metal and silicate during planet accretion—and interpretation of the Hf-W chronometer. *Earth and Planetary Science Letters*, 295(1-2):177–186, 2010. (Cited on page 12.)

de Wijs, G. A., Kresse, G., Vočadlo, L., Dobson, D., Alfè, D., Gillan, M. J., and Price, G. D. The viscosity of liquid iron at the physical conditions of the Earth's core. *Nature*, 392(6678):805–807, 1998. (Cited on pages 47, 48 and 56.)

Desjarlais, M. P. First-principles calculation of entropy for liquid metals. *Physical Review E*, 88(6), 2013. (Cited on page 37.)

Dillon, I. G., Nelson, P. A., and Swanson, B. S. Measurement of Densities and Estimation of Critical Properties of the Alkali Metals. *The Journal of Chemical Physics*, 44:4229, 1966. (Cited on pages 70, 71 and 73.)

Dorogokupets, P., Dymshits, A., Litasov, K., and Sokolova, T. Thermodynamics and equations of state of iron to 350 gpa and 6000 k. *Scientific reports*, 7(1):1–11, 2017. (Cited on page 16.)

Dufty, J., Wrighton, J., Luo, K., and Trickey, S. On the Kubo-Greenwood model for electron conductivity. *Contributions to Plasma Physics*, 58(2-3):150–154, 2018. (Cited on page 48.)

Engel, E. and Dreizler, R. M. *Density functional theory: An Advanced Course*. Springer-Verlag Berlin Heidelberg, 2013. (Cited on page 26.)

Eschrig, H. *The fundamentals of density functional theory*. Vieweg+Teubner Verlag, 1996. (Cited on page 20.)

Forbes, J. W. *Shock Wave Compression of Condensed Matter*. Springer Berlin Heidelberg, 2013. (Cited on pages 8 and 51.)

Fortov, V. and Lomonosov, I. Shock waves and equations of state of matter. *Shock waves*, 20(1):53–71, 2010. (Cited on pages 15, 16, 34 and 39.)

Franchi, I. A., Wright, I. P., Sexton, A. S., and Pillinger, C. T. The oxygen-isotopic composition of earth and mars. *Meteoritics & Planetary Science*, 34(4):657–661, 1999. (Cited on page 3.)

Fratanduono, D. E., Millot, M., Kraus, R. G., Spaulding, D. K., Collins, G. W., Celliers, P. M., and Eggert, J. H. Thermodynamic properties of $MgSiO_3$ at super-Earth mantle conditions. *Physical Review B*, 97(21), 2018. (Cited on page 53.)

Frenkel, D. and Smit, B. *Understanding Molecular Simulation: From Algorithms to Applications*. Computational science. Academic Press, 2001. (Cited on pages 60, 65 and 71.)

Gambino, D., Arale Brännvall, M., Ehn, A., Hedström, Y., and Alling, B. Longitudinal spin fluctuations in bcc and liquid fe at high temperature and pressure calculated with a supercell approach. *Physical Review B*, 102:014402, 2020. (Cited on page 76.)

Goel, H., Ling, S., Ellis, B. N., Taconi, A., Slater, B., and Rai, N. Predicting vapor liquid equilibria using density functional theory: A case study of argon. *The Journal of Chemical Physics*, 148(22):224501, 2018. (Cited on pages 60 and 71.)

Goldreich, P. History of the lunar orbit. *Reviews of Geophysics*, 4(4):411–439, 1966. (Cited on page 5.)

Green, J. L., Durben, D. J., Wolf, G. H., and Angell, C. A. Water and Solutions at Negative Pressure: Raman Spectroscopic Study to -80 Megapascals. *Science*, 249 (4969):649–652, 1990. (Cited on page 36.)

Greenwood, D. A. The Boltzmann Equation in the Theory of Electrical Conduction in Metals. *Proceedings of the Physical Society*, 71(4):585–596, 1958. (Cited on pages 37 and 48.)

Grosse, A. and Kirshenbaum, A. The densities of liquid iron and nickel and an estimate of their critical temperature. *Journal of Inorganic and Nuclear Chemistry*, 25(4):331–334, 1963. (Cited on pages 15, 16, 34, 75, 84 and 86.)

Gyorffy, B., Pindor, A., Staunton, J., Stocks, G., and Winter, H. A first-principles theory of ferromagnetic phase transitions in metals. *Journal of Physics F: Metal Physics*, 15(6):1337, 1985. (Cited on page 31.)

Hansen, J.-P. and McDonald, I. R. *Theory of Simple Liquids (Fourth Edition)*. Academic Press, 2013. (Cited on page 22.)

Hartmann, W. K. and Davis, D. R. Satellite-sized planetesimals and lunar origin. *Icarus*, 24(4):504 – 515, 1975. (Cited on page 3.)

Hirose, K., Labrosse, S., and Hernlund, J. Composition and State of the Core. *Annual Review of Earth and Planetary Sciences*, 41(1):657–691, 2013. (Cited on pages 34 and 52.)

Hixson, R., Winkler, M., and Hodgdon, M. Sound speed and thermophysical properties of liquid iron and nickel. *Physical Review B*, 42(10):6485, 1990. (Cited on pages 15, 16, 34, 75, 84 and 86.)

Hohenberg, P. and Kohn, W. Inhomogeneous electron gas. *Physical Review*, 136 (3B):B864, 1964. (Cited on pages 25, 35 and 77.)

Huang, K. *Statistical Mechanics*. John Wiley & Sons, 2nd edition, 1987. (Cited on page 60.)

Jacobson, S. A., Rubie, D. C., Hernlund, J., Morbidelli, A., and Nakajima, M. Formation, stratification, and mixing of the cores of earth and venus. *Earth and Planetary Science Letters*, 474:375–386, 2017. (Cited on page 13.)

Karthika, S., Radhakrishnan, T. K., and Kalaichelvi, P. A Review of Classical and Nonclassical Nucleation Theories. *Crystal Growth & Design*, 16(11):6663–6681, 2016. (Cited on page 39.)

Kaul, S. N. Phase transitions and finite temperature magnetism: Experiment and analysis. In Kronmüller, H., Parkin, S., Fähnle, M., Maekawa, S., and Zutic, I., editors, *Handbook of Magnetism and Advanced Magnetic Materials*. John Wiley & Sons, 2007. (Cited on pages 29 and 76.)

Kendall, J. D. and Melosh, H. Differentiated planetesimal impacts into a terrestrial magma ocean: Fate of the iron core. *Earth and Planetary Science Letters*, 448: 24–33, 2016. (Cited on pages 12 and 56.)

Khmelevskyi, S. Longitudinal integration measure in classical spin space and its application to first-principle based simulations of ferromagnetic metals. *Journal of Magnetism and Magnetic Materials*, 461:14 – 18, 2018. (Cited on page 32.)

Kohn, W. and Sham, L. J. Self-consistent equations including exchange and correlation effects. *Physical Review*, 140(4A):A1133, 1965. (Cited on pages 26, 35 and 77.)

Korell, J.-A., French, M., Steinle-Neumann, G., and Redmer, R. Paramagnetic-to-Diamagnetic Transition in Dense Liquid Iron and Its Influence on Electronic Transport Properties. *Physical Review Letters*, 122(8):086601, 2019. (Cited on page 49.)

Kraus, R. G., Root, S., Lemke, R. W., Stewart, S. T., Jacobsen, S. B., and Mattsson, T. R. Impact vaporization of planetesimal cores in the late stages of planet formation. *Nature Geoscience*, 8(4):269–272, 2015. (Cited on pages 12, 13, 34, 51, 54 and 55.)

Kresse, G. and Furthmüller, J. Efficient iterative schemes for ab initio total-energy calculations using a plane-wave basis set. *Physical Review B*, 54:11169–11186, 1996. (Cited on pages 35, 65 and 77.)

Kresse, G. and Furthmüller, J. Efficiency of ab-initio total energy calculations for metals and semiconductors using a plane-wave basis set. *Computational Materials Science*, 6(1):15 – 50, 1996. (Cited on pages 35, 65 and 77.)

Kresse, G. and Joubert, D. From ultrasoft pseudopotentials to the projector augmented-wave method. *Physical Review B*, 59:1758–1775, 1999. (Cited on pages 35, 65 and 77.)

Kruijer, T. S., Kleine, T., Fischer-Gödde, M., and Sprung, P. Lunar tungsten isotopic evidence for the late veneer. *Nature*, 520(7548):534–537, 2015. (Cited on pages 4 and 12.)

Kubo, R. Statistical-Mechanical Theory of Irreversible Processes. I. General Theory and Simple Applications to Magnetic and Conduction Problems. *Journal of the Physical Society of Japan*, 12(6):570–586, 1957. (Cited on pages 37 and 48.)

Lichtenstein, A., Katsnelson, M., and Kotliar, G. Finite-temperature magnetism of transition metals: An ab initio dynamical mean-field theory. *Physical Review Letters*, 87(6):067205, 2001. (Cited on pages 31, 35 and 76.)

Lin, S.-T., Blanco, M., and Goddard, W. A. The two-phase model for calculating thermodynamic properties of liquids from molecular dynamics: Validation for the phase diagram of Lennard-Jones fluids. *The Journal of Chemical Physics*, 119 (22):11792–11805, 2003. (Cited on page 37.)

Lock, S. J., Stewart, S. T., Petaev, M. I., Leinhardt, Z., Mace, M. T., Jacobsen, S. B., and Cuk, M. The origin of the moon within a terrestrial synestia. *Journal of Geophysical Research: Planets*, 123(4):910–951, 2018. (Cited on pages 9, 11, 12 and 34.)

Ma, P.-W. and Dudarev, S. Constrained density functional for noncollinear magnetism. *Physical Review B*, 91(5):054420, 2015. (Cited on page 30.)

Ma, P.-W., Dudarev, S. L., and Wróbel, J. S. Dynamic simulation of structural phase transitions in magnetic iron. *Physical Review B*, 96:094418, 2017. (Cited on page 30.)

Marqués, M., González, L. E., and González, D. J. *Ab initio* study of the structure and dynamics of bulk liquid Fe. *Physical Review B*, 92(13):134203, 2015. (Cited on pages 35 and 41.)

Marx, D. and Hutter, J. *Ab initio molecular dynamics: basic theory and advanced methods*. Cambridge University Press, 2009. (Cited on page 22.)

McGrath, M. J., Siepmann, J. I., Kuo, I.-F. W., and Mundy, C. J. Vapor–liquid equilibria of water from first principles: comparison of density functionals and basis sets. *Molecular Physics*, 104(22-24):3619–3626, 2006a. (Cited on page 60.)

McGrath, M. J., Siepmann, J. I., Kuo, I.-F. W., Mundy, C. J., VandeVondele, J., Sprik, M., Hutter, J., Mohamed, F., Krack, M., and Parrinello, M. Toward a monte carlo program for simulating vapor–liquid phase equilibria from first principles. *Computer Physics Communications*, 169(1):289 – 294, 2005. (Cited on page 60.)

McGrath, M. J., Siepmann, J. I., Kuo, I.-F. W., Mundy, C. J., VandeVondele, J., Hutter, J., Mohamed, F., and Krack, M. Simulating fluid-phase equilibria of water from first principles. *The Journal of Physical Chemistry A*, 110(2):640–646, 2006b. (Cited on page 60.)

McGrath, M. J., Kuo, I.-F. W., Ghogomu, J. N., Mundy, C. J., and Siepmann, J. I. Vapor–liquid coexistence curves for methanol and methane using dispersion-corrected density functional theory. *The Journal of Physical Chemistry B*, 115 (40):11688–11692, 2011. (Cited on page 60.)

Medvedev, A. B. Wide-range multiphase equation of state for iron. *Combustion, Explosion, and Shock Waves*, 50(5):582–598, 2014. (Cited on pages 34, 39 and 81.)

Melosh, H. J. *Planetary Surface Processes*. Cambridge University Press, 2011. (Cited on pages 51 and 54.)

Melosh, H. A hydrocode equation of state for SiO_2. *Meteoritics & Planetary Science*, 42(12):2079–2098, 2007. (Cited on page 13.)

Melosh, H. New approaches to the moon's isotopic crisis. *Philosophical Transactions of the Royal Society A: Mathematical, Physical and Engineering Sciences*, 372 (2024):20130168, 2014. (Cited on page 12.)

Mermin, N. D. Thermal properties of the inhomogeneous electron gas. *Physical Review*, 137(5A):A1441, 1965. (Cited on pages 25, 35 and 77.)

Metropolis, N., Rosenbluth, A. W., Rosenbluth, M. N., Teller, A. H., and Teller, E. Equation of state calculations by fast computing machines. *The Journal of Chemical Physics*, 21(6):1087–1092, 1953. (Cited on pages 61 and 62.)

Militzer, B. Equation of state calculations of hydrogen-helium mixtures in solar and extrasolar giant planets. *Physical Review B*, 87:014202, 2013. (Cited on pages 51 and 53.)

Monkhorst, H. J. and Pack, J. D. Special points for brillouin-zone integrations. *Physical Review B*, 13:5188–5192, 1976. (Cited on page 35.)

Nakajima, M. and Stevenson, D. J. Melting and mixing states of the earth's mantle after the moon-forming impact. *Earth and Planetary Science Letters*, 427:286–295, 2015. (Cited on pages 13, 54 and 56.)

Nimmo, F., O'Brien, D., and Kleine, T. Tungsten isotopic evolution during late-stage accretion: Constraints on Earth–Moon equilibration. *Earth and Planetary Science Letters*, 292(3-4):363–370, 2010. (Cited on page 56.)

Nosé, S. A unified formulation of the constant temperature molecular dynamics methods. *The Journal of Chemical Physics*, 81(1):511–519, 1984. (Cited on pages 23, 35, 65 and 77.)

Pahlevan, K. and Stevenson, D. J. Equilibration in the aftermath of the lunar-forming giant impact. *Earth and Planetary Science Letters*, 262(3):438 – 449, 2007. (Cited on page 3.)

Palmer, B. J. and Lo, C. Molecular dynamics implementation of the gibbs ensemble calculation. *The Journal of Chemical Physics*, 101(12):10899–10907, 1994. (Cited on page 60.)

Panagiotopoulos, A. Z., Quirke, N., Stapleton, M., and Tildesley, D. J. Phase equilibria by simulation in the gibbs ensemble. *Molecular Physics*, 63(4):527–545, 1988. (Cited on page 60.)

Panagiotopoulos, A. Z. Direct determination of phase coexistence properties of fluids by monte carlo simulation in a new ensemble. *Molecular Physics*, 61(4):813–826, 1987. (Cited on pages 59, 60 and 64.)

Paniello, R. C., Day, J. M., and Moynier, F. Zinc isotopic evidence for the origin of the moon. *Nature*, 490(7420):376–379, 2012. (Cited on page 4.)

Parr, R. G. and Yang, W. Density functional theory of atoms and molecules. *Oxford University Press*, 1989. (Cited on pages 25, 26 and 28.)

Perdew, J. P., Burke, K., and Ernzerhof, M. Generalized gradient approximation made simple. *Physical Review Letters*, 77:3865–3868, 1996. (Cited on pages 35, 65 and 77.)

Pierazzo, E. and Melosh, H. J. Hydrocode modeling of oblique impacts: The fate of the projectile. *Meteoritics & Planetary Science*, 35(1):117–130, 2000a. (Cited on page 54.)

Pierazzo, E. and Melosh, H. J. Understanding Oblique Impacts from Experiments, Observations, and Modeling. *Annual Review of Earth and Planetary Sciences*, 28 (1):141–167, 2000b. (Cited on page 54.)

Pierazzo, E., Vickery, A., and Melosh, H. A reevaluation of impact melt production. *Icarus*, 127(2):408–423, 1997. (Cited on pages 13 and 34.)

Pindor, A., Staunton, J., Stocks, G., and Winter, H. Disordered local moment state of magnetic transition metals: a self-consistent KKR CPA calculation. *Journal of Physics F: Metal Physics*, 13(5):979, 1983. (Cited on page 31.)

Poole, P. H., Sciortino, F., Essmann, U., and Stanley, H. E. Phase behaviour of metastable water. *Nature*, 360(6402):324–328, 1992. (Cited on page 36.)

Posner, E. S., Steinle-Neumann, G., Vlček, V., and Rubie, D. C. Structural changes and anomalous self-diffusion of oxygen in liquid iron at high pressure. *Geophysical Research Letters*, 44(8):3526–3534, 2017. (Cited on pages 46 and 47.)

Pozzo, M., Davies, C., Gubbins, D., and Alfè, D. Thermal and electrical conductivity of iron at Earth's core conditions. *Nature*, 485(7398):355–358, 2012. (Cited on pages 37 and 38.)

Pozzo, M., Davies, C., Gubbins, D., and Alfè, D. Transport properties for liquid silicon-oxygen-iron mixtures at Earth's core conditions. *Physical Review B*, 87(1), 2013. (Cited on page 38.)

Raymond, S. N., O'Brien, D. P., Morbidelli, A., and Kaib, N. A. Building the terrestrial planets: Constrained accretion in the inner Solar System. *Icarus*, 203 (2):644–662, 2009. (Cited on pages 51 and 54.)

Recoules, V., Renaudin, P., Clérouin, J., Noiret, P., and Zérah, G. Electrical conductivity of hot expanded aluminum: Experimental measurements and *ab initio* calculations. *Physical Review E*, 66(5):056412, 2002. (Cited on page 49.)

Reed, M. S. and Flurchick, K. Hybrid molecular dynamics: an approach to low density simulations. *Computer Physics Communications*, 81(1-2):56–64, 1994. (Cited on page 45.)

Rowlinson, J. S. and Swinton, F. *Liquids and liquid Mixtures*. Butterworth-Heinemann, 3rd edition, 1982. (Cited on page 71.)

Rowlinson, J. S. and Widom, B. *Molecular Theory of Capillarity*. Clarendon Press, Oxford, 1982. (Cited on page 71.)

Ruban, A. V., Khmelevskyi, S., Mohn, P., and Johansson, B. Temperature-induced longitudinal spin fluctuations in fe and ni. *Physical Review B*, 75(5):054402, 2007. (Cited on page 16.)

Rubie, D., Nimmo, F., and Melosh, H. Formation of the Earth's Core. In *Treatise on Geophysics*, pages 43–79. Elsevier, 2015. (Cited on pages 57 and 94.)

Rudge, J. F., Kleine, T., and Bourdon, B. Broad bounds on Earth's accretion and core formation constrained by geochemical models. *Nature Geoscience*, 3(6): 439–443, 2010. (Cited on pages 56 and 57.)

Schienbein, P. and Marx, D. Liquid–vapor phase diagram of rpbe-d3 water: Electronic properties along the coexistence curve and in the supercritical phase. *The Journal of Physical Chemistry B*, 122(13):3318–3329, 2018. (Cited on page 60.)

Sinmyo, R., Hirose, K., and Ohishi, Y. Melting curve of iron to 290 gpa determined in a resistance-heated diamond-anvil cell. *Earth and Planetary Science Letters*, 510:45–52, 2019. (Cited on pages 14 and 15.)

Sjostrom, T. and Crockett, S. Quantum molecular dynamics of warm dense iron and a five-phase equation of state. *Physical Review E*, 97(5), 2018. (Cited on pages 34, 50 and 52.)

Smit, B., Smedt, P. D., and Frenkel, D. Computer simulations in the gibbs ensemble. *Molecular Physics*, 68(4):931–950, 1989. (Cited on pages 61, 70 and 81.)

Smith, R. F., Fratanduono, D. E., Braun, D. G., Duffy, T. S., Wicks, J. K., Celliers, P. M., Ali, S. J., Fernandez-Pañella, A., Kraus, R. G., Swift, D. C., et al. Equation of state of iron under core conditions of large rocky exoplanets. *Nature Astronomy*, 2(6):452–458, 2018. (Cited on page 14.)

Speedy, R. J. Stability-limit conjecture. an interpretation of the properties of water. *The Journal of Physical Chemistry*, 86(6):982–991, 1982. (Cited on pages 35 and 71.)

Stevenson, D. J. Origin of the moon-the collision hypothesis. *Annual Review of Earth and Planetary Sciences*, 15(1):271–315, 1987. (Cited on pages 2, 9, 10 and 13.)

Stewart, A. J., Schmidt, M. W., van Westrenen, W., and Liebske, C. Mars: A New Core-Crystallization Regime. *Science*, 316(5829):1323–1325, 2007. (Cited on page 52.)

Tateno, S., Hirose, K., Ohishi, Y., and Tatsumi, Y. The Structure of Iron in Earth's Inner Core. *Science*, 330(6002):359–361, 2010. (Cited on page 34.)

Tian, Z. and Wisdom, J. Vertical angular momentum constraint on lunar formation and orbital history. *Proceedings of the National Academy of Sciences*, 117(27): 15460–15464, 2020. (Cited on page 8.)

Touboul, M., Puchtel, I. S., and Walker, R. J. Tungsten isotopic evidence for disproportional late accretion to the earth and moon. *Nature*, 520(7548):530–533, 2015. (Cited on pages 4, 12, 56 and 57.)

Touma, J. and Wisdom, J. Evolution of the earth-moon system. *The Astronomical Journal*, 108:1943–1961, 1994. (Cited on pages 5 and 7.)

Touma, J. and Wisdom, J. Resonances in the early evolution of the earth-moon system. *The Astronomical Journal*, 115(4):1653, 1998. (Cited on pages 5, 6 and 7.)

Tsuchiya, T., Wentzcovitch, R. M., da Silva, C. R. S., and de Gironcoli, S. Spin transition in magnesiowüstite in earth's lower mantle. *Physical Review Letters*, 96:198501, 2006. (Cited on page 32.)

Vasisht, V. V., Saw, S., and Sastry, S. Liquid–liquid critical point in supercooled silicon. *Nature Physics*, 7(7):549–553, 2011. (Cited on page 36.)

von Barth, U. and Hedin, L. A local exchange-correlation potential for the spin polarized case. i. *Journal of Physics C: Solid State Physics*, 5(13):1629, 1972. (Cited on page 28.)

Vočadlo, L., de Wijs, G. A., Kresse, G., Gillan, M., and Price, G. D. First principles calculations on crystalline and liquid iron at Earth's core conditions. *Faraday Discussions*, 106:205–218, 1997. (Cited on pages 40 and 41.)

Wang, K. and Jacobsen, S. B. Potassium isotopic evidence for a high-energy giant impact origin of the moon. *Nature*, 538(7626):487–490, 2016. (Cited on page 4.)

Ward, W. R. and Canup, R. M. Origin of the moon's orbital inclination from resonant disk interactions. *Nature*, 403(6771):741–743, 2000. (Cited on page 7.)

Ward, W. R., Canup, R. M., and Rufu, R. Analytical model for the tidal evolution of the evection resonance and the timing of resonance escape. *Journal of Geophysical Research: Planets*, page e2019JE006266, 2020. (Cited on pages 6, 7 and 8.)

Waseda, Y. and Suzuki, K. Atomic distribution and magnetic moment in liquid iron by neutron diffraction. *physica status solidi (b)*, 39(2):669–678, 1970. (Cited on pages 31, 35 and 76.)

Wentzcovitch, R. M., Martins, J. L., and Allen, P. B. Energy versus free-energy conservation in first-principles molecular dynamics. *Physical Review B*, 45:11372–11374, 1992. (Cited on pages 23 and 24.)

Wilding, N. B. Critical-point and coexistence-curve properties of the lennard-jones fluid: A finite-size scaling study. *Physical Review E*, 52:602–611, 1995. (Cited on page 71.)

Wisdom, J. and Tian, Z. Early evolution of the earth–moon system with a fast-spinning earth. *Icarus*, 256:138–146, 2015. (Cited on pages 6, 7 and 8.)

Zhang, J., Dauphas, N., Davis, A. M., Leya, I., and Fedkin, A. The proto-earth as a significant source of lunar material. *Nature Geoscience*, 5(4):251–255, 2012. (Cited on page 4.)

Zhao, G., Yu, Y. J., Yan, J. L., Ding, M. C., Zhao, X. G., and Wang, H. Y. Phase behavior of metastable liquid silicon at negative pressure: *Ab initio* molecular dynamics. *Physical Review B*, 93(14), 2016. (Cited on page 36.)

Zwanzig, R. W. Transition from quantum to" classical" partition function. *Physical Review*, 106(1):13, 1957. (Cited on page 23.)

Appendix A

Manuscripts

---

1. Earth and Planetary Science Letters (2020): Partial core vaporization during Giant Impacts inferred from the entropy and the critical point of iron, doi: 10.1016/j.epsl.2020.116463.
2. Physical Chemistry Chemical Physics (accepted): *Ab initio* Gibbs ensemble Monte Carlo simulations of the liquid-vapor equilibrium and the critical point of sodium.
3. Physics of the Earth and Planetary Interiors (submitted): Thermophysical properties of hot fluid iron in the protolunar disk.